An Accurate Approach to Modeling the Genuine Tooth Surfaces of the Face-Milled Spiral Bevel and Hypoid Gears

Shuangxi Xie

A Thesis

In the Department

of

Mechanical and Industrial Engineering

Presented in Partial Fulfillment of the Requirements

For the Degree of Doctor of Philosophy at

Concordia University

Montreal Quebec, Canada

Dec 2011

CONCORDIA UNIVERSITY

School of Graduate Studies

This is to certify that the thesis prepared

By: Shuangxi Xie

Entitled: An Accurate Approach to Modeling the Genuine Tooth Surfaces of the Face-Milled Spiral Bevel and Hypoid Gears

and submitted in partial fulfillment of the requirements for the degree of

Doctor of Philosophy

complies with the regulations of the University and meets the accepted standards with respect to originality and quality.

Signed by the final examining committee:

_____ Chair

Deyi Xue (Calgary) External Examiner

Will Tian (CIISE) External to Program

Mingyuan Chen Examiner

Ali Akgunduz Examiner

Zezhong Chevy Chen Thesis Supervisor

Approved by:

_____

Chair of Department or Graduate Program Director

_____ _____

Dean of Faculty

ABSTRACT

An Accurate Approach to Modeling the Genuine Tooth Surfaces of the Face-Milled Spiral Bevel and Hypoid Gears

Shuangxi Xie Ph.D.

Concordia University, 2011

Accurate gear tooth surface machining is critical operation to achieve the low noise gear drive. Normally tooth rough surface is produced by face milling process, and then finished by tooth grinding process. The high speed face milling can produce high tooth surface quality as grinding with more productivity, but currently the accurate tooth surface cannot be obtained due to the use of simplified cutter geometric model used in tooth modeling. The accuracy of roughing gear tooth produced by face milling is also important. The cutter in finishing process can get benefit from the equally distributed remaining material on roughed stock. In this paper an accurate approach to modeling the genuine tooth surface for face-milled spiral bevel and hypoid gears is proposed.

In the first part of this work, a genuine cutter geometric model for the spiral bevel and hypoid gears is proposed. This model fully matches the real cutter used in industry. The side and circular cutting edges of the genuine cutter are defined on the blade rake plane, rather than the normal plane as the simplified cutter. In the genuine cutter modeling the rake angles and relief angles are taken into consideration. To compare the difference between genuine cutter and simplified cutter, the geometric errors of the simplified cutter are analyzed. The genuine cutter geometric model lays a ground for machining the accurate face-milled spiral bevel and hypoid gear tooth.

In the second part of this work, we build up the accurate spiral bevel gear tooth by using the genuine cutter geometric model. First, with the genuine cutter the member gear tooth surfaces are developed based on the kinematics of the non-generated gear tooth machining process, and then with the genuine pinion cutter geometric model the pinion tooth surfaces are modeled based on the kinematics of pinion generation process. The tooth surfaces of member gear and pinion are accurately represented as NURBS surface by optimizing the number of sampling and control points. The NURBS tooth surface can be directly implemented into CAD software, and provide the accurate geometry for the following FEA process. Finally the tooth geometric errors are calculated, and the tooth contact of the genuine gears is compare to the tooth contact of simplified gears.

In the third part, the accurate tooth surfaces of hypoid gears are built up. Similar to spiral bevel gear tooth modeling process, first the tooth surface of member gear is modeled with genuine cutter, and then the pinion tooth surface is generated, and finally tooth contact of genuine gears are compared to the tooth contact of simplified hypoid gears.

In this work an accurate approach to modeling the genuine tooth surfaces of genuine tooth surfaces for the face-milled spiral bevel and hypoid gears is proposed. With accurate surface model, high speed face milling process becomes possible to be used as the gear tooth finishing process. When the accurate gear tooth surface is used in gear roughing process, the remaining material and residual stress on the roughed stock are distributed equally. It can decrease the workload on the finishing cutter, thus the cutter

life is prolonged. The accurate NURBS gear tooth surfaces can also be conveniently used by the FEA process.

ACKNOWLEDGEMENTS

I would like to express my sincere thanks and gratitude to my supervisor Prof. Chevy Chen for his invaluable guidance, support and enthusiasm throughout this work. I have gained valuable research experience and significantly improved my technical skills under his supervision.

Thanks to my fellow graduate students, Fu Qiang, Maqsood Ahmed Khan, Muhammad Wasif, Mahmoud Rababah, Aqeel Ahmed, Jiang Zhu, Chun Du, Liming Wang, Ge Song, Sherif Abd Elkhalek, Yuansheng Zhou, Haiqing Liang, Huang Guogui, and Zheng Hong, for providing all sorts of help and creating an excellent working atmosphere.

Finally, I dedicate this work to my parents, my wife and daughter for their never-ending love and support.

Table of Contents

List of Figures

List of Tables

Chapter 1 Introduction

1.1 Research Problems

Spiral bevel and hypoid gears are composed of member gear and pinion normally with 90 degree shaft angle, and massively used in automobile and helicopter industry for transformation of the rotation and torque. The high quality gears with low noise, smooth transformation, and low transmission errors are required higher gear tooth accuracy. Currently face milling and face hobbing are two main ways to manufacture the spiral bevel and hyoid gears. In the traditional spiral bevel and hypoid gears machining process, face milling is always followed with grinding as the finishing process, so the face milling does not affect the accuracy of the finished tooth surface. With the high speed milling technology development, the face milling may use in the tooth finishing process, which put forward a higher requirement on accuracy for the face-milled tooth surface. The accurate tooth surface for the tooth roughing is also important. If the roughing tooth surface is accurate, the residue stress will distribute equally on the gear stock, and also the workload on the cutter will be reduced, thus the life of gear cutter will be prolonged.

There are two problems in current face-milled spiral bevel and hypoid gears machining process. First, in the gear tooth generation the simplified cutter geometric model is used [1]. This simplification may result in the geometric error on the gear tooth surface. For the simplified cutter, at the beginning people defined the side cutting edges

(SCE) as two straight lines located on the blade normal plane (see Fig. 1.1). The simplified blade model was improved by taking the circular cutting edge (CCE) into consideration, and its side cutting edge was treated as parabolic profile, but the cutting edges are still on the normal plane.

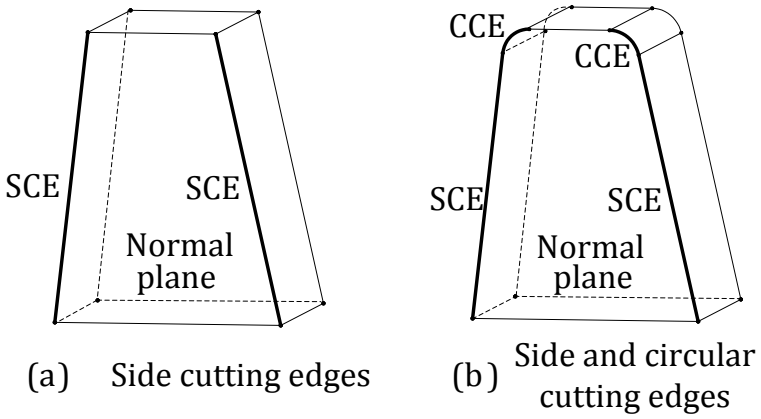

Figure 1.1 Simplified blade geometric models.

Second, current representation of gear tooth cannot be easily and accurately implemented in CAD software, especially the pinion teeth are represented as two equations with three parameters. For the generated gear tooth method, the gear tooth can be represented as [1]

$$\begin{cases} r_g = M_{gc}(\phi) \cdot r_c(u,\theta) \\ f = n_g \cdot v_{gc} \end{cases}. \tag{1.1}$$

r_g represents the family of tool surface in gear coordinate system, and it can be obtained by transforming tool surface r_c from cutter coordinate system to pinion coordinate system by matrix M_{gc}. The equation f is the mesh equation in the pinion generation, which represents during the machining process the tool surface and pinion tooth surface

have the same normal n_g, and the normal is perpendicular to their relative velocity v_{gc}. Although some researcher try to calculate the sampling points from the above equations, and fit them in CAD software, but the accuracy cannot be guaranteed.

1.2 Research Objectives

The goal of this work is to build up the genuine tooth surface for spiral bevel and hypoid gears. From the above problem analysis, we know that the simplified blade model may cause the geometric error for the gear and pinion tooth. The first objective of this work is to build up the genuine cutter geometric model. The cutting edges of the genuine cutter are defined on the rake plane by parameters the blade angle, rake angles and relief angles, rather than the cutting edges of simplified cutter are defined on the cutter normal plane. In this work the mathematic cutter model is build up, and the geometric error of the simplified cutter is analyzed.

The second objective is to build up the accurate gear and pinion tooth surface by using the genuine cutter geometric model. First, by using the genuine cutter geometric model we develop the member gear tooth surface based on the kinematics of the non-generated gear tooth machining process. Second, we generate the pinion tooth surface with the genuine pinion cutter and kinematics of pinion generation process. The tooth surfaces of member gear and pinion are accurately represented as NURBS surfaces by optimize the number of sampling points and control points. The NURBS tooth suface can be directly implemented into current CAD software, and provide the accurate geometry for the following gear tooth FEA.

In industry, people model the gear and pinion tooth surfaces, and calculate the machine setting, after that machine the real parts. If the real tooth meshing deviates from the designed pattern, they need to manually adjust the machine setting, but it takes long time; or use the simulation to adjust the machine settings, but the current tooth geometry is inaccurate. In this work, since the tooth geometry is fully match with the real machined gear, when can quickly and accurately adjust the machine settings by simulation, which saves time and money.

Finally we calculate the tooth geometric errors, and compare the tooth contact of the genuine gears to the tooth contact of simplified gears. To demonstrate the above methods, examples on spiral bevel gears and hypoid gears machining are conducted.

1.3 Dissertation Organization

The remaining sections of this dissertation are organized as follows. Chapter 2 reviews the current technologies on gear face hobbing, tooth contact analysis and tooth surface optimization. Chapter 3 discusses the face milling process for spiral bevel and hypoid gears machining. Chapter 4 presents the genuine cutter geometric model for spiral bevel and hypoid gears. Chapter 5 presents the accurate tooth surface for the spiral bevel gear generated from genuine cutter geometric model. Chapter 6 presents the accurate tooth surface for the hypoid gear generated from genuine cutter geometric model. Chapter 7 contains the summary of this work.

Chapter 2 Literature Review

2.1 Introduction

Gear machining technology has developed from eldest wooden teeth gear to the today's most complicated hypoid gears. Spiral bevel gears are used to transform rotation and torque between two intersected axes, and hypoid gears are used to transform rotation and torque between two cross axes (Fig. 2.1). The hypoid gears are similar to spiral bevel from tooth geometry and manufacturing process point of views. The hypoid gears have a shaft offset between gear and pinion axes, which make the case more complicated.

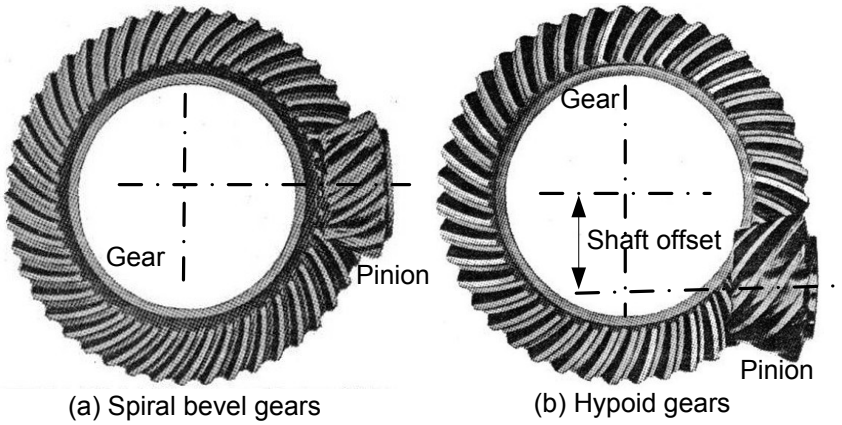

Figure 2.1 Spiral bevel gears and hypoid gears.

There are lots of researchers devote their careers for the gear technology development. Olivier and Gochman developed the basic theory about the generation of conjugated gear tooth surface. Wildhaber developed the theory of hypoid gear drives. Dudley wrote the first edition of Gear Handbook [2], and it is intensively used in the industry. Dr. Litvin, a great scientist, did a great contribution to the modern gear theory.

This work is based on the developed gear theory and gear manufacturing, which is introduced in detail in Chapter 3.

Currently there are three major gear machining tool manufacturers. One is Gleason Company in USA, which provides the full service from gear machine, tooling and metrology for all kinds of cylindrical gear and bevel gear. The other two companies are Klingelnberg and Oerlikon in Europe. They are famous for the continuous indexing face hobbing method in spiral bevel and hypoid gears machining. There are two popular ways to machine spiral bevel and hypoid gears. First method is the gear tooth rough machined by face milling, and then finish grinded. This method is mainly applied on Gleason PHOENIX® machine [3]. Another method is rough machined by face hobbing, and hard-cutting for finish. This method is mainly applied on Klingelnberg and Oerlikon's machine [4, 5]. Most of researches are focusing on these two methods. Since now days the flexible multi-axis CNC milling machine are massively used in the industry, people start to consider the gear machining on the general CNC milling machine. Suh proposed a ¾ axis or additional four-axis milling machine to manufacture the sculptured tooth surface of spiral bevel gear [6, 7]. In the work, the gear tooth geometry was build up, and the process planning and tool path planning were developed. Safavi proposed a three-axis CNC milling machine interfaced with an additional PLC module to machine the spiral bevel gear [8]. Özel also tried to machine the spiral bevel gear using the optimized cutting tool and machining parameters using end mill by CNC milling machine [9]. Kawasaki investigated the accuracy of straight bevel gear manufactured by using general CNC milling machine [10]. For the spiral bevel gear machining by using CNC milling machine, people don't need to invest huge money on specific bevel gear machine

since the general CNC milling machine is used, but the accuracy is difficult to achieve, and takes longer time compared to the specified cradle machining method. Face milling process will be introduced in the next chapter in detail. In this chapter, we will introduce the face hobbing process, the methods for tooth optimization and tooth contact analysis.

2.2 Face Hobbing

Face hobbing is a continuous generating process for the spiral bevel and hypoid gear manufacturing, unlike single indexing of the face milling process which gear tooth has to be cut one by one. Compare to face milling process, one of the advantages is the tooth curvature can be easily controlled by changing the kinematics of face hobbing index motion. While for the non-generated face milling process, the tooth curvature is determined by the blade geometry and cutter radius. The disadvantages are the finish grinding cannot be applied to the face-hobbed tooth, and the face milling process has higher productivity.

Although face hobbing process was invented one century before, the mathematical model for face hobbing and computerized tooth representation and contact is proposed around 2006 [11-14]. The face hobbing methods can be implemented on Klingelnberg's Cyclo-Palloid© system, Oerlikon's Spirac© and Spiroflex© systems, or Gleason's hypoid generator with TRI-AC® and Pentac® face hobbing cutters.

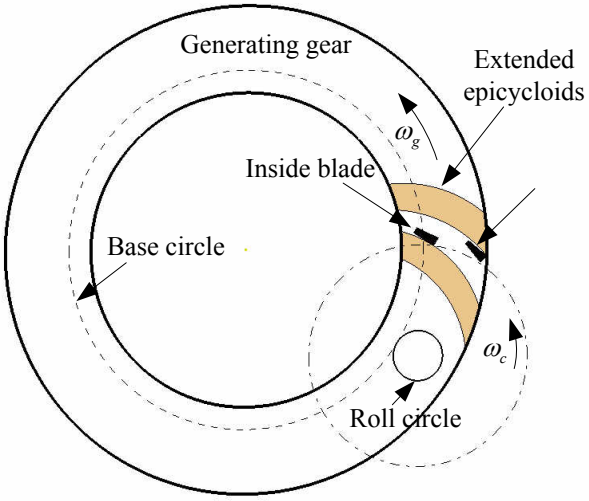

Figure 2.2 Kinematics of face hobbing tooth generation.

The kinematics of face hobbing tooth generation is shown in Fig. 2.2. The relative between generating gear and tool surface is extended epicycloids. Assume N_g is the gear teeth number, and N_c is the blade number. The angular velocity of gear and blade are ω_g and ω_c respectively. The relationship should be satisfied as

$$\frac{\omega_g}{\omega_c} = \frac{N_c}{N_g}. \tag{2.1}$$

The face hobbing head cutter is composed of a group of inside and outside blades, which are alternatively mounted on the cutter plate. When building up the hobbing cutter, only the rake angle and blade angle are considered.

Once we have the kinematics model of gear generation and the blade geometry, the gear tooth can be represented as

$$\begin{cases} r = r_g\left(u,\theta,\phi\right) \\ f = n_g \cdot v_g = 0 \end{cases}, \tag{2.2}$$

Here, r_g represent the surface generated by the relative motion of blade in gear coordinate system. u is the parameter of cutting edge. θ is the cutter rotation angle, and ϕ is the cradle rotation angle. f represents the point on the gear tooth surface satisfies the mesh equation, which means that the normal direction should be perpendicular to the relative velocity between points on the gear tooth and blade. Once the gear and pinion tooth surfaces are obtained. Tooth contact analysis (TCA) can be conducted. The main job of TCA is to check the transmission error and contact pattern. The stress distribution on the flank and fillet also can be predicted by using FEA method.

The face hobbing gear tooth generation process shows that the final tooth contact is affected by the blade geometry, and kinematics model. Fan proposed a modified machine settings to minimize the tooth surface geometric errors due to the machining dynamics and tolerances of machine tools [14]. But currently there is no work to consider the geometric error caused by the blade model since only the rake angle and blade angle are considered in the modeling, and also no optimization on the blade geometry.

2.3 Tooth Contact Analysis

After generating the gear and pinion tooth, the next step is to tooth contact analysis (TCA). We categorize the TCA into the following subjects: tooth surface modeling, tooth measurement, tooth contact analysis and stress calculation, surface crack, tooth vibration.

Gear tooth geometric modeling is the fundamental of tooth contact analysis. In Litvin's work the parametric equations of gear and pinion tooth surface are provided. The generated gear tooth is represented as two equations and three parameters [1]. Yanwei built up the spiral bevel gear machining model in the machining simulation software VERICUT [15]. In the virtual machining environment, the blade and blank geometric model, and the kinematics of gear generation are built up. By through simulating the material removal process, they achieve the final gear geometry. This method is a simply and quick way to achieve the gear geometry, and also from the simulation we can observe the material removal process. The drawback is that the accuracy of the gear tooth can be guaranteed. Yanwei also proposed another method to build tooth geometric model. From the generated gear tooth equations the dozens of sampling points are calculated, and use a NURBS surface to interpolate these points in the CAD software Isight [16]. Zhaowen did the same work in Pro/E [17]. This method has the same drawback as the above method. The accuracy of the tooth geometry cannot be guaranteed.

Due to the random error in the gear tooth machining process, the geometric error exists on the gear tooth. The big gear machine manufactures have their own gear measuring machine such as Gleason [3]. The measuring method is classified for different companies. There are also some general methods to measure the geometric errors of gear tooth. Suh proposed a virtual gear model [18]. In this model, the sampling points were measured by using CMM, and fitted by NURBS surface. Compare the virtual gear model to the theoretic model, the geometric error was evaluated. Weimin developed a accurate way to measuring the spiral gear tooth by optimize the measuring process parameters [19].

The tooth contact pattern is the status of how the gear teeth contact at the instantaneous moment and continuous meshing process. Litvin proposed the approach to determine the direction and length the instantaneous contact line with Euler-Rodrigues' formula [1]. According to Rodrigues's formula, the principal curvatures of point on surface can be represented as $\kappa_{\text{I,II}} \cdot v_r = -i$. In the equation v_r is the velocity and i is derivative of normal, vector v_r and i are collinear for the principal direction. Euler's equation build up the relation between normal and principal curvatures of a surface, which is $\kappa_n = \kappa_{\text{I}} \cdot \cos^2 q + \kappa_{\text{II}} \cdot \sin^2 q$. Under the workload, the instantaneous contact between gear and pinion tooth is an ellipse centered at the contact point. With the above two equation, we can derive the direction of contact point moving, and the orientation and major length of the ellipse. With the gear continuous rotations, the bearing contact is a set of contact ellipses. Kolivand use ease-off topography and shell theory to analyze the tooth contact for the unloaded and loaded tooth [20, 21]. The ease-off approach can be explained as tooth contact analysis directly from the tooth geometry of gear and pinion, other than from the principal directions and curvature. In this method the local mesh area is defined first, and then the gear and pinion tooth surface within this area projected on a projection plane. By analysis the projection we can predict the real contact status. This method is straight forward compared to the traditional tooth contact analysis except huge calculation work required.

Due to the periodic loading condition, the tooth failure maybe happened on the gear tooth. The tooth failures may exist in form of fatigue failure at the tooth root, or flank crack. Guagliano researched on the flank crack due to rolling contact fatigue [22,

23]. In their work the crack growth mechanism was proposed. The contact pressure is evaluated first, and the stress intensity factors are calculated using the finite element, finally find the direction of crack propagation. Ural predicted the crack growth combining the parallel finite element methods and plasticity-induced fatigue crack closure and moving loads, which is better representation the moving load and significantly reduced the computation time for simulation [24]. Hotait investigated on the stress on the gear root. In the work, the effects of different misalignment were predicted with the proposed model, and verified with experiments [25].

Transmission error is the main source of vibration in gear running. Cheng derived a new gear mesh coupling formula, and using model free and forced vibrations in the transmission error excitation are examined [26]. In the experiment, the effects of design parameters on the dynamic characteristics and vibration response are investigated. Teik proposed a nonlinear, time-varying, 3-dimensional gear mesh coupling dynamic model for hypoid gear pair [27]. Pei-Yu provided a model of 3D dynamic contact and impact analysis of spiral bevel gear drives [28]. In the work finite element is used to calculate the transmission error and surface contact stress, and a dynamic model is applied to analyze the response in time varying. Yoon investigate the vibration caused by transmission error experimentally [29].

2.4 Optimization on Tooth Surface

Tooth contact between gear and pinion is mainly determined by the tooth geometry if the gear installation error is neglected. There are several factors which may

affect the final tooth geometry. Since face hobbing and face milling are both using the cradle method, the factors are effective for both of them. For the generated gear tooth method, the gear tooth can be represented as [1]

$$\begin{cases} r_g = M_{gc}(\phi) \cdot r_c(u,\theta) \\ f = n_g \cdot v_{gc} \end{cases}. \tag{2.3}$$

r_c is the tool surface, and M_{gc} is the transformation matrices. ϕ is the cradle rotation angle, ϕ is related to generated gear rotation angle ϕ_g as $\phi = m_{cp}(\phi_c)$, this is also called roll ratio. f is the mesh equation, which represent the normal direction of contact point on gear surface and tool surface should be perpendicular to the relative velocity direction. From the above equation we can observe that the cutter geometry, machine settings, roll ratio are directly related to the generated gear tooth geometry.

Gosselin proposed an algorithm to calculate the machine settings producing a theoretical tooth surface, which is match with the real tooth surface [30]. In the work, the generated gear tooth machining process is considered as a black box system. The input is the machine settings, and output is the real tooth surface. The geometric error between real and theoretic gear tooth is used to adjust the machine settings. At the beginning of machining, the initial tooth surface is produced by using the calculated machining setting from traditional method. CMM machine is used measure the geometry of the machined gear tooth. By calculate the distance between theoretic and machined gear tooth we can evaluate the geometric error. The next step is to adjust the machine settings up to the geometric error is within tolerance. Chung-Yunn optimized the machine setting by using

the sensitivity study [31, 32]. This method is effective and practicable in the industry. There are many factors may cause the geometric error of the tooth surface, and it is difficult to discover the real reason behind this error. The simplest ways is treated it as black box system. Through changing the machine settings which may cause the geometric error, we can observe the effect on the tooth geometry. The disadvantage of the method is time consuming since lots of trials and repeated measurement are taken.

The kinematic error of face-milled gear is a parabolic function [1]. Zhang-Hua proposed a fourth-order motion curve, which can reduce the impact at the transfer point at adjacent mating teeth [33]. In this work, the modified radial motion correction is introduced in the calculation of machining settings, with the modified radial motion, the contact position, motion curve and contact path bias can be controlled independently, which allow us easily achieve the different desired contact patterns.

Cutting tool is major factor affecting the accuracy of gear tooth. Simon proposed an optimized circular tool profile arcs and the diameter of cutter for hypoid pinion teeth [34, 35]. With the optimized tool, the contact pressure and angular position error are reduced. Fan optimized the face cone for the spiral bevel and hypoid gears, which maximize the contact ratio, and at the same time avoid the root-tip interference [36]. Jinliang optimized the pitch cone for hypoid gear to improve the strength of the gear teeth [37].

2.5 Summary

In this chapter, we review the current techniques related to spiral bevel and hypoid gear machining. One of the main machining process face hobbing is introduced, The kinematics of gear generation, the cutter geometry, tooth surface generation related face hobbing are represented. After that, the tooth contact analysis including gear tooth geometry modeling, measurement on tooth surface, tooth contact pattern, tooth crack and vibration is represented. Finally the optimization on the gear tooth surface is discussed from machine settings, modified radial motion, cutting tool and gear geometry point of views. The Tooth contact analysis and optimization techniques are effective both for face milling and face hobbing process. In the following chapter, the current face milling process used in this work will be introduced.

Chapter 3 Manufacturing Process of Face-Milled Spiral Bevel and Hypoid Gears

3.1 Introduction

In this chapter, the design and manufacturing process of spiral bevel and hypoid gears by face milling are discussed. The contents introduced in this chapter are all coming from Dr. Litvin's research group. His team contributed more than 60 high quality journal paper, 7 NASA reports, one book on gear geometry and theory. His research covered the design and manufacturing of spur [38-41] and helical gears [39, 42-46], worm gear [40, 47-49], screw compressor [50], spiral bevel gear and hypoid gear. In the gear theory, he proposed the determination of the conjugated gear surface from curvature relations, determination of envelope singularities, computer aided tooth contact analysis, low noise misaligned gear drives and so on [1]. These methods lay down a theoretical foundation for modern computer aided gear design and manufacturing.

Spiral bevel gear design and manufacturing process is a very complicated process because of its non-standardized, complex geometry, and tooth contact. It takes time and costly. So normally before manufacturing the gears people will modeling the gear geometry and do TCA (tooth contact analysis). Litvin published one important paper consisting of three parts on journal of Mechanical Design in 1981 for the manufacturing

of hypoid [51-53]. This is the most important paper introduced the detail how the hypoid is machined with Formate and Helixform methods up to now. Most the following works are based on this paper.

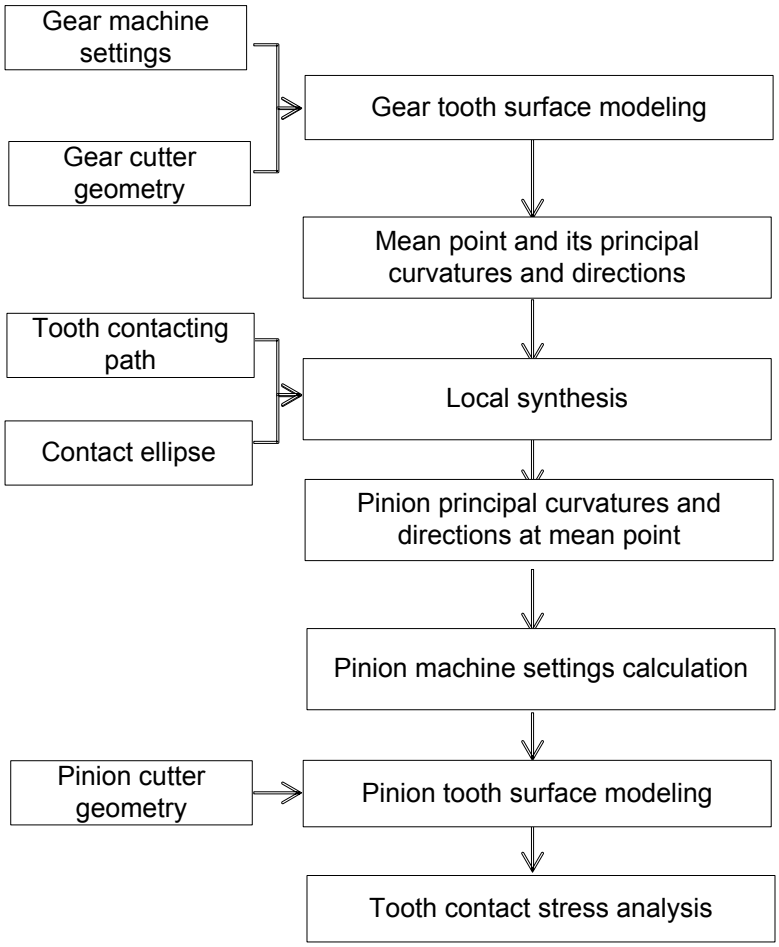

Figure 3.1 Hypoid gear surface modeling process

Fig. 3.1 shows the hypoid gear surface modeling process. The first step is to determine the gear tooth surface. In the second part, based on the member gear tooth, the machine setting for the pinion are calculated, and in the final part, tooth contact analysis is conducted, and the synthesis is optimized. In the papers related to spiral bevel gear manufacturing, the gear tooth surface is derived from the gear blade geometry, and then

the machine settings for pinion is calculated, and the pinion tooth surface is generated, and finally the transmission errors are calculated, and FEA on the tooth is conducted by using commercial software ABAQUS. Through this procedure, the desirable tooth contact can be obtained, and the low-noise high endurance spiral bevel gears are achieved [54-59].

In this chapter, first we introduce the cutting tool and CNC machine used for face -milled spiral bevel gears and hypoid gears, and then present how to generate the gear and pinion tooth surfaces.

3.2 Simplified Face Milling Cutter

The face milling cutting tool is composed of a group of blades, which are mounted on the cutter plates. Fig. 3.1 shows the Hardac ® cutter from Gleason Company. The blades include inner and out blades, which can be adjusted in both angular and radial planes.

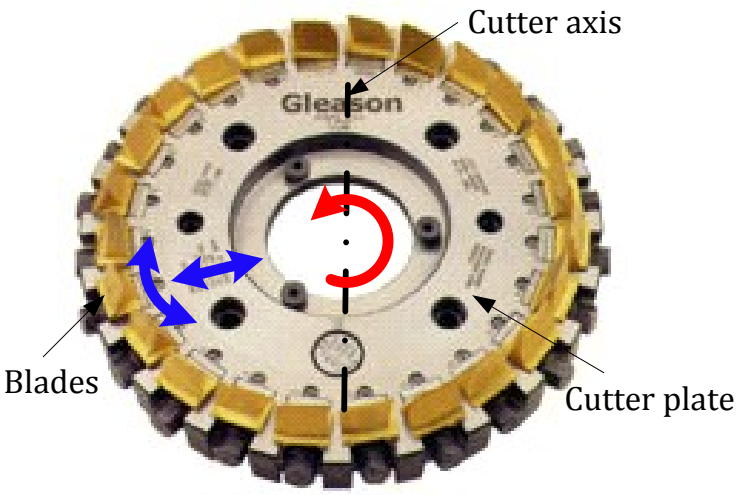

Figure 3.2 Hardac ® cutter from Gleason Company.

The face milling cutters for hypoid gear are massively used in the roughing and semi-finishing process. A blade geometry model was proposed by Litvin, which simplified the side cutting edges (SCE) as two straight lines on the blade installation plane, which passes through the cutter axis. Argyris improved the simplified blade model by taking the circular cutting edge (CCE) into consideration, and proposed the parabolic profile for side cutting edge.

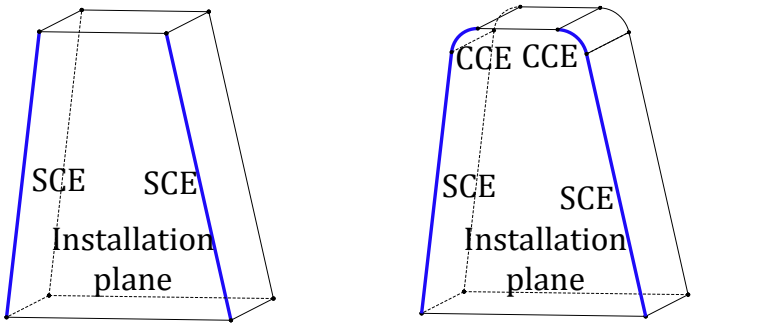

(a) Litvin's blade model (b) Argyris's blade model

Figure 3.3 Simplified blade geometric models.

The simplified blade can be modeled in blade coordinate system $S_b^{(s)}$. Assume p_w is the point width. d_b is depth of blade. $\phi_c^{(s)}$ is the blade angle. r is the corner radius. r_c is the cutter average radius, which is the distanct from $O_b^{(s)}$ to the origin O_c of cutter coordinate system S_c. Curves $M_s^{(i)}L_s^{(i)}$ and $L_s^{(i)}J_s^{(i)}$ are the respective inner SCE and CCE. Curves $M_s^{(o)}L_s^{(o)}$ and $L_s^{(o)}J_s^{(o)}$ are the respective outer SCE and CCE.

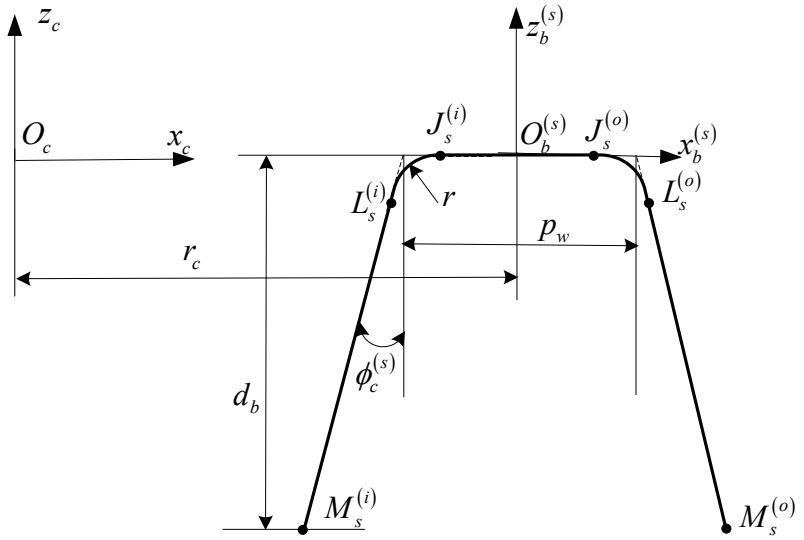

Figure 3.4 Parametric model of simplified blade.

The line $M_s^{(i)}L_s^{(i)}$ can be represented in S_c as

$$\mathbf{L}_{s,s}^{(i)}\left(u_s\right)=\begin{bmatrix} r_c-\dfrac{p_w}{2}-\left[\left(1-u_s\right)\cdot r\cdot\cot\left(\dfrac{\pi+\phi_c^{(s)}}{2}\right)+u_s\cdot\dfrac{d_b}{\cos\phi_c^{(s)}}\right]\cdot\sin\phi_c^{(s)} \\ 0 \\ -\left[\left(1-u_s\right)\cdot r\cdot\cot\left(\dfrac{\pi+\phi_c^{(s)}}{2}\right)+u_s\cdot\dfrac{d_b}{\cos\phi_c^{(s)}}\right]\cdot\cos\phi_c^{(s)} \end{bmatrix} \quad \left(0\le u_s\le 1\right). \tag{3.1}$$

The circular $L_s^{(i)}J_s^{(i)}$ can be represented in S_c as

$$\mathbf{L}_{s,c}^{(i)}\left(\varphi_s\right)=\begin{bmatrix} r\cdot\cos\varphi_s-\dfrac{p_w}{2}+r\cdot\cot\left(\dfrac{\pi+\phi_c^{(s)}}{2}\right)+r_c \\ 0 \\ r\cdot\left(1-\sin\varphi_s\right) \end{bmatrix} \quad \left(\frac{\pi}{2}\le\varphi_s\le\pi-\phi_c^{(s)}\right). \qquad (3.2)$$

The line $M_s^{(o)}L_s^{(o)}$ can be represented in S_c as

$$\mathbf{L}_{s,s}^{(o)}\left(u_s\right)=\begin{bmatrix} r_c+\dfrac{p_w}{2}+\left[\left(1-u_s\right)\cdot r\cdot\cot\left(\dfrac{\pi+\phi_c^{(s)}}{2}\right)+u_s\cdot\dfrac{d_b}{\cos\phi_c^{(s)}}\right]\cdot\sin\phi_c^{(s)} \\ 0 \\ -\left[\left(1-u_s\right)\cdot r\cdot\cot\left(\dfrac{\pi+\phi_c^{(s)}}{2}\right)+u_s\cdot\dfrac{d_b}{\cos\phi_c^{(s)}}\right]\cdot\cos\phi_c^{(s)} \end{bmatrix} \quad \left(0\le u_s\le 1\right). (3.3)$$

The circular $L_s^{(o)}J_s^{(o)}$ can be represented in S_c as

$$\mathbf{L}_{s,c}^{(o)}\left(\varphi_s\right)=\begin{bmatrix} r\cdot\cos\varphi_s+\dfrac{p_w}{2}-r\cdot\cot\left(\dfrac{\pi+\phi_c^{(s)}}{2}\right)+r_c \\ 0 \\ r\cdot\left(1-\sin\varphi_s\right) \end{bmatrix} \quad \left(\phi_c^{(s)}\le\varphi_s\le\frac{\pi}{2}\right). \qquad (3.4)$$

3.3 CNC Machine Used for Gear Face Milling

The spiral bevel and hypoid gears can be machined by “Phoenix” CNC machine. This kind of special machine has hypoid generation function. The machine has to be

adjust to make sure the cutter and workpiece in right positions, which are called machining settings. The machine settings include γ_m (machine root angle), ΔA (gear center to back), ΔB (machine center to back), ΔC (blank offset), S_r (radial setting), q (radial angle) and i (radial angle). The machine can provide three rotations and two linear motions. This machine can be used to produce the non-generated gear, in which one tooth machining process the workpiece and cradle keep stationary, and only the work table feeds to remove the material. When the generated gears or pinions are machined, the rotation of workpiece and cradle are related with certain ratio. By using face milling machine the gear teeth are machined one by one.

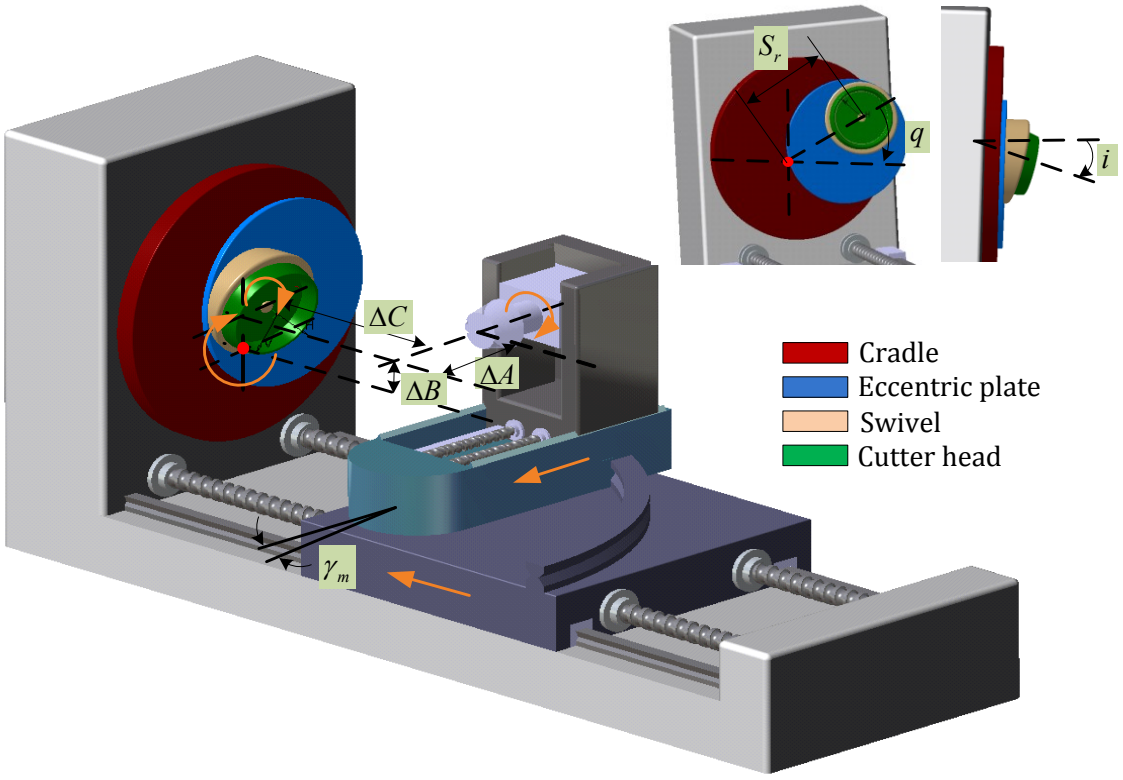

Figure 3.5 CNC machine for spiral bevel and hypoid gears.

3.4 Gear and Pinion Generating Process

It becomes possible to generate the complicated conjugate teeth surfaces. To achieve the desire the mesh and contact condition by using this type of machine is not an easy job. Litvin proposed a procedure to produce the low noise of spiral bevel and hypoid gears by application of predesigned parabolic function of transmission error. In conclusion, the approach includes the following steps.

3.4.1 Generation of the Gear Tooth Surface

Assume we know the cutting edges of the gear blades $\mathbf{L}_{s,s}^{(g,i)}(u_s)$, $\mathbf{L}_{s,s}^{(g,o)}(u_s)$, $\mathbf{L}_{s,c}^{(g,i)}(\varphi_s)$ and $\mathbf{L}_{s,c}^{(g,o)}(\varphi_s)$. the tool surface is the revolution of the cutting edges about the cutter axis z_c. Since here non-generated method is used to produce the gear tooth surface, the gear tooth surface can be achieved by transferring the gear tool surface from S_{gc} to gear coordinate system S_g, which are represented by the equations

$$\begin{cases} \mathbf{G}_{s,s}^{(i)}(u_s,\theta_s) = M_{gc}\cdot\mathbf{T}_{s,s}^{(g,i)}(u_s,\theta_s) = M_{gc}\cdot M_{rc}(\theta_s)\cdot\mathbf{L}_{s,s}^{(g,i)}(u_s) \\ \mathbf{G}_{s,c}^{(i)}(u_s,\varphi_s) = M_{gc}\cdot\mathbf{T}_{s,c}^{(g,i)}(u_s,\varphi_s) = M_{gc}\cdot M_{rc}(\theta_s)\cdot\mathbf{L}_{s,c}^{(g,i)}(\varphi_s) \\ \mathbf{G}_{s,s}^{(o)}(u_s,\theta_s) = M_{gc}\cdot\mathbf{T}_{s,s}^{(g,o)}(u_s,\theta_s) = M_{gc}\cdot M_{rc}(\theta_s)\cdot\mathbf{L}_{s,s}^{(g,o)}(u_s) \\ \mathbf{G}_{s,c}^{(o)}(u_s,\varphi_s) = M_{gc}\cdot\mathbf{T}_{s,c}^{(g,o)}(u_s,\varphi_s) = M_{gc}\cdot M_{rc}(\theta_s)\cdot\mathbf{L}_{s,c}^{(g,o)}(\varphi_s) \end{cases}. \tag{3.5}$$

Here M_{gc} is the transforming matrix from S_c to S_g, and $M_{rc}(\theta_s)$ is the matrix when the cutting edges revolve about the z_c.The unit normal to the gear surface can be represented by the equations

$$\begin{cases} \mathbf{n}_{s,s}^{(g,i)}\left(u_s,\theta_s\right)=\dfrac{N_{s,s}^{(g,i)}}{\left|N_{s,s}^{(g,i)}\right|}, & N_{s,s}^{(g,i)}=\dfrac{\partial \mathbf{G}_{s,s}^{(i)}}{\partial u_s}\times\dfrac{\partial \mathbf{G}_{s,s}^{(i)}}{\partial \theta_s} \\ \mathbf{n}_{s,c}^{(g,i)}\left(u_s,\varphi_s\right)=\dfrac{N_{s,c}^{(g,i)}}{\left|N_{s,c}^{(g,i)}\right|}, & N_{s,c}^{(g,i)}=\dfrac{\partial \mathbf{G}_{s,c}^{(i)}}{\partial u_s}\times\dfrac{\partial \mathbf{G}_{s,c}^{(i)}}{\partial \theta_s} \\ \mathbf{n}_{s,s}^{(g,o)}\left(u_s,\theta_s\right)=\dfrac{N_{s,s}^{(g,o)}}{\left|N_{s,s}^{(g,o)}\right|}, & N_{s,s}^{(g,i)}=\dfrac{\partial \mathbf{G}_{s,s}^{(o)}}{\partial u_s}\times\dfrac{\partial \mathbf{G}_{s,s}^{(o)}}{\partial \theta_s} \\ \mathbf{n}_{s,c}^{(g,o)}\left(u_s,\varphi_s\right)=\dfrac{N_{s,c}^{(g,o)}}{\left|N_{s,c}^{(g,o)}\right|}, & N_{s,c}^{(g,i)}=\dfrac{\partial \mathbf{G}_{s,c}^{(o)}}{\partial u_s}\times\dfrac{\partial \mathbf{G}_{s,c}^{(o)}}{\partial \theta_s} \end{cases}. \tag{3.6}$$

3.4.2 Local Synthesis

After determination the gear tooth surface, the next step is to derive the pinion machine settings. First we find a mean point on the gear tooth surface, and then find the relative position between gear and pinion, finally calculate the pinion machine settings based on input parameters of local synthesis.

- Finding the mean point

Mean point will be the tangency of gear and pinion tooth surface. Here we assume the M_g^* is on the flank of convex side of gear tooth. M_g^* and the normal to $\mathbf{G}_{s,s}^{(i)}$ at M_g^* can be represented as

$$\begin{cases} M_g^*=\mathbf{G}_{s,s}^{(i)}\left(u_s^*,\theta_s^*\right) \\ n_g=\mathbf{n}_{s,s}^{(g,i)}\left(u_s^*,\theta_s^*\right) \end{cases}. \tag{3.7}$$

- Calculating the angle ϕ^*

For the spiral bevel gear with perpendicular shaft, the relative position between gear and pinion is decided by angle ϕ^* (Fig. 3.5). Angle ϕ^* can be calculated from the meshing equation between gear and pinion tooth, which is

$$n_g\left(\phi^*\right)\cdot v_{gp}\left(\phi^*\right)=0. \tag{3.8}$$

Here n_g is the common normal of gear and pinion at the mean point M_g^*, and v_{gp} is the relative velocity at M_g^*, which can be calculated from the gear ratio

$$\omega_{gp}=\frac{\omega_g}{\omega_p}. \tag{3.9}$$

ω_g is the angular velocity of gear, and ω_p is the angular velocity of pinion.

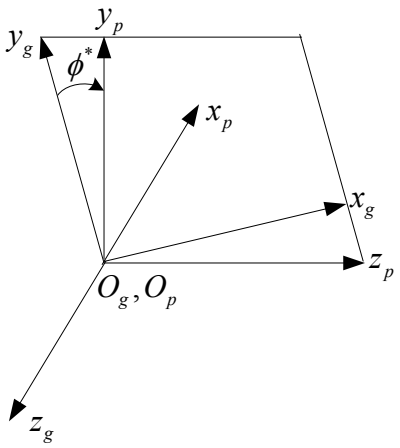

Figure 3.6 Relative position between S_g and S_p.

- Finding the curvatures of the pinion tooth at mean point M_g^*.

With the gear tooth surface $\mathbf{G}_{s,s}^{(i)}$ and the mean point M_g^*, we can find the principal curvatures k_g^1, k_g^2 and the corresponding principal directions Assume the principal directions τ_g^1 and τ_g^2. The local synthesis is trying to find the optimized pinion tooth surface which satisfies the designed meshing situation. The designed mesh situation is illustrated in Fig. 3.6. It is given as the input of the local synthesis. It defined the angle ε between principal direction of gear and the tangent to the tooth contacting path, and the length of major axis a of the contact ellipse at M_g^*.

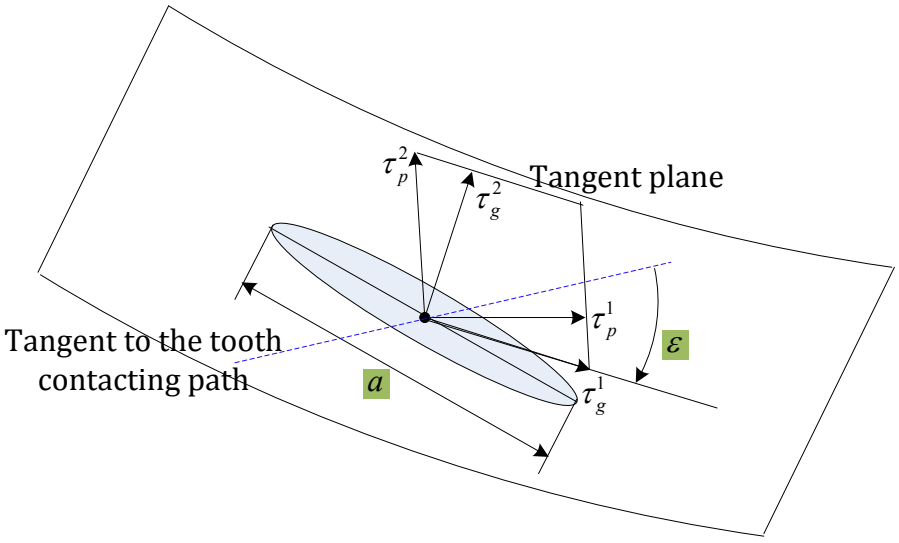

Figure 3.7 Local synthesis between gear and pinion tooth surfaces.

With the parameters k_g^1, k_g^2, τ_g^1 ,τ_g^2, ε and a, we can find the principal curvatures k_p^1, k_p^2 and directions τ_p^1, τ_p^2 of pinion from the local synthesis equations

$$\begin{cases} v_g = v_p + v_{pg} \\ \cdot \qquad \cdot \qquad n_g \\ \dfrac{d\left(n_g \cdot v_{gp}\right)}{dt} = 0 \end{cases} \tag{3.10}$$

The first two equations are to make assure that the gear and pinion tooth has a continuous tangency. The last equation is the differentiated equation of meshing.

3.4.3 Determination of Pinion Machine Settings

Once we have k_p^1, k_p^2, τ_p^1 and τ_p^2, it is possible to determine the pinion machine settings, which include machine offset, sliding base, machine center to back, machine root angle, radial setting, installation angle and ratio of cutting. It is also possible to decide the two pinion surface parameters and one cutter parameter. All the machine settings are decided from the following equation

$$\begin{cases} M_p^* = M_c^* \\ n_p \cdot v_{pc} = 0 \\ f\left(k_p^1, k_p^2, k_c^1, k_c^2\right) = 0 \end{cases} . \tag{3.11}$$

First equation means the pinion has a common mean point with the pinion cutter. The second equation shows that the pinion tooth and cutter surface should satisfy the mesh equation at mean point. The last equation represents the curvature relations between pinion tooth surface and pinion cutter surface.

3.4.4 Generation of Pinion Tooth Surface

From above section we can get the cutting edges of pinion blades $\mathbf{L}_{s,s}^{(p,i)}(u_s)$, $\mathbf{L}_{s,s}^{(p,o)}(u_s)$ $\mathbf{L}_{s,c}^{(p,i)}(\varphi_s)$ and $\mathbf{L}_{s,c}^{(p,o)}(\varphi_s)$. The pinion flank on convex side can be represented as

$$\begin{cases} \mathbf{P}_{s,s}^{i}(u_s,\theta_s,\varphi_1) = M_{pc}(\varphi_1)\cdot\mathbf{T}_{s,s}^{(g,i)}(u_s,\theta_s) = M_{pc}(\varphi_1)\cdot M_{rc}(\theta_s)\cdot\mathbf{L}_{s,s}^{(g,i)}(u_s) \\ n_p\cdot v_{pc} = 0 \end{cases} . \quad (3.12)$$

Here, first equation is to transform the pinion tool surface from S_{pc} to S_p. The parameter φ_1 is the pinion rotating angle, which is related to the cradle angle. The second equation is the meshing between pinion cutter and pinion tooth surface.

Chapter 4 Genuine Cutter Geometric Model for Face-milled Spiral Bevel Gears and Hypoid Gears

4.1 Introduction

Spiral bevel and hypoid gears are massively used in automobile industry for transformation of the rotation and torque. The high quality gears can work with low noise, smooth transformation, and low transmission errors. In the traditional face-milled spiral bevel and hypoid gears, face milling process is always followed with grinding as the finishing process, so the face milling does not affect the accuracy of the finished tooth surface. In this kind of scenario, people can use the simplified cutter model in machine setting calculation and tooth machining simulation because it will not affect the final tooth surface. With the high speed milling technology development, the face milling may replace the grinding in the tooth finishing process. High speed milling can provide a very close tool surface as the grinder continuous tool surface, but currently the simplified cutter model causes the geometric error, which will affect the final tooth surface, thus the accurate representation of the cutter geometry is critical and essential for the face milling used for the gear tooth surface finishing. The accurate roughing tooth surface is also important. Since for the accurate roughing tooth surface the residue stress and remaining material is equally distributed on the stock, it will reduce the workload for the finishing cutter, thus the life of gear cutter will be prolonged.

In this chapter an accurate cutter geometry model for the face-milled spiral bevel and hypoid gears process was build up. First, the parametric model of the cutter is build up with cutter geometric parameters, such as rake angles, relief angles. With this model we can accurately describe the real cutter geometry used in industry. To compare the simplified cutter to the genuine cutter, the cross sections of their tool surfaces on normal plane are calculated. Finally, some examples are rendered to demonstrate the geometric error of the simplified cutter.

4.2 Cutter Geometric Model

The cutter for the face-milled spiral bevel and hypoid gears is composed of a group of blades, which are mounted on the cutter plates. At the beginning people use a simplified blade geometric model, which simplifies the side cutting edges (SCE) as two straight lines on the blade normal plane (see Fig. 1.1). The simplified blade model was improved by taking the circular cutting edge (CCE) into consideration and its side cutting edge was treated as parabolic profile, but the cutting edges are still on the normal plane.

For the real blade for face-milled spiral bevel and hypoid gears used in industry (see Fig. 4.1), its cutting edges are located on the blade rake face, which is determined by blade rake angles and relief angles, and form a angle with the normal plane, on which the cutting edges of simplified blade are defined.

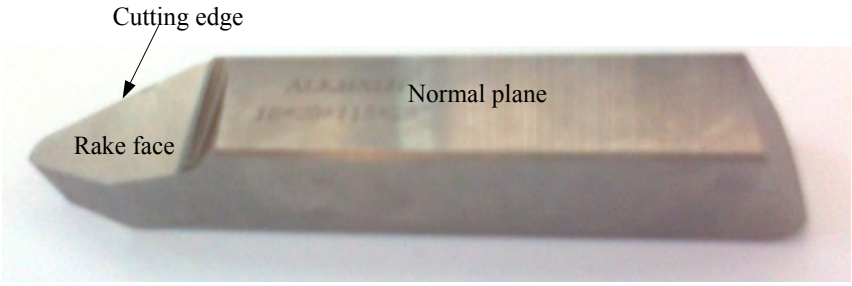

Figure 4.1 Real blade for face-milled spiral bevel and hypoid gears.

Different companies have their own blade product. “Gleason” company provides several types of blades for face milling such as RIDG-AC, WEDGE-AC, HELIXFORM, HARDAC, SOLID, and RSR. These blades have different features. One blade parametric model can used to represent the cutting edge profiles (see Fig. 4.2).

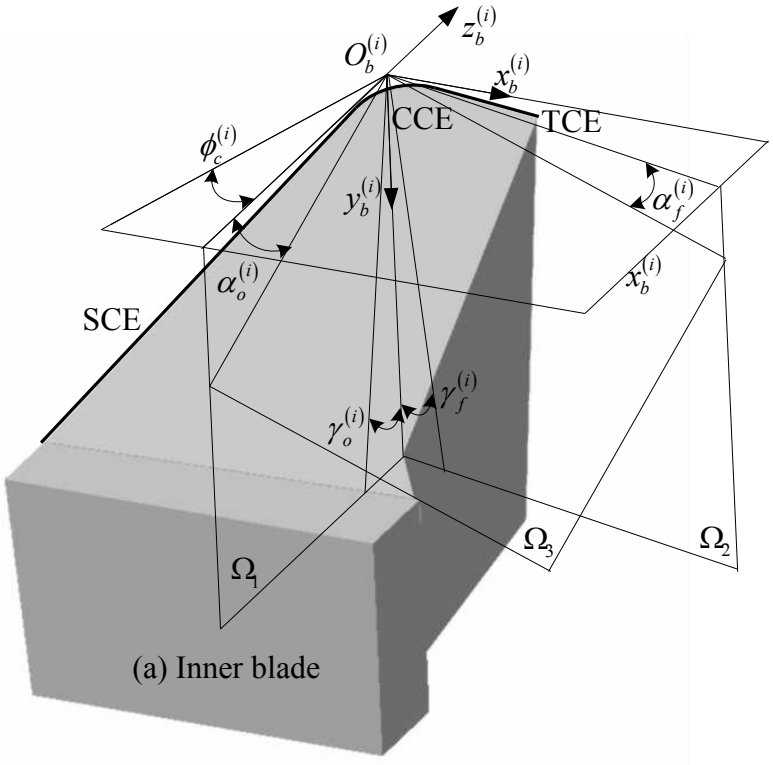

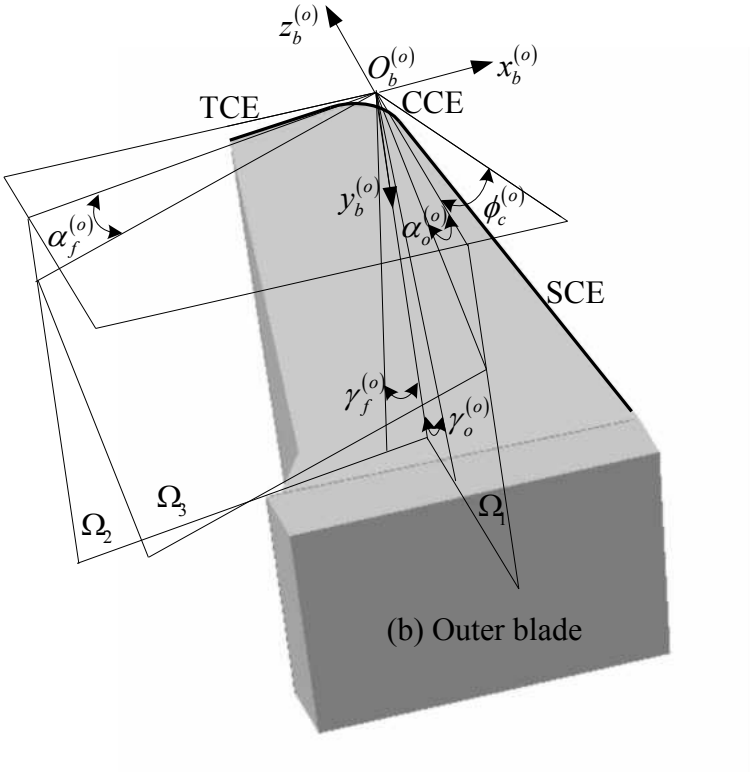

Figure 4.2 Blade parametric model.

The blades include inner blade and outer blade, which are respectively generating the convex and concave gear tooth surface. The parametric model is defined by blade angle (ϕ_c^i, ϕ_c^o), back rake angle (α_o^i, α_o^o), side rake angle (α_f^i, α_f^o), end relief angle (γ_o^i, γ_o^o) and side relief angle (γ_f^i, γ_f^o). In the following section it will introduce how to use these geometric parameters to build up the genuine blade geometry.

4.3 Representation of Inner Blade in Blade Coordinate System

The inner blade is defined in the coordinate system $S_b^{(i)}$. The origin $O_b^{(i)}$ is at the intersection of $\mathrm{TCE}^{(i)}$ (top cutting edge) and $\mathrm{SCE}^{(i)}$ (side cutting edge). Plane $x_b^{(i)} z_b^{(i)}$ is

coincident to the normal plane. $z_b^{(i)}$ is perpendicular to the cutter plate, and $y_b^{(i)}$ is parallel to cutting velocity. Axis $x_b^{(i)}$ is the cross product of $y_b^{(i)}$ and $z_b^{(i)}$ by the right hand rule.

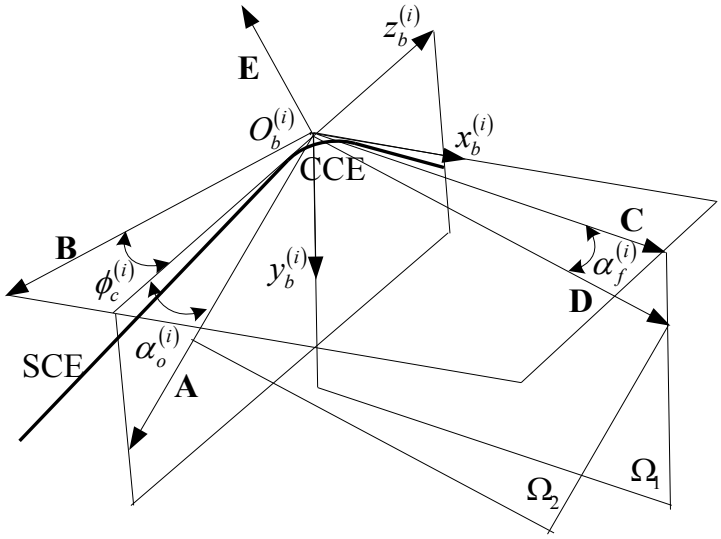

Figure 4.3 Rake plane of inner blade.

According to the definition of back rake angle α_o, it is formed by $z_b^{(i)}$ axis and vector $\mathbf{A}$, which is located on $y_b^{(i)} z_b^{(i)}$ plane (see Fig. 4.3). The unit vector $\mathbf{U}_A$ along $\mathbf{A}$ is

$$U_A = \begin{bmatrix} 0 \\ \sin\alpha_o^{(i)} \\ -\cos\alpha_o^{(i)} \end{bmatrix}. \tag{4.1}$$

Vector $\mathbf{B}$ is on $x_b^{(i)} z_b^{(i)}$ plane. $\phi_c^{(i)}$ is the blade angle. The unit vector $\mathbf{U}_B$ along $\mathbf{B}$ is

$$\mathbf{U}_B = \begin{bmatrix} -\sin\phi_c^{(i)} \\ 0 \\ -\cos\phi_c^{(i)} \end{bmatrix}. \tag{4.2}$$

Plane Ω_1 is perpendicular to vector $\mathbf{B}$, and pass through origin $o_b^{(i)}$. Vector $\mathbf{C}$ is at the intersection of $x_b^{(i)} z_b^{(i)}$ plane and plane Ω_1. The unit vector $\mathbf{U}_C$ along $\mathbf{C}$ is

$$\mathbf{U}_C = \begin{bmatrix} \cos\phi_c^{(i)} \\ 0 \\ -\sin\phi_c^{(i)} \end{bmatrix}. \tag{4.3}$$

Vector $\mathbf{D}$ is on plane Ω_1, and form angle $\alpha_f^{(i)}$ with $\mathbf{C}$. The unit vector $\mathbf{U}_D$ along $\mathbf{D}$ is

$$\mathbf{U}_D = \begin{bmatrix} \cos\phi_c^{(i)} \cdot \cos\alpha_f^{(i)} \\ \sin\alpha_f^{(i)} \\ -\sin\phi_c^{(i)} \cdot \cos\alpha_f^{(i)} \end{bmatrix}. \tag{4.4}$$

Rake plane Ω_2 is determined by vectors $\mathbf{A}$ and $\mathbf{D}$. Vector $\mathbf{E}$ is normal to Ω_2, and passes through origin $o_b^{(i)}$. The vector $\mathbf{E}$ is

$$\begin{aligned} \mathbf{E} &= \mathbf{U}_A \times \mathbf{U}_D \\ &= \begin{bmatrix} \cos\alpha_o^{(i)} \cdot \sin\alpha_f^{(i)} - \sin\alpha_o^{(i)} \cdot \sin\phi_c^{(i)} \cdot \cos\alpha_f^{(i)} \\ -\cos\alpha_o^{(i)} \cdot \cos\phi_c^{(i)} \cdot \cos\alpha_f^{(i)} \\ -\sin\alpha_o^{(i)} \cdot \cos\phi_c^{(i)} \cdot \cos\alpha_f^{(i)} \end{bmatrix}. \end{aligned} \tag{4.5}$$

Vector $\mathbf{F}$ is on $y_b^{(i)} z_b^{(i)}$ plane, and forms end relief angle $\gamma_o^{(i)}$ with axis $y_b^{(i)}$ (see Fig. 4.4). The unit vector $\mathbf{U}_F$ along the Vector $\mathbf{F}$ is

$$\mathbf{U}_F = \begin{bmatrix} 0 \\ \cos\gamma_o^{(i)} \\ -\sin\gamma_o^{(i)} \end{bmatrix}. \tag{4.6}$$

Vector **G** is on $y_b^{(i)} z_b^{(i)}$ plane, and perpendicular to **F**. The unit vector $\mathbf{U}_G$ along the **G** is

$$\mathbf{U}_G = \begin{bmatrix} 0 \\ -\sin\gamma_o^{(i)} \\ -\cos\gamma_o^{(i)} \end{bmatrix}. \tag{4.7}$$

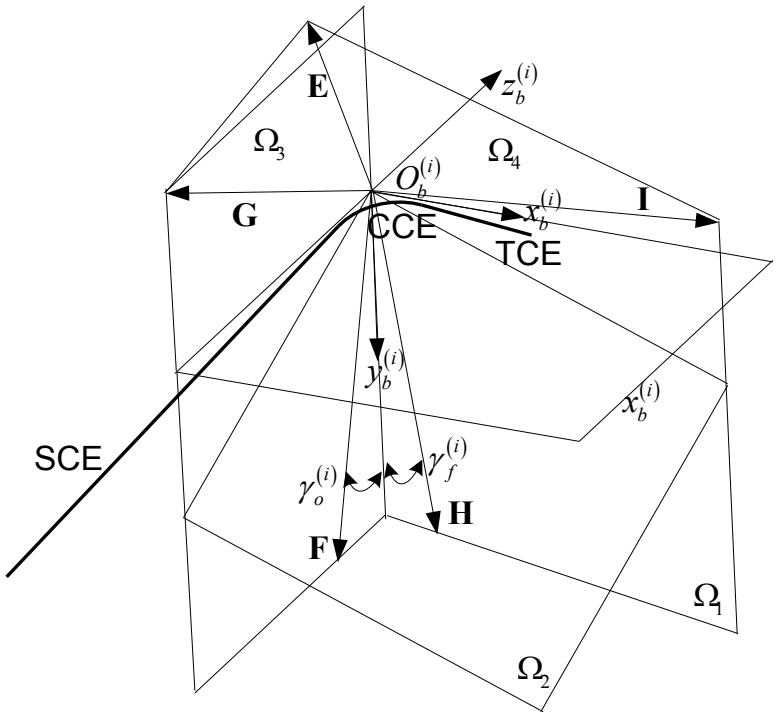

Figure 4.4 Top cutting edge and side cutting edge of inner blade.

The vectors **E** and **G** will form the plane Ω_3. The top cutting edge $\mathbf{TCE}^{(i)}$ is perpendicular to Ω_3, and may be expressed as

$$\begin{aligned} \mathbf{TCE}^{(i)} &= \mathbf{E} \times \mathbf{U}_G \\ &= \begin{bmatrix} \cos\alpha_o^{(i)} \cdot \cos\phi_c^{(i)} \cdot \cos\alpha_f^{(i)} \cdot \cos\gamma_o^{(i)} - \sin\alpha_o^{(i)} \cdot \cos\phi_c^{(i)} \cdot \cos\alpha_f^{(i)} \cdot \sin\gamma_o^{(i)} \\ \cos\alpha_o^{(i)} \cdot \sin\alpha_f^{(i)} \cdot \cos\gamma_o^{(i)} - \sin\alpha_o^{(i)} \cdot \sin\phi_c^{(i)} \cdot \cos\alpha_f^{(i)} \cdot \cos\gamma_o^{(i)} \\ \sin\alpha_o^{(i)} \cdot \sin\phi_c^{(i)} \cdot \cos\alpha_f^{(i)} \cdot \sin\gamma_o^{(i)} - \cos\alpha_o^{(i)} \cdot \sin\alpha_f^{(i)} \cdot \sin\gamma_o^{(i)} \end{bmatrix}. \end{aligned} \tag{4.8}$$

Vector $\mathbf{H}$ is on plane Ω_1, and forms side relief angle $\gamma_f^{(i)}$ with axis $y_b^{(i)}$. The unit vector $\mathbf{U}_H$ along the Vector $\mathbf{H}$ is

$$\mathbf{U}_H = \begin{bmatrix} \cos\phi_c^{(i)} \cdot \sin\gamma_f^{(i)} \\ \cos\gamma_f^{(i)} \\ -\sin\phi_c^{(i)} \cdot \sin\gamma_f^{(i)} \end{bmatrix}. \tag{4.9}$$

Vector $\mathbf{I}$ is on plane Ω_1, and perpendicular to $\mathbf{H}$. The unit vector $\mathbf{U}_I$ along the Vector $\mathbf{I}$ is

$$\mathbf{U}_I = \begin{bmatrix} \cos\phi_c^{(i)} \cdot \cos\gamma_f^{(i)} \\ -\sin\gamma_f^{(i)} \\ -\sin\phi_c^{(i)} \cdot \cos\gamma_f^{(i)} \end{bmatrix}. \tag{4.10}$$

The vector $\mathbf{E}$ and vector $\mathbf{I}$ will form the plane Ω_4. The side cutting edge $\mathbf{SCE}^{(i)}$ is perpendicular to Ω_4, and can be expressed as

$$\begin{aligned} \mathbf{SCE}^{(i)} &= \mathbf{I} \times \mathbf{E} \\ &= \begin{bmatrix} \sin\gamma_f^{(i)} \cdot \sin\alpha_o^{(i)} \cdot \cos\phi_c^{(i)} \cdot \cos\alpha_f^{(i)} - \sin\phi_c^{(i)} \cdot \cos\phi_c^{(i)} \cdot \cos\gamma_f^{(i)} \cdot \cos\alpha_o^{(i)} \cdot \cos\alpha_f^{(i)} \\ \left(\cos\phi_c^{(i)}\right)^2 \cdot \cos\gamma_f^{(i)} \cdot \sin\alpha_o^{(i)} \cdot \cos\alpha_f^{(i)} - \sin\phi_c^{(i)} \cdot \cos\gamma_f^{(i)} \cdot \cos\alpha_o^{(i)} \cdot \sin\alpha_f^{(i)} + \left(\sin\phi_c^{(i)}\right)^2 \cdot \cos\gamma_f^{(i)} \cdot \sin\alpha_o^{(i)} \cdot \cos\alpha_f^{(i)} \\ \sin\gamma_f^{(i)} \cdot \cos\alpha_o^{(i)} \cdot \sin\alpha_f^{(i)} - \sin\gamma_f^{(i)} \cdot \sin\alpha_o^{(i)} \cdot \sin\phi_c^{(i)} \cdot \cos\alpha_f^{(i)} - \left(\cos\phi_c^{(i)}\right)^2 \cdot \cos\gamma_f^{(i)} \cdot \cos\alpha_o^{(i)} \cdot \cos\alpha_f^{(i)} \end{bmatrix}. \end{aligned} \tag{4.11}$$

The circular cutting edge $\mathbf{CCE}^{(i)}$ is an arc on rake plane Ω_1. It is tangent to $\mathbf{TCE}^{(i)}$ and $\mathbf{SCE}^{(i)}$ (Fig. 4.5). Suppose r is its radius. The Point $o_r^{(i)}$ is the center of the arc. $\mathbf{TCE}^{(i)}$ is tangent to $\mathbf{CCE}^{(i)}$ at point J.

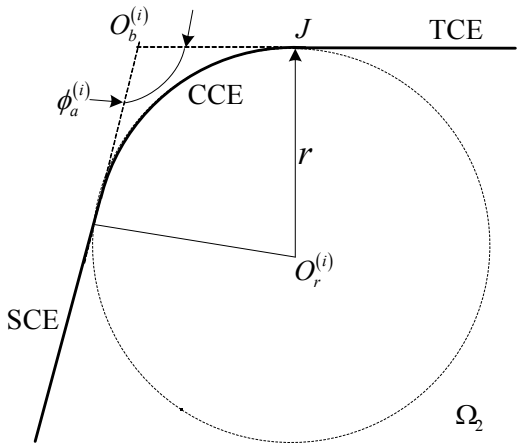

Figure 4.5 Circular cutting edge of inner blade.

The vector $\overrightarrow{O_b^{(i)}J}$ can be expressed as

$$\overrightarrow{O_b^{(i)}J} = r \cdot \cot\frac{\phi_a^{(i)}}{2} \cdot \mathbf{U}_{\mathrm{TCE}}^{(i)}. \tag{4.12}$$

Here $\mathbf{U}_{\mathrm{TCE}}^{(i)}$ is the unit vector of $\mathbf{TCE}^{(i)}$, and the vector $\overrightarrow{O_b^{(i)}O_r^{(i)}}$ can be written as

$$\overrightarrow{O_b^{(i)}O_r^{(i)}} = \overrightarrow{O_b^{(i)}J} + \overrightarrow{JO_r^{(i)}}. \tag{4.13}$$

Since $\mathbf{E}$ and $\mathbf{TCE}^{(i)}$ are both perpendicular to $\overrightarrow{JO_r^{(i)}}$, the vector $\overrightarrow{JO_r^{(i)}}$ can be represented as

$$\overrightarrow{JO_r^{(i)}} = r \cdot \left(\mathbf{U}_{\mathrm{TCE}}^{(i)} \times \mathbf{U}_E\right), \tag{4.14}$$

and $\mathbf{U}_E$ is the unit norm vector on rake plane. Assume $\phi_a^{(i)}$ is the angle between $\mathbf{SCE}^{(i)}$ and $\mathbf{TCE}^{(i)}$. Since the vector $\mathbf{SCE}^{(i)}$ and $\mathbf{TCE}^{(i)}$ are known, the angle $\phi_a^{(i)}$ can be represented as

$$\phi_a^{(i)} = \arccos\left(\mathbf{U}_{\mathrm{TCE}}^{(i)} \cdot \mathbf{U}_{\mathrm{SCE}}^{(i)}\right), \tag{4.15}$$

and $\mathbf{U}_{\mathrm{SCE}}^{(i)}$ is the unit vector of $\mathbf{SCE}^{(i)}$. The circular cutting edge $\mathbf{CCE}^{(i)}$ can be obtained by translating and rotating an arc from $x_b^{(i)} z_b^{(i)}$ plane to the rake plane Ω_2 (see Fig. 4.6).

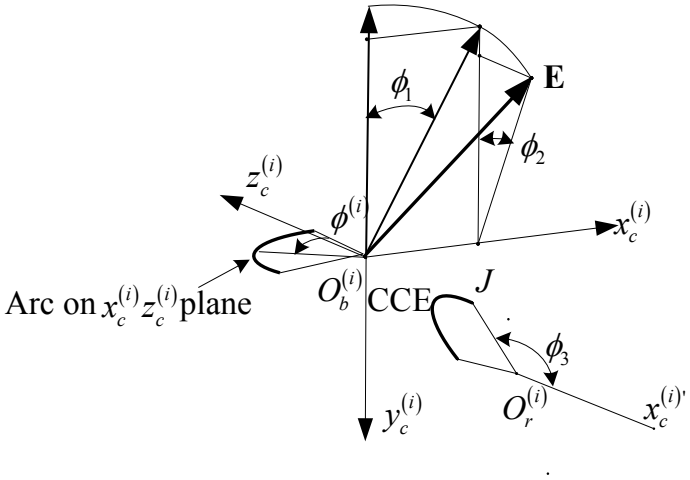

Figure 4.6 Transformation of CCE from normal plane to rake plane.

The $\mathbf{CCE}^{(i)}$ can be represented as

$$\begin{bmatrix} L_{\mathbf{CCE}}^{(i)}\left(\phi^{(i)}\right) \\ 1 \end{bmatrix} = M_{CCE}^{(i)} \cdot \begin{bmatrix} r \cdot \cos\phi^{(i)} \\ 0 \\ r \cdot \sin\phi^{(i)} \\ 1 \end{bmatrix} \quad \left(\phi_3 \le \phi^{(i)} \le \phi_3 + \phi_a^{(i)}\right), \tag{4.16}$$

with the transformation matrices can be represented as

$$M_{CCE}^{(i)} = Trans^{(i)}\left(z, Z_{O_r^{(i)}}\right) \cdot Trans^{(i)}\left(y, Y_{O_r^{(i)}}\right) \cdot Trans^{(i)}\left(x, X_{O_r^{(i)}}\right) \cdot Rot^{(i)}\left(x, \phi_2\right) \cdot Rot^{(i)}\left(z, \phi_1\right)$$

$$= \begin{bmatrix} \cos\phi_1 & -\sin\phi_1 & 0 & X_{O_r^{(i)}} \\ \cos\phi_2 \cdot \sin\phi_1 & \cos\phi_2 \cdot \cos\phi_1 & -\sin\phi_2 & Y_{O_r^{(i)}} \\ \sin\phi_2 \cdot \sin\phi_1 & \sin\phi_2 \cdot \cos\phi_1 & \cos\phi_2 & Z_{O_r^{(i)}} \\ 0 & 0 & 0 & 1 \end{bmatrix}.$$

This equation can be explained as at the beginning an arc is defined on $x_b^{(i)}z_b^{(i)}$ plane, and then rotated about $z_b^{(i)}$ axis with angle ϕ_1, and then rotated about $z_b^{(i)}$ axis with angle ϕ_2. Up to now the arc is transformed from $x_b^{(i)}z_b^{(i)}$ plane to rake plane, and the last step is to translate it from $O_b^{(i)}$ to $O_r^{(i)}$. The coordinates of **E** can be written as $\mathbf{E} = \begin{bmatrix} X_E & Y_E & Z_E \end{bmatrix}^{\mathrm{T}}$, the rotation angle ϕ_1 and ϕ_2 are calculated as

$$\phi_1 = \arcsin\left(\frac{X_E}{\sqrt{X_E{}^2 + Y_E{}^2 + Z_E{}^2}} \right), \tag{4.17}$$

and

$$\phi_2 = \arctan\left(\frac{Z_E}{Y_E} \right) = \alpha_o^{(i)}. \tag{4.18}$$

To decide the limit of arc parameter $\phi^{(i)}$, the same transformation matrices are applied on $x_b^{(i)}$ axis. We can get the new vector $x_b^{(i)'}$ after transformation

$$\begin{bmatrix} x_b^{(i)'} \\ 0 \end{bmatrix} = M_{CCE}^{(i)} \cdot \begin{bmatrix} x_b^{(i)} \\ 0 \end{bmatrix}. \tag{4.19}$$

ϕ_3 is the angle between vector $x_b^{(i)'}$ and $\overrightarrow{JO_r'}$, which can be expressed as

$$\phi_3 = \arccos\left(\frac{x_b^{(i)'} \cdot \overrightarrow{\quad\quad}}{\left| x_b^{(i)'} \right| \cdot \left| \overrightarrow{JO_r'} \right|} \right). \tag{4.20}$$

Finally the $\mathbf{CCE}^{(i)}$ can be represented as

$$L_{\mathbf{CCE}}^{(i)}\left(\phi^{(i)}\right)=\begin{bmatrix} r\cdot\cos\phi_1\cdot\cos\phi^{(i)}+X_{O_r^{(i)}} \\ r\cdot\cos\phi_2\cdot\sin\phi_1\cdot\cos\phi^{(i)}-r\cdot\sin\phi_2\cdot\sin\phi^{(i)}+Y_{O_r^{(i)}} \\ r\cdot\sin\phi_2\cdot\sin\phi_1\cdot\cos\phi^{(i)}+r\cdot\cos\phi_2\cdot\sin\phi^{(i)}+Z_{O_r^{(i)}} \end{bmatrix} \quad \left(\phi_3\le\phi^{(i)}\le\phi_3+\phi_a^{(i)}\right). \tag{4.21}$$

Assume the point width is p_w and the depth of blade is d_b (see Fig. 4.7).

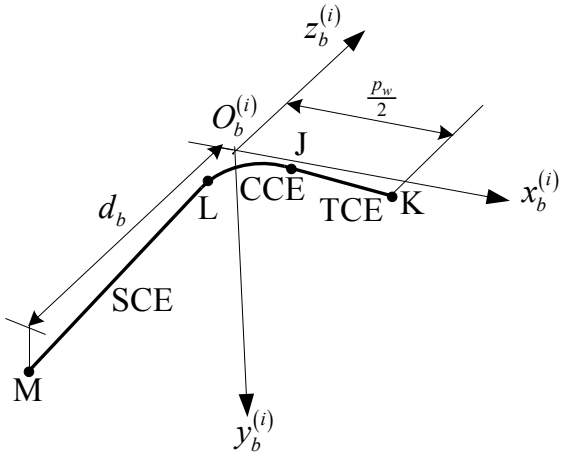

Figure 4.7 Top cutting edge and side cutting edge of inner blade.

The parametric equation of the TCE can be expressed as

$$\mathbf{L}_{TCE}^{(i)}\left(u_1\right)=\left(1-u_1\right)\cdot J+u_1\cdot K \qquad \left(0\le u_1\le 1\right), \tag{4.22}$$

with $J=r\cdot\cot\frac{\theta_i}{2}\cdot\mathbf{U}_{\mathrm{TCE}}^{(i)}$ and $K=\frac{p_w}{2}\cdot\mathbf{U}_{\mathrm{TCE}}^{(i)}$.

The parametric equation of the SCE can be expressed as

$$\mathbf{L}_{SCE}^{(i)}\left(u_2\right)=\left(1-u_2\right)\cdot L+u_2\cdot M \qquad \left(0\le u_2\le 1\right), \tag{4.23}$$

with $L=r\cdot\cot\frac{\theta_i}{2}\cdot\mathbf{U}_{\mathrm{SCE}}^{(i)}$ and $M=\frac{d_b}{Z_{\mathbf{U}_{\mathrm{SCE}}^{(i)}}}\cdot\mathbf{U}_{\mathrm{SCE}}^{(i)}$.

4.4 Outer Blade in Blade Coordinate System

The outer blade is similar to the inner blade, and can be defined by the same parameters (see Fig. 4.8), but the outer blade may have different parameter values, such as blade angle, rake angles and relief angles.

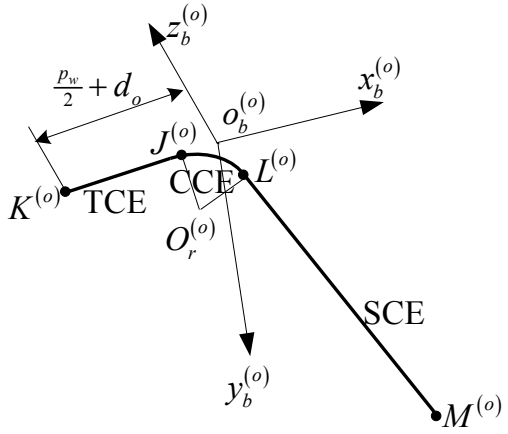

Figure 4.8 Parametric model of the outer blade.

The circular cutting edge can be represented as

$$\begin{bmatrix} \mathbf{L}_{\mathrm{CCE}}^{(o)}\left(\phi^{(o)}\right) \\ 1 \end{bmatrix} = M_{CCE}^{(o)} \cdot \begin{bmatrix} r^{(o)} \cdot \cos\phi^{(o)} \\ 0 \\ r^{(o)} \cdot \sin\phi^{(o)} \\ 1 \end{bmatrix} \quad \left(\phi_3^{(o)} \le \phi^{(o)} \le \phi_3^{(o)} - \phi_a^{(o)}\right), \tag{4.24}$$

With

$$M_{CCE}^{(o)} = Trans^{(o)}\left(z, Z_{O_r^{(o)}}\right) \cdot Trans^{(o)}\left(y, Y_{O_r^{(o)}}\right) \cdot Trans^{(o)}\left(x, X_{O_r^{(o)}}\right) \cdot Rot^{(o)}\left(x, \phi_2^{(o)}\right) \cdot Rot^{(o)}\left(z, \phi_1^{(o)}\right)$$

$$= \begin{bmatrix} \cos\phi_1^{(o)} & -\sin\phi_1^{(o)} & 0 & X_{O_r^{(o)}} \\ \cos\phi_2^{(o)} \cdot \sin\phi_1^{(o)} & \cos\phi_2^{(o)} \cdot \cos\phi_1^{(o)} & -\sin\phi_2^{(o)} & Y_{O_r^{(o)}} \\ \sin\phi_2^{(o)} \cdot \sin\phi_1^{(o)} & \sin\phi_2^{(o)} \cdot \cos\phi_1^{(o)} & \cos\phi_2^{(o)} & Z_{O_r^{(o)}} \\ 0 & 0 & 0 & 1 \end{bmatrix}$$

and $\phi_1^{(o)} = \arcsin\left(\frac{X_{E^{(o)}}}{\sqrt{X_{E^{(o)}}{}^2 + Y_{E^{(o)}}{}^2 + Z_{E^{(o)}}{}^2}}\right)$ and $\phi_2^{(o)} = \arctan\left(\frac{Z_{E^{(o)}}}{Y_{E^{(o)}}}\right) = \alpha_o^{(o)}$.

$E^{(o)}$ is the normal vector to the rake plane, which can be represented as

$$\mathbf{E}^{(o)} = \begin{bmatrix} \sin\alpha_o^{(o)} \cdot \sin\phi_c^{(o)} \cdot \cos\alpha_f^{(o)} - \cos\alpha_o^{(o)} \cdot \sin\alpha_f^{(o)} \\ -\cos\alpha_o^{(o)} \cdot \cos\phi_c^{(o)} \cdot \cos\alpha_f^{(o)} \\ -\sin\alpha_o^{(o)} \cdot \cos\phi_c^{(o)} \cdot \cos\alpha_f^{(o)} \end{bmatrix}. \tag{4.25}$$

The vector $x_b^{(o)'}$ is $x_b^{(o)}$ after transformation, which can be represented as

$$\begin{bmatrix} x_b^{(o)'} \\ 0 \end{bmatrix} = M_{CCE}^{(o)} \cdot \begin{bmatrix} x_b^{(o)} \\ 0 \end{bmatrix}. \tag{4.26}$$

With $x_b^{(o)'}$ we can derive $\phi_3^{(o)}$ as

$$\phi_3^{(o)} = \arccos\left(\frac{x_b^{(o)'} \cdot \overrightarrow{\quad\quad}}{\left|x_b^{(o)'}\right| \cdot \left|\overrightarrow{JO_r}\right|}\right). \tag{4.27}$$

Thus, the limits of $\phi^{(o)}$ are $\phi_3^{(o)} \le \phi^{(o)} \le \phi_3^{(o)} + \phi_a^{(o)}$. Here, $\phi_a^{(o)}$ is the angle between SCE and TCE, and it can be calculated from

$$\phi_a^{(o)} = \arccos\left(\mathbf{U}_{\mathrm{TCE}}^{(o)} \cdot \mathbf{U}_{\mathrm{SCE}}^{(o)}\right). \tag{4.28}$$

$\mathbf{U}_{\mathrm{TCE}}^{(o)}$ and $\mathbf{U}_{\mathrm{SCE}}^{(o)}$ are respectively the unit vector of top cutting edge and side cutting edge. $\mathbf{TCE}^{(o)}$ and $\mathbf{SCE}^{(o)}$ can be represented as

$$\mathbf{TCE}^{(o)} = \begin{bmatrix} \sin\alpha_o^{(o)} \cdot \cos\phi_c^{(o)} \cdot \cos\alpha_f^{(o)} \cdot \sin\gamma_o^{(o)} - \cos\alpha_o^{(o)} \cdot \cos\phi_c^{(o)} \cdot \cos\alpha_f^{(o)} \cdot \cos\gamma_o^{(o)} \\ \cos\alpha_o^{(o)} \cdot \sin\alpha_f^{(o)} \cdot \cos\gamma_o^{(o)} - \sin\alpha_o^{(o)} \cdot \sin\phi_c^{(o)} \cdot \cos\alpha_f^{(o)} \cdot \cos\gamma_o^{(o)} \\ \sin\alpha_o^{(o)} \cdot \sin\phi_c^{(o)} \cdot \cos\alpha_f^{(o)} \cdot \sin\gamma_o^{(o)} - \cos\alpha_o^{(o)} \cdot \sin\alpha_f^{(o)} \cdot \sin\gamma_o^{(o)} \end{bmatrix}, \quad (4.29)$$

and

$$\mathbf{SCE}^{(o)} = \begin{bmatrix} \sin\phi_c^{(o)} \cdot \cos\phi_c^{(o)} \cdot \cos\gamma_f^{(o)} \cdot \cos\alpha_o^{(o)} \cdot \cos\alpha_f^{(o)} - \sin\gamma_f^{(o)} \cdot \sin\alpha_o^{(o)} \cdot \cos\phi_c^{(o)} \cdot \cos\alpha_f^{(o)} \\ \left(\cos\phi_c^{(o)}\right)^2 \cdot \cos\gamma_f^{(o)} \cdot \sin\alpha_o^{(o)} \cdot \cos\alpha_f^{(o)} - \sin\phi_c^{(o)} \cdot \cos\gamma_f^{(o)} \cdot \cos\alpha_o^{(o)} \cdot \sin\alpha_f^{(o)} + \left(\sin\phi_c^{(o)}\right)^2 \cdot \cos\gamma_f^{(o)} \cdot \sin\alpha_o^{(o)} \cdot \cos\alpha_f^{(o)} \\ \sin\gamma_f^{(o)} \cdot \cos\alpha_o^{(o)} \cdot \sin\alpha_f^{(o)} - \sin\gamma_f^{(o)} \cdot \sin\alpha_o^{(o)} \cdot \sin\phi_c^{(o)} \cdot \cos\alpha_f^{(o)} - \left(\cos\phi_c^{(o)}\right)^2 \cdot \cos\gamma_f^{(o)} \cdot \cos\alpha_o^{(o)} \cdot \cos\alpha_f^{(o)} \end{bmatrix}$$
,(4.30)

The parametric equation of TCE can be expressed as

$$\mathbf{L}_{TCE}^{(o)} = \left(1-u_3\right) \cdot J^{(o)} + u_3 \cdot K^{(o)} \qquad \left(0 \le u_3 \le 1\right), \quad (4.31)$$

with $\mathbf{J}^{(o)} = r^{(o)} \cdot \cot\dfrac{\theta_i^{(o)}}{2} \cdot \mathbf{U}_{\mathrm{TCE}}^{(o)}$ and $\mathbf{K}^{(o)} = \left(\dfrac{p_w}{2} + d_o\right) \cdot \mathbf{U}_{\mathrm{TCE}}^{(o)}$.

d_o is the overlap between inner and outer blades. The parametric equation of TCE is

$$\mathbf{L}_{SCE}^{(o)} = \left(1-u_4\right) \cdot L^{(o)} + u_4 \cdot M^{(o)} \qquad \left(0 \le u_4 \le 1\right), \quad (4.32)$$

with $\mathbf{L}^{(o)} = r^{(o)} \cdot \cot\dfrac{\theta_i^{(o)}}{2} \cdot \mathbf{U}_{\mathrm{SCE}}^{(o)}$ and $\mathbf{M}^{(o)} = \dfrac{d_b}{Z_{\mathbf{U}_{\mathrm{SCE}}^{(o)}}} \cdot \mathbf{U}_{\mathrm{SCE}}^{(o)}$.

4.5 Cutting edges in cutter coordinate system

The inner and outer blades are mounted on the cutter plates alternatively (Fig. 4.9). The axes z_c, $z_b^{(i)}$ and $z_b^{(o)}$ are parallel to each other. Axis x_c is coincide with $x_b^{(i)}$, and

forms angle ϕ_p with $x_b^{(o)}$. The angle ϕ_p can be calculated from the number of the blades, and $\phi_p = \dfrac{2 \cdot \pi}{n_b}$.

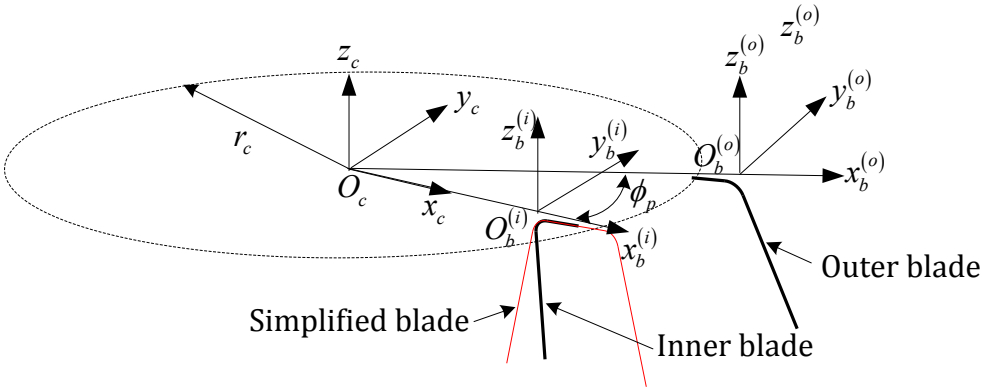

Figure 4.9 Blades in cutter coordinate system.

r_c is the mean cutter radius. The cutting edges of inner blade can be represented in cutter coordinate system S_c as

$$\begin{cases} \begin{bmatrix} \mathbf{P}_{\mathrm{CCE}}^{(i)}\left(\phi^{(i)}\right) \\ 1 \end{bmatrix} = M_{cb}^{(i)} \cdot \begin{bmatrix} \mathbf{L}_{\mathrm{CCE}}^{(i)}\left(\phi^{(i)}\right) \\ 1 \end{bmatrix} & \left(\phi_3 \le \phi^{(i)} \le \phi_3 + \phi_a^{(i)}\right) \\ \begin{bmatrix} \mathbf{P}_{\mathrm{TCE}}^{(i)}\left(u_1\right) \\ 1 \end{bmatrix} = M_{cb}^{(i)} \cdot \begin{bmatrix} \mathbf{L}_{\mathrm{TCE}}^{(i)}\left(\phi^{(i)}\right) \\ 1 \end{bmatrix} & \left(0 \le u_1 \le 1\right) \\ \begin{bmatrix} \mathbf{P}_{\mathrm{SCE}}^{(i)}\left(u_2\right) \\ 1 \end{bmatrix} = M_{cb}^{(i)} \cdot \begin{bmatrix} \mathbf{L}_{\mathrm{SCE}}^{(i)}\left(u_2\right) \\ 1 \end{bmatrix} & \left(0 \le u_2 \le 1\right) \end{cases}, \tag{4.33}$$

with the transformation matrix

$$M_{cb}^{(i)} = \begin{bmatrix} 1 & 0 & 0 & \sqrt{r_c^{\,2} - Y_K^{\,2}} - X_K \\ 0 & 1 & 0 & 0 \\ 0 & 0 & 1 & 0 \\ 0 & 0 & 0 & 1 \end{bmatrix}.$$

The cutting edges of outer blade can be represented in cutter coordinate system S_c as

$$\begin{cases} \begin{bmatrix} \mathbf{P}_{\mathrm{CCE}}^{(o)}\left(\phi^{(o)}\right) \\ 1 \end{bmatrix} = M_{cb}^{(o)} \cdot \begin{bmatrix} \mathbf{L}_{\mathrm{CCE}}^{(o)}\left(\phi^{(o)}\right) \\ 1 \end{bmatrix} & \left(\phi_3 \le \phi^{(o)} \le \phi_3 + \phi_a^{(o)}\right) \\ \begin{bmatrix} \mathbf{P}_{\mathrm{TCE}}^{(o)}\left(u_3\right) \\ 1 \end{bmatrix} = M_{cb}^{(o)} \cdot \begin{bmatrix} \mathbf{L}_{\mathrm{TCE}}^{(o)}\left(u_3\right) \\ 1 \end{bmatrix} & \left(0 \le u_3 \le 1\right) \\ \begin{bmatrix} \mathbf{P}_{\mathrm{SCE}}^{(o)}\left(u_4\right) \\ 1 \end{bmatrix} = M_{cb}^{(o)} \cdot \begin{bmatrix} \mathbf{L}_{\mathrm{SCE}}^{(o)}\left(u_4\right) \\ 1 \end{bmatrix} & \left(0 \le u_4 \le 1\right) \end{cases}, \tag{4.34}$$

with the transformation matrix

$$M_{cb}^{(o)} = \begin{bmatrix} \cos\phi_p & -\sin\phi_p & 0 & \sqrt{r_c^{\,2} - Y_{K^{(o)}}^{\,2}} - X_{K^{(o)}} \\ \sin\phi_p & \cos\phi_p & 0 & 0 \\ 0 & 0 & 1 & 0 \\ 0 & 0 & 0 & 1 \end{bmatrix}.$$

4.6 Cross Section of Tool Surface on $x_c z_c$ Plane

The tool surface is generated by blades rotating about the cutter axis z_c. Since the simplified blades are defined on the normal plane, which is $x_c z_c$ in S_c, to compare the genuine tool surface to the simplified tool surface, the cross section of genuine tool surfaces on $x_c z_c$ plane is taken. By calculating the distance between this cross section and simplified blade profile, we can evaluate the geometric error of the simplified model.

4.6.1 Cross Section of Tool Surface Revolved by SCE on $x_c z_c$ Plane

The blade side cutting edge is a straight line on rake face, when it rotates about the z_c axis, it will produce the tool surface of side cutting edge (Fig. 4.10).

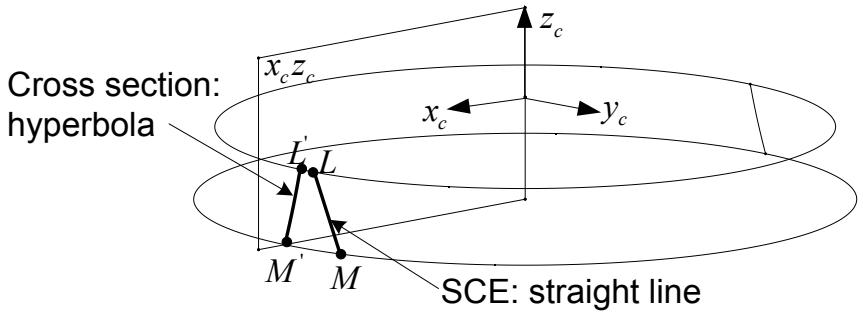

Figure 4.10 Cross section of tool surface revolved by SCE on $x_c z_c$ plane.

Points M and L are two ends of inner blade SCE, they can be represented in S_c as $\mathbf{P}_{\mathrm{SCE}}^{(i)}(1)$ and $\mathbf{P}_{\mathrm{SCE}}^{(i)}(0)$. When LM revolves about z_c, the surface can be represented as

$$S_{SCE}^{(i)}\left(u_2,\varphi^{(i)}\right)=\begin{bmatrix}\cos\varphi^{(i)}\cdot\left[X_{L_c}+u_2\cdot\left(X_{M_c}-X_{L_c}\right)\right]-\sin\varphi^{(i)}\cdot\left[Y_{L_c}+u_2\cdot\left(Y_{M_c}-Y_{L_c}\right)\right]\\ \sin\varphi^{(i)}\cdot\left[X_{L_c}+u_2\cdot\left(X_{M_c}-X_{L_c}\right)\right]+\cos\varphi^{(i)}\cdot\left[Y_{L_c}+u_2\cdot\left(Y_{M_c}-Y_{L_c}\right)\right]\\ Z_{L_c}+u_2\cdot\left(Z_{M_c}-Z_{L_c}\right)\end{bmatrix}. \quad (4.35)$$

The cross section of $S_{SCE}^{(i)}$ on $x_c z_c$ should satisfied the equation

$$\sin\varphi^{(i)}\cdot\left[X_{L_c}+u_2\cdot\left(X_{M_c}-X_{L_c}\right)\right]+\cos\varphi^{(i)}\cdot\left[Y_{L_c}+u_2\cdot\left(Y_{M_c}-Y_{L_c}\right)\right]=0, \quad (4.36)$$

so from the equation we can obtain the relation between $\varphi^{(i)}$ and u_2

$$\sin\varphi^{(i)} = -\frac{Y_{L_c} + u_2 \cdot \left(Y_{M_c} - Y_{L_c}\right)}{\sqrt{\left[X_{L_c} + u_2 \cdot \left(X_{M_c} - X_{L_c}\right)\right]^2 + \left[Y_{L_c} + u_2 \cdot \left(Y_{M_c} - Y_{L_c}\right)\right]^2}},$$

and

$$\cos\varphi^{(i)} = \frac{X_{L_c} + u_2 \cdot \left(X_{M_c} - X_{L_c}\right)}{\sqrt{\left[X_{L_c} + u_2 \cdot \left(X_{M_c} - X_{L_c}\right)\right]^2 + \left[Y_{L_c} + u_2 \cdot \left(Y_{M_c} - Y_{L_c}\right)\right]^2}}.$$

Replace $\sin\varphi^{(i)}$ and $\cos\varphi^{(i)}$ in $S_{SCE}^{(i)}$, we can get the planar curve $\mathbf{C}_{SCE}^{(i)}$ one the $x_c z_c$ plane, which can be written as

$$\mathbf{C}_{SCE}^{(i)}\left(u_2\right) = \begin{bmatrix} \sqrt{\left[X_{L_c} + u_2 \cdot \left(X_{M_c} - X_{L_c}\right)\right]^2 + \left[Y_{L_c} + u_2 \cdot \left(Y_{M_c} - Y_{L_c}\right)\right]^2} \\ Z_{L_c} + u_2 \cdot \left(Z_{M_c} - Z_{L_c}\right) \end{bmatrix}. \tag{4.37}$$

This planar curve can be written in the explicit way as

$$\frac{\left(X_{M_c} - X_{L_c}\right)^2 + \left(Y_{M_c} - Y_{L_c}\right)^2}{\left(Z_{M_c} - Z_{L_c}\right)^2} \cdot \left(z - Z_{L_c}\right)^2 + 2 \cdot \frac{X_{L_c} \cdot \left(X_{M_c} - X_{L_c}\right) + Y_{L_c} \cdot \left(Y_{M_c} - Y_{L_c}\right)}{\left(Z_{M_c} - Z_{L_c}\right)} \cdot \left(z - Z_{L_c}\right) - x^2 + {X_{L_c}}^2 + {Y_{L_c}}^2 = 0, \tag{4.38}$$

It can be simplified as a typical hyperbola equation

$$\frac{x^2}{a^2} - \frac{\left(z-c\right)^2}{b^2} = 1, \tag{4.39}$$

with the parameters

$$a=\sqrt{\left(X_{L_c}{}^2+Y_{L_c}{}^2\right)-\frac{\left[X_{L_c}\cdot\left(X_{M_c}-X_{L_c}\right)+Y_{L_c}\cdot\left(Y_{M_c}-Y_{L_c}\right)\right]^2}{\left(X_{M_c}-X_{L_c}\right)^2+\left(Y_{M_c}-Y_{L_c}\right)^2}},$$

$$b=\frac{\sqrt{\left(Z_{M_c}-Z_{L_c}\right)^2\cdot\left\{\left(X_{L_c}{}^2+Y_{L_c}{}^2\right)\cdot\left[\left(X_{M_c}-X_{L_c}\right)^2+\left(Y_{M_c}-Y_{L_c}\right)^2\right]-\left[X_{L_c}\cdot\left(X_{M_c}-X_{L_c}\right)+Y_{L_c}\cdot\left(Y_{M_c}-Y_{L_c}\right)\right]^2\right\}}}{\left[\left(X_{M_c}-X_{L_c}\right)^2+\left(Y_{M_c}-Y_{L_c}\right)^2\right]},$$

$$c=Z_{L_c}-\frac{\left(Z_{M_c}-Z_{L_c}\right)\cdot\left[X_{L_c}\cdot\left(X_{M_c}-X_{L_c}\right)+Y_{L_c}\cdot\left(Y_{M_c}-Y_{L_c}\right)\right]}{\left(X_{M_c}{}^2-X_{L_c}{}^2\right)+\left(Y_{M_c}{}^2-Y_{L_c}{}^2\right)}.$$

Fig. 4.11 shows the cross section $\mathbf{C}_{SCE}^{(i)}$ is one segment of hyperbola, which is starting from $L^{'}$ to $M^{'}$, and their coordinates can be calculated as

$$\begin{cases} L^{'}=\left[\sqrt{X_{L_c}{}^2+Y_{L_c}{}^2} \quad Z_{L_c}\right]^T \\ M^{'}=\left[\sqrt{X_{M_c}{}^2+Y_{M_c}{}^2} \quad Z_{M_c}\right]^T \end{cases}. \tag{4.40}$$

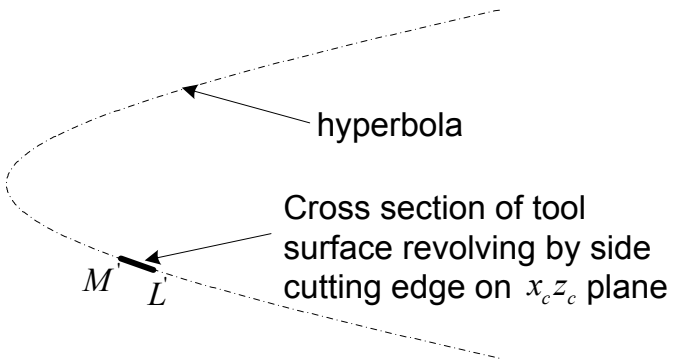

Figure 4.11 Hyperbola curve.

By using the same procedure, we can derive cross section of tooth surface generated by outer blade $\mathbf{C}_{SCE}^{(o)}$, which can be written as

$$\mathbf{C}_{SCE}^{(o)}\left(u_2\right)=\begin{bmatrix}\sqrt{\left[X_{L_c^{(o)}}+u_4\cdot\left(X_{M_c^{(o)}}-X_{L_c^{(o)}}\right)\right]^2+\left[Y_{L_c^{(o)}}+u_4\cdot\left(Y_{M_c^{(o)}}-Y_{L_c^{(o)}}\right)\right]^2}\\ Z_{L_c^{(o)}}+u_4\cdot\left(Z_{M_c^{(o)}}-Z_{L_c^{(o)}}\right)\end{bmatrix}. \quad (4.41)$$

This result shows the cross section of tool surface revolving by SCE on $x_c z_c$ plane is a hyperbola. It is totally different with the simplified blade, which simply treated SEC as a straight line on $x_c z_c$ plane. Since the SCE is responsible for the generation of tooth flank, this geometric error caused from simplification finally affects the tooth mating between gear and pinion.

4.6.2 Cross Section of Tool Surface Revolved by CCE on $x_c z_c$ Plane

The circular cutting CCE is an arc locating on rake plane. The parametric equation of inner blade CCE in Eq. 4.34 can be also written as

$$\mathbf{P}_{\mathrm{CCE}}^{(i)}\left(\phi^{(i)}\right)=\begin{bmatrix}r\cdot\cos\phi_1\cdot\cos\phi^{(i)}+X_{O_r^{(i)}}+\sqrt{r_c^{\,2}-Y_K^{\,2}}-X_K^{\,2}\\ r\cdot\cos\phi_2\cdot\sin\phi_1\cdot\cos\phi^{(i)}-r\cdot\sin\phi_2\cdot\sin\phi^{(i)}+Y_{O_r^{(i)}}\\ r\cdot\sin\phi_2\cdot\sin\phi_1\cdot\cos\phi^{(i)}+r\cdot\cos\phi_2\cdot\sin\phi^{(i)}+Z_{O_r^{(i)}}\end{bmatrix}\quad\left(\phi_3\le\phi^{(i)}\le\phi_3+\phi_a^{(i)}\right)$$

. (4.42)

When it rotates about z_c, the revolving surface can be represented as

$$S_{\mathrm{CCE}}^{(i)}\left(\phi^{(i)},\varphi^{(i)}\right)=M_{rc}^{(i)}\left(\varphi^{(i)}\right)\cdot\mathbf{P}_{\mathrm{CCE}}^{(i)}\left(\phi^{(i)}\right)\quad\left(\phi_3\le\phi^{(i)}\le\phi_3+\phi_a^{(i)},0\le\varphi^{(i)}\le2\cdot\pi\right), (4.43)$$

with

$$M_{rc}^{(i)}\left(\varphi^{(i)}\right)=\begin{bmatrix}\cos\varphi^{(i)} & -\sin\varphi^{(i)} & 0 & 0\\ \sin\varphi^{(i)} & \cos\varphi^{(i)} & 0 & 0\\ 0 & 0 & 1 & 0\\ 0 & 0 & 0 & 1\end{bmatrix}.$$

The y-coordinate of cross section of $S_{\mathrm{CCE}}^{(i)}$ on $x_c z_c$ plane should equal to zero. Based on this rule we can derive the equation

$$\begin{cases} a_1=\sin\varphi^{(i)}=\dfrac{-Y_{\mathbf{P}_{\mathrm{CCE}}^{(i)}}}{\sqrt{X_{\mathbf{P}_{\mathrm{CCE}}^{(i)}}{}^2+Y_{\mathbf{P}_{\mathrm{CCE}}^{(i)}}{}^2}} \\ a_2=\cos\varphi^{(i)}=\dfrac{X_{\mathbf{P}_{\mathrm{CCE}}^{(i)}}}{\sqrt{X_{\mathbf{P}_{\mathrm{CCE}}^{(i)}}{}^2+Y_{\mathbf{P}_{\mathrm{CCE}}^{(i)}}{}^2}} \end{cases}. \tag{4.44}$$

Combining the above equations, we can get the plane curve on $x_c z_c$ plane

$$S_{\mathrm{CCE}}^{(i)}\left(\phi^{(i)}\right)=\begin{bmatrix} a_2\cdot\left(r\cdot\cos\phi_1\cdot\cos\phi^{(i)}+X_{O_r^{(i)}}+\sqrt{r_c^2-Y_K{}^2}-X_K{}^2\right)-a_1\cdot\left(r\cdot\cos\phi_2\cdot\sin\phi_1\cdot\cos\phi^{(i)}-r\cdot\sin\phi_2\cdot\sin\phi^{(i)}+Y_{O_r^{(i)}}\right) \\ r\cdot\sin\phi_2\cdot\sin\phi_1\cdot\cos\phi^{(i)}+r\cdot\cos\phi_2\cdot\sin\phi^{(i)}+Z_{O_r^{(i)}} \end{bmatrix}.$$

(4.45)

The parametric equation shows the cross section is a complicated curve. Using the same procedure, we can derive the cross section for the tooth surface generated by outer blade, which can be written as

$$S_{\mathrm{CCE}}^{(o)}\left(\phi^{(o)}\right)=\begin{bmatrix} a_4\cdot\left(r\cdot\cos\phi_1^{(o)}\cdot\cos\phi^{(o)}+X_{O_r^{(o)}}+\sqrt{r_c^2-Y_{K^{(o)}}{}^2}-X_{K^{(o)}}{}^2\right)-a_3\cdot\left(r\cdot\cos\phi_2^{(o)}\cdot\sin\phi_1^{(o)}\cdot\cos\phi^{(o)}-r\cdot\sin\phi_2^{(o)}\cdot\sin\phi^{(o)}+Y_{O_r^{(o)}}\right) \\ r\cdot\sin\phi_2^{(o)}\cdot\sin\phi_1^{(o)}\cdot\cos\phi^{(o)}+r\cdot\cos\phi_2^{(o)}\cdot\sin\phi^{(o)}+Z_{O_r^{(o)}} \end{bmatrix}$$

,(4.46)

with

$$\begin{cases} a_3 = \sin\varphi^{(o)} = \dfrac{-Y_{\mathbf{P}_{\mathrm{CCE}}^{(o)}}}{\sqrt{X_{\mathbf{P}_{\mathrm{CCE}}^{(o)}}{}^2 + Y_{\mathbf{P}_{\mathrm{CCE}}^{(o)}}{}^2}} \\ a_4 = \cos\varphi^{(o)} = \dfrac{X_{\mathbf{P}_{\mathrm{CCE}}^{(o)}}}{\sqrt{X_{\mathbf{P}_{\mathrm{CCE}}^{(o)}}{}^2 + Y_{\mathbf{P}_{\mathrm{CCE}}^{(o)}}{}^2}} \end{cases} . \tag{4.47}$$

4.7 Geometric Error of Simplified Cutter

The cutting edges of simplified and genuine cutter are two space curves, which are defined on normal plane and rake plane respectively. Since in tooth generation process the tool surface is used, in the section 3 we calculate the tool surface cross section on normal plane. From the difference between their cross section we know how much the geometric error of the simplified tool surface (see Fig. 4.12).

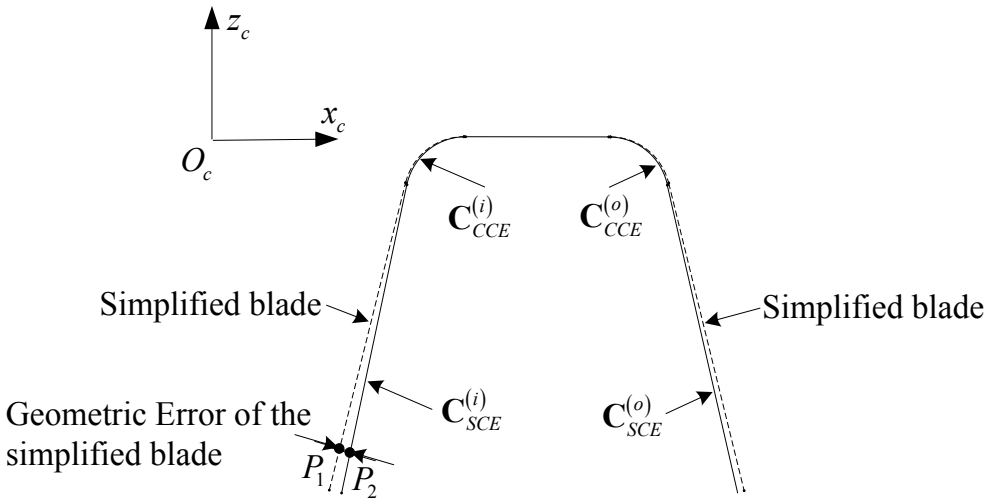

Figure 4.12 Geometric error calculation of the simplified cutter.

To calculate the geometric error along the cutting edge, assume point P_1 is on simplified blade, we can find a nearest point P_2 on cross section of genuine tool surfaces. The geometric error at point P_1 can be represented as

$$error = |P_2 - P_1|. \tag{4.48}$$

4.8 Applications

To demonstrate the geometric error of the simplified cutter, some examples are conducted. In the first example, the inner and out blades of one cutter are tested. The genuine cutter and tool surface geometric models are built up (see Fig. 4.13). The simplified cutter geometric model is also built up, and the parametric equations of simplified cutter are presented in appendix. The geometric errors along the cutting edges are calculated. For the inner and outer blades, they have the same back rake angle, end relief angle, side rake angle, side relief angle and blade angle (see Table 4.1).

Table 4.1 Geometric parameters of the blade.

Bake rake angle	20^o	End relief angle	12^o
Side rake angle	10^o	Side relief angle	4^o
Inner blade angle	22.5^o	Outer blade angle	22.5^o
Depth of blade	17.8 mm	Corner radius	1 mm
Average cutter radius	152.4 mm	Point width	2.54 mm

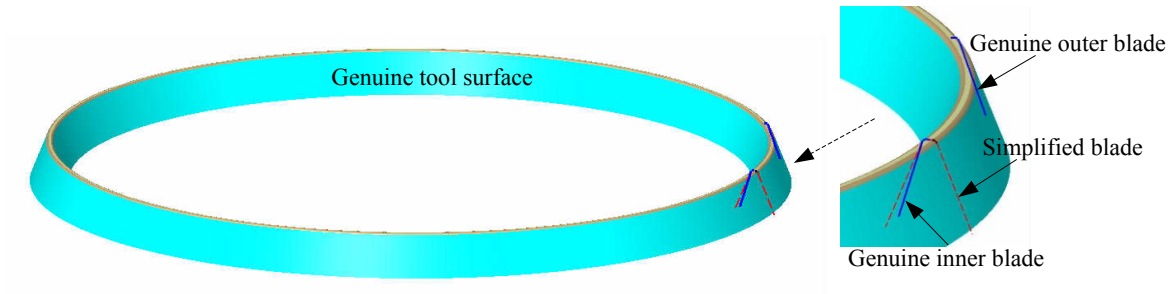

Figure 4.13 Genuine cutter and tool surface geometric models.

The cross sections of tool surfaces on normal plane are displayed in S_c (see Fig. 4.14). The errors of simplified inner blade and outer blade along the cutting edges are calculated. Since the surface generated by top cutting edge will not affect the mating of pair of gears, the errors analysis only focus on side cutting edge and circular cutting edge. Fig. 4.15 shows the geometric errors of the simplified cutter. From the first example we find that the geometric errors from blade top to bottom are gradually increasing (see Fig. 4.15). The geometric error of inner blade are larger than the error of outer blade because the distance of outer blade to z_c is larger than the distance of inner blade to z_c. For the inner blade, the maximum geometric error is about 0.53 mm, and for the outer blade, the maximum error is about 0.32 mm. Since in the machining process not all the cutting edge segments participate in the material remove, we care more about the geometric error around mean point. The geometric error at the mean point of the inner blade is about 0.21 mm, and for the outer blade, it is about 0.17 mm.

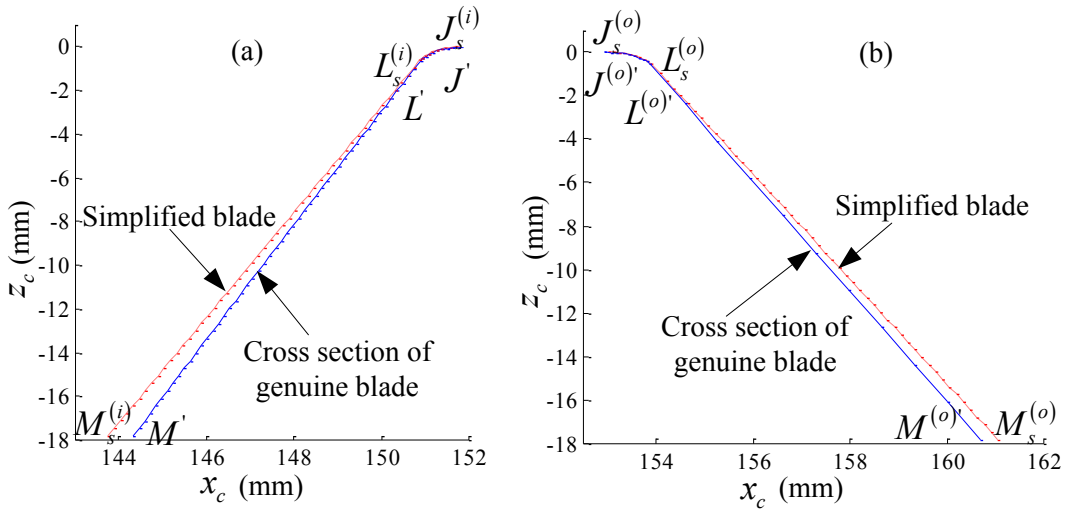

Figure 4.14 Cross section of the blades: (a) inner blade, (b) outer blade.

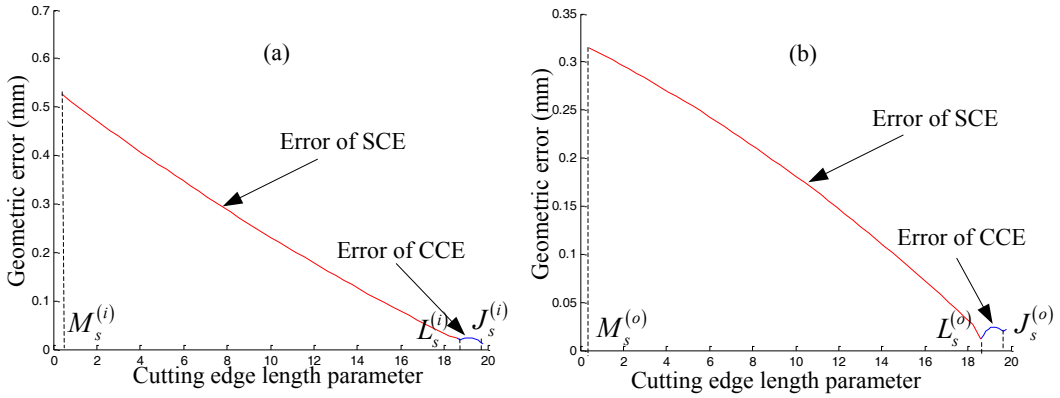

Figure 4.15 Geometric errors of the simplified blades: (a) inner blade, (b) outer blade.

In the following tests, the effects of the geometric angle on the geometric errors are analyzed (see Fig. 4.16). Since the calculation of pinion machine settings is based on the mean point, the following geometric errors are estimated at the mean point.

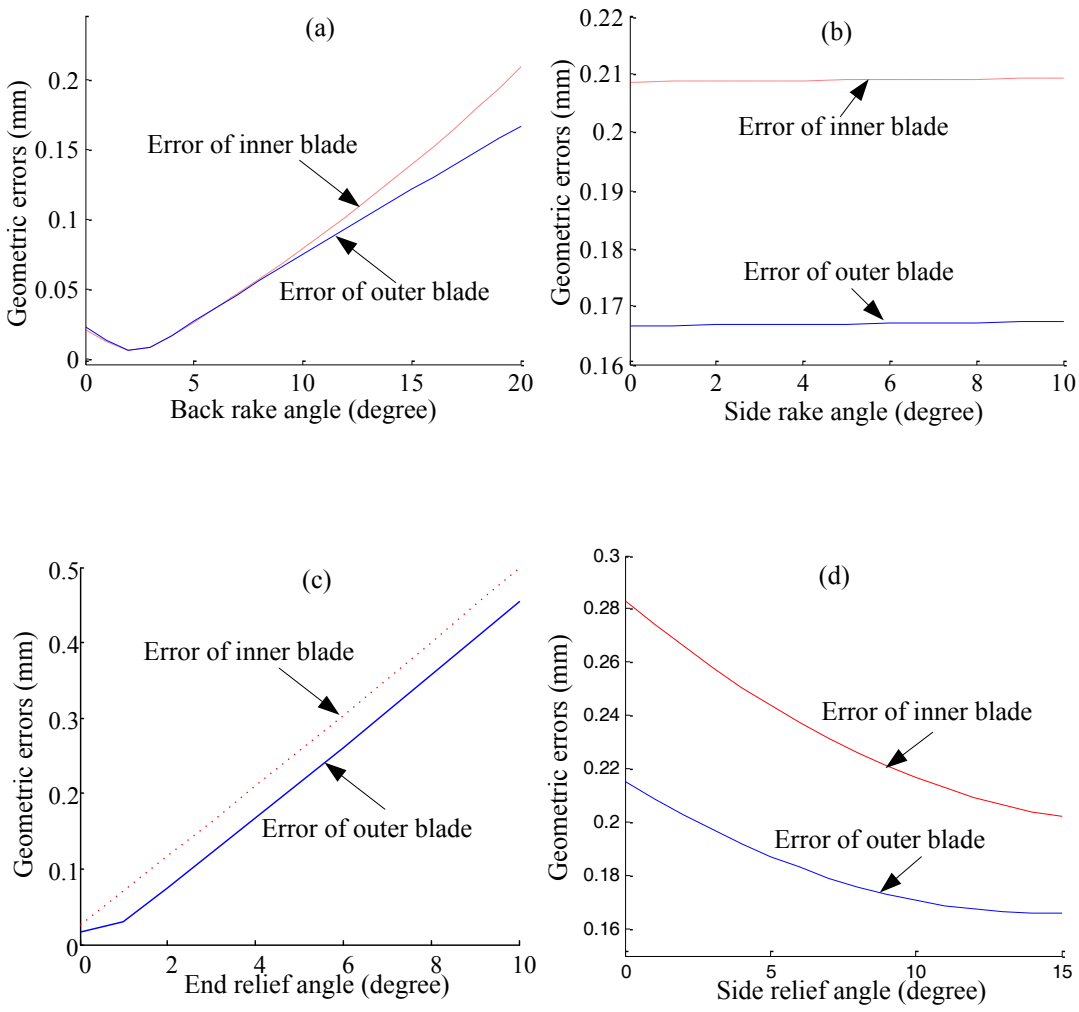

Figure 4.16 Geometric errors with parameter varying: (a) back rake angle, (b) side rake angle, (c) end relief angle, (d) side relief angle.

In test (a) we keep the same geometric parameters in the first test except changing the back rake angle from 0^o to 20^o. It shows that with the back rake angle increasing the geometric errors will decrease at the beginning, and then gradually increase. The minimum errors of inner and outer blade are about 0.007 mm. The maximum error for inner blade is about 0.21 mm, and for out blade is about 0.17 mm. In test (b) the side rake angle varies from 0^o to 10^o. The result shows that with the side rake angle changing, the

geometric errors almost keep the constant. In test (c) the end relief angle varies from 0^o to 10^o. The result shows with the end relief angle increasing, the geometric errors of inner blade keep on increasing from 0.02 mm to 0.50 mm, and the errors of outer blade increases from 0.01 mm to 0.45 mm. In test (d) the side relief angle varies from 0^o to 15^o. It shows that with the side relief angle increasing, the geometric errors of inner blade gradually decrease from 0.28 mm to 0.20 mm, and the errors of outer blade decrease from 0.21 mm to 0.16 mm.

From the tests we can see the geometric errors of the simplified cutter cannot be neglected in cutter modeling, and the different cutter parameters have different effect on the cutter, so we have to take these parameters into consideration in cutter modeling.

4.9 Summary

To achieve the accurate and real face-milled spiral bevel and hypoid gears, a genuine geometric model of cutter is proposed in this chapter. By taken the rake angles and relief angles into consideration, we accurately represent the cutting edges on the rake plane, rather than the cutting edges of the simplified blade are built up on the normal plane. In the applications we observe the geometric errors of the simplified cutter are big enough and cannot be neglected. This genuine cutter model is the foundation to build up the accurate gear tooth surfaces. With this model it is possible for high speed face-milled used for gear tooth finishing, and the accurate roughing tooth surface also benefit to the finishing cutter.

Chapter 5 Modeling of Accurate Tooth Surface of Face-Milled Spiral Bevel Gears with Genuine Cutter Geometric Model

5.1 Introduction

Spiral bevel gear is a kind specific hypoid gear when the shaft offset is equal to zero. For the member gear, there are two machining ways: non-generated and generated methods. In the non-generated gear tooth machining, the gear tooth just simply duplicates the tool surface. For the generated gear tooth machining, the gear tooth is the envelope of the tool surface family. In the work, the member gear will be machined by non-generated method. The pinion tooth only can be machined by generated method. In the introduction we discussed the importance of the accurate gear tooth surface for the tooth finishing process and the tooth roughing process. In the chapter 4, a genuine cutter geometric model is proposed. In this chapter, by using this genuine cutter geometric model, the gear tooth surfaces of spiral bevel is developed. In the final one example of spiral bevel machining is conducted to show how to build up the tooth geometry, and demonstrate the geometric error of the simplified gear teeth.

5.2 Genuine Cutter Geometric Model

The cutter for the face-milled spiral bevel and hypoid gears is composed of a group of inner and outer blades, which are alternatively mounted on the cutter plates with angle ϕ_p. For the genuine blade, the side cutting edge (SCE) is a straight line, and the circular cutting edge (CCE) is an arc. Both of them are located on the rake plane (Fig. 5.1), and can be defined in cutter coordinate system S_c. For the simplified blade, the cutting edges are defined the blade normal plane, and here it is the $x_c z_c$ plane.

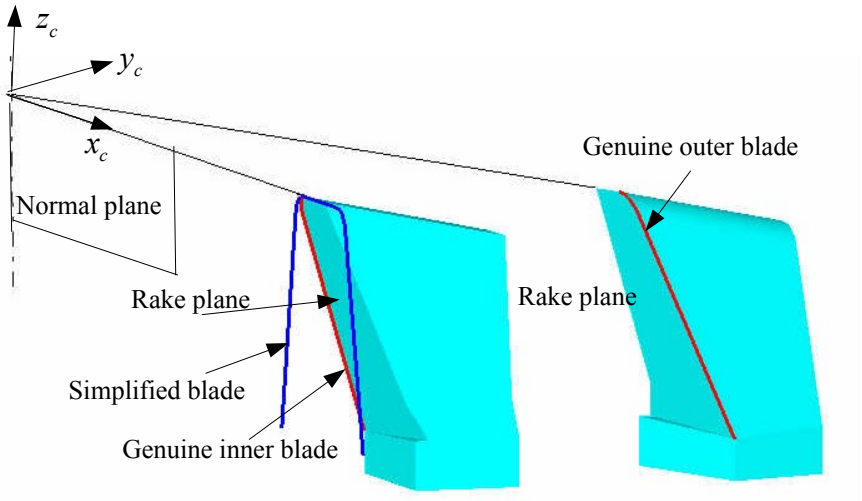

Figure 5.1 Blades in cutter coordinate system.

The tool surface is the generated by the cutting edges revolving about the cutter axis. To compare the genuine blade to the simplified blade, the cross section of the tool surface on $x_c z_c$ plane is taken. In Fig. 5.2 $C_{SCE}^{(i)}$ and $C_{SCE}^{(o)}$ are the respective cross sections of tool surfaces generated by inner blade SCE and out blade SCE. We find they are hyperbolas, instead of the straight lines as simplified cutter defined. $C_{CCE}^{(i)}$ and $C_{CCE}^{(o)}$ are

the respective cross sections of tool surfaces generated by inner blade CCE and out blade CCE. They are more complicated curves, instead of the arcs as simplified cutter defined.

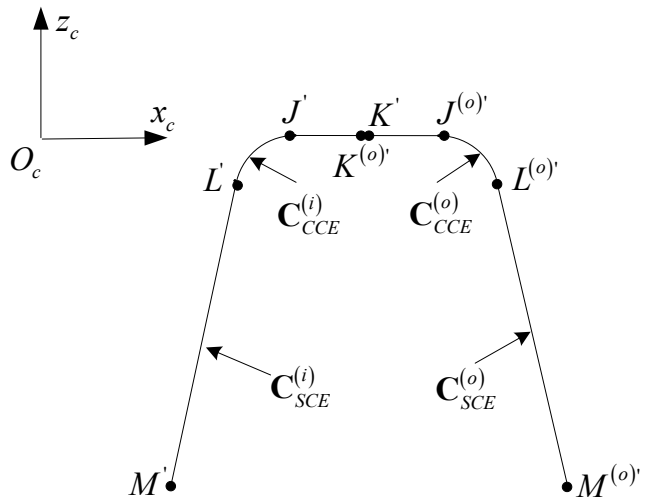

Figure 5.2 Cross sections of tool surface on $x_c z_c$ plane.

5.3 Rational Bézier Curve Representation of $C_{SCE}^{(i)}$ and $C_{SCE}^{(o)}$

The cross section $C_{SCE}^{(i)}$ and $C_{SCE}^{(o)}$ can be represented as rational Bézier curves since they are hyperbolas. Points L' and M' are two ends of $C_{SCE}^{(i)}$ (see Fig. 5.3).

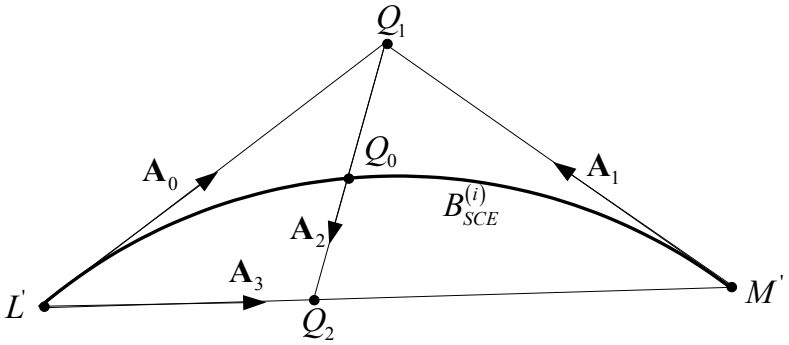

Figure 5.3 Hyperbola curve of $C_{SCE}^{(i)}$.

Vectors $\mathbf{A}_0$ and $\mathbf{A}_1$ are the tangent directions of $L'M'$ at points L' and M', it can be represented as

$$\mathbf{A}_0 = \begin{bmatrix} X_{A_0} \\ Z_{A_0} \end{bmatrix} = \begin{bmatrix} \dfrac{X_{L_c} \cdot \left(X_{M_c} - X_{L_c} \right) + Y_{L_c} \cdot \left(Y_{M_c} - Y_{L_c} \right)}{\sqrt{X_{L_c}{}^2 + Y_{L_c}{}^2}} \\ Z_{M_c} - Z_{L_c} \end{bmatrix}, \tag{5.1}$$

and

$$\mathbf{A}_1 = \begin{bmatrix} X_{A_1} \\ Z_{A_1} \end{bmatrix} = \begin{bmatrix} \dfrac{X_{M_c} \cdot \left(X_{M_c} - X_{L_c} \right) + Y_{M_c} \cdot \left(Y_{M_c} - Y_{L_c} \right)}{\sqrt{X_{M_c}{}^2 + Y_{M_c}{}^2}} \\ Z_{M_c} - Z_{L_c} \end{bmatrix}. \tag{5.2}$$

Here, $M_c = \begin{bmatrix} X_{M_c} & Y_{M_c} & Z_{M_c} \end{bmatrix}^{\mathrm{T}}$ and $L_c = \begin{bmatrix} X_{L_c} & Y_{L_c} & Z_{L_c} \end{bmatrix}^{\mathrm{T}}$ are the two ends of inner blade SCE. Their corresponding cross section points M' and L' are

$$\begin{cases} M' = \begin{bmatrix} X_{M_c'} & Z_{M_c'} \end{bmatrix}^T = \begin{bmatrix} \sqrt{X_{M_c}{}^2 + Y_{M_c}{}^2} & Z_{M_c} \end{bmatrix}^T \\ L' = \begin{bmatrix} X_{L_c'} & Z_{L_c'} \end{bmatrix}^T = \begin{bmatrix} \sqrt{X_{L_c}{}^2 + Y_{L_c}{}^2} & Z_{L_c} \end{bmatrix}^T \end{cases}. \tag{5.3}$$

Q_1 is the intersection of $\mathbf{A}_0$ and $\mathbf{A}_1$. Here assume $\mathbf{A}_0$ is not parallel to $\mathbf{A}_1$, and Q_1 be derived as

$$Q_1 = \begin{bmatrix} X_{L_c'} + X_{A_0} \cdot \dfrac{X_{A_1} \cdot \left(Z_{M_c'} - Z_{L_c'} \right) + Z_{A_1} \cdot \left(X_{L_c'} - X_{M_c'} \right)}{Z_{A_0} \cdot X_{A_1} - Z_{A_1} \cdot X_{A_0}} \\ Z_{L_c'} + Z_{A_0} \cdot \dfrac{X_{A_1} \cdot \left(Z_{M_c'} - Z_{L_c'} \right) + Z_{A_1} \cdot \left(X_{L_c'} - X_{M_c'} \right)}{Z_{A_0} \cdot X_{A_1} - Z_{A_1} \cdot X_{A_0}} \end{bmatrix}. \tag{5.4}$$

The hyperbola $C_{SCE}^{(i)}$ can be represented as a quadratic rational Bézier curve

$$\mathbf{B}_{SCE}^{(i)}(u)=\frac{(1-u)^2\cdot w_0\cdot L_c^{'}+2\cdot u\cdot(1-u)\cdot w_1\cdot Q_1+u^2\cdot w_2\cdot M_c^{'}}{(1-u)^2\cdot w_0+2\cdot u\cdot(1-u)\cdot w_1+u^2\cdot w_2}\qquad(0\le u\le 1).\quad(5.5)$$

Set $w_0=w_2=1$. The only unknown item in $\mathbf{B}_{SCE}^{(i)}$ is w_1. When $w_1=0$, we obtain the straight line $\overline{L^{'}M^{'}}$, yielding

$$L^{'}M^{'}(u)=\frac{(1-u)^2\cdot M_c^{'}+u^2\cdot L_c^{'}}{(1-u)^2+u^2}.\qquad(5.6)$$

Assume one point Q_0 is on the curve $C_{SCE}^{(i)}$ with parameter $u_2=\overline{u_2}$, the point Q_0 can be written as

$$Q_0\left(\overline{u_2}\right)=\begin{bmatrix}\sqrt{\left[X_{L_c}+\overline{u_2}\cdot\left(X_{M_c}-X_{L_c}\right)\right]^2+\left[Y_{L_c}+\overline{u_2}\cdot\left(Y_{M_c}-Y_{L_c}\right)\right]^2}\\ Z_{L_c}+\overline{u_2}\cdot\left(Z_{M_c}-Z_{L_c}\right)\end{bmatrix}.\qquad(5.7)$$

Extend the line $\overline{Q_1Q_0}$, and it will intersect with line $\overline{L^{'}M^{'}}$ at point Q_2, which can be derived as

$$Q_2=\begin{bmatrix}X_{Q_1}+X_{A_2}\cdot\dfrac{X_{A_3}\cdot\left(Z_{L_c^{'}}-Z_{Q_1}\right)+Z_{A_3}\cdot\left(X_{Q_1}-X_{L_c^{'}}\right)}{Z_{A_2}\cdot X_{A_3}-Z_{A_3}\cdot X_{A_2}}\\ Z_{Q_1}+Z_{A_2}\cdot\dfrac{X_{A_3}\cdot\left(Z_{L_c^{'}}-Z_{Q_1}\right)+Z_{A_3}\cdot\left(X_{Q_1}-X_{L_c^{'}}\right)}{Z_{A_2}\cdot X_{A_3}-Z_{A_3}\cdot X_{A_2}}\end{bmatrix},\qquad(5.8)$$

with

$$\begin{cases} \mathbf{A}_2 = \begin{bmatrix} X_{A_2} & Z_{A_2} \end{bmatrix}^T = Q_1 - Q_0 \\ \mathbf{A}_3 = \begin{bmatrix} X_{A_3} & Z_{A_3} \end{bmatrix}^T = M' - L' \end{cases}.$$

Replace Q_2 back to the straight line $\overline{L'M'}$, we can obtain

$$Q_2(u^{(0)}) = \frac{\left(1-u^{(0)}\right)^2 \cdot M_c' + \left(u^{(0)}\right)^2 \cdot L_c'}{\left(1-u^{(0)}\right)^2 + \left(u^{(0)}\right)^2}, \tag{5.9}$$

and then we can derive the equation of the parameter $u^{(0)}$ as

$$\frac{\left(u^{(0)}\right)^2}{\left(1-u^{(0)}\right)^2} = \frac{Q_2 - M_c'}{L_c' - Q_2}. \tag{5.10}$$

Assume $a_5 = \sqrt{\frac{\left|Q_2 - M_c'\right|}{\left|L_c' - Q_2\right|}}$, and we can get $u^{(0)} = \frac{a_5}{1+a_5}$. Replace $u^{(0)}$ back to the equation $\mathbf{B}_{SCE}^{(i)}$ at point Q_0 we can obtain

$$w_1 = \frac{\left(1-u^{(0)}\right)^2 \cdot \left(M_c' - Q_0\right) + \left(u^{(0)}\right)^2 \cdot \left(L_c' - Q_0\right)}{2 \cdot u^{(0)} \cdot \left(1-u^{(0)}\right) \cdot \left(Q_0 - Q_1\right)}. \tag{5.11}$$

Once we know w_1, all the parameters for the quadratic rational Bézier curve $\mathbf{B}_{SCE}^{(i)}$ are determined. The curve $\mathbf{B}_{SCE}^{(i)}$ can accurately describe the cross section of tool surface generated by inner blade SCE.

By using the same procedure we can derive the equation for the outer blade (see Fig. 5.4), the quadratic rational Bézier curve can be written as

$$\mathbf{B}_{SCE}^{(o)}(u)=\frac{(1-u)^2\cdot w_0^{(o)}\cdot L_c^{(i)'}+2\cdot u\cdot(1-u)\cdot w_1^{(o)}\cdot Q_1^{(i)}+u^2\cdot w_2^{(o)}\cdot M_c^{(i)'}}{(1-u)^2\cdot w_0^{(o)}+2\cdot u\cdot(1-u)\cdot w_1^{(o)}+u^2\cdot w_2^{(o)}} \qquad (0\le u\le 1). \tag{5.12}$$

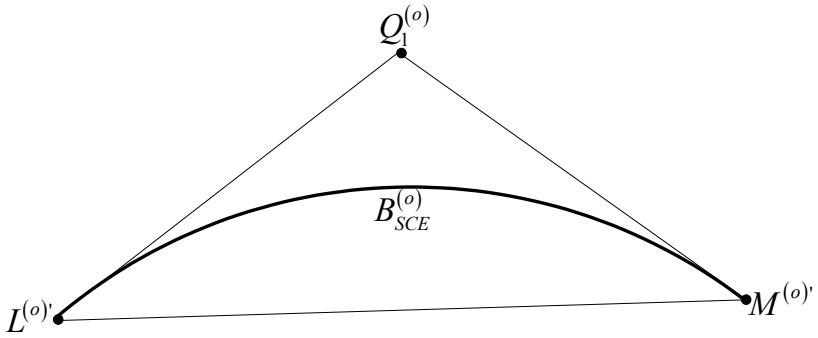

Figure 5.4 Hyperbola curve of $C_{SCE}^{(o)}$.

5.4 B-spline Representation of $C_{CCE}^{(i)}$ and $C_{CCE}^{(o)}$

$C_{CCE}^{(i)}$ and $C_{CCE}^{(o)}$ are the cross sections of the tool surfaces generated by CCE. We are trying to use B-spline curves to represent them (see Fig. 5.5). First we derive the B-spline curve for the inner blade. To represent the $C_{CCE}^{(i)}$ as a B-spline curve, the sampling points $C_0^{(i)}, C_1^{(i)}\cdots\cdots$ on curve $C_{CCE}^{(i)}$ are calculated, we seek a cubic B-spline curve

$$\mathbf{B}_{CCE}^{(i)}(u)=\sum_{j=0}^{n}N_{j,3}(u)D_j^{(i)} \qquad u\in[0,1], \tag{5.13}$$

satisfying that: $C_0^{(i)}=\mathbf{B}_{CCE}^{(i)}(0)$ and $C_m^{(i)}=\mathbf{B}_{CCE}^{(i)}(1)$, and the remaining $C_1^{(i)}\cdots\cdots$ are approximated in the lease squares

$$\sum_{j=1}^{m-1}\left|C_j^{(i)}-\mathbf{B}_{CCE}^{(i)}(u)\right|^2 ,$$

is a minimum with respect to the n+1 control points $D_0^{(i)}, D_1^{(i)} \cdots\cdots$.

By using the same procedure we can find a cubic B-spline curve for the outer blade, which can be written as

$$\mathbf{B}_{CCE}^{(o)}(u) = \sum_{j=0}^{n} N_{j,3}(u) D_j^{(o)} \qquad u \in [0,1]. \tag{5.14}$$

Here, $C_0^{(o)}, C_1^{(o)} \cdots\cdots$ are the sampling points, and $D_0^{(o)}, D_1^{(o)} \cdots\cdots$ are the control points. Since interpolating method is used to approximate the cross sections, it is important to control the accuracy within defined tolerance. There are two ways to increase the accuracy. One is increasing the degree, and the other way is increasing the number of control points. Here we fix the degree, and use a cubic B-spline. Thus our goal is to satisfy the defined tolerance using as few as possible control points. At the beginning few control points are taken, and gradually increase the curve accuracy by using more control points, up to make the curve within defined tolerance.

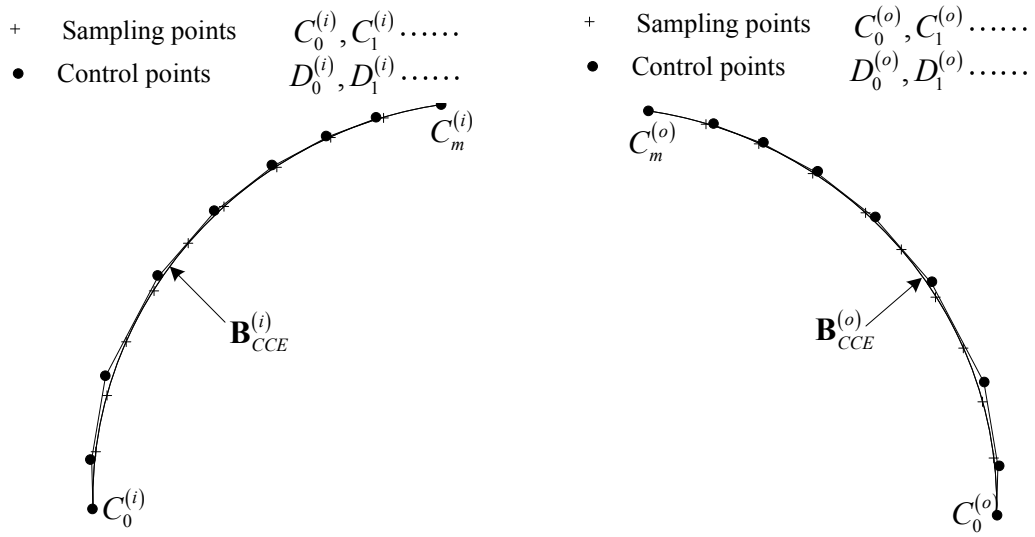

(a) Cross section of inner blade (b) Cross section of outer blade

Figure 5.5 B-spline representation of $C_{CCE}^{(i)}$ and $C_{CCE}^{(o)}$.

5.5 Tool Surfaces Represented as NURBS

The tool surfaces can be achieved by revolving of the cutting edges about the cutter axis z_c. We assume the tool surfaces are continuous surfaces, like grinder surface. First we derive the the tool surface generated by inner blade SCE (see Fig. 5.6).

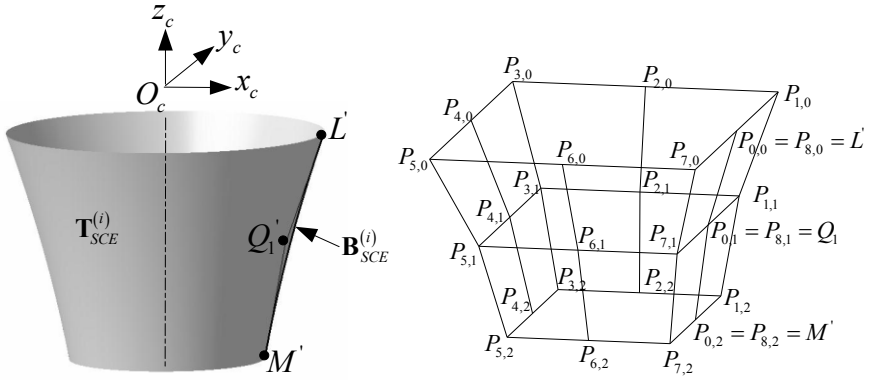

(a) NURBS tool surface (b) Control ployhedron

Figure 5.6 NURBS tool surface generated by SCE.

The NURBS surface revolved by inner blade SCE can be represented as

$$\mathbf{T}_{SCE}^{(i)}(u,v)=\sum_{j=0}^{2}\sum_{k=0}^{8}\cdot N_{j,2}(u)N_{k,2}(v)P_{j,k}^{w}\qquad(0\le u\le 1,0\le v\le 1). \tag{5.15}$$

For easy representation the hyperbola control points $L^{'}$, Q_1 and $M^{'}$ are written as $P_{0,0}$, $P_{0,1}$, and $P_{0,2}$ respectively. w_k is the weight of the rational Bézier curve $\mathbf{B}_{SCE}^{(i)}$. This hyperbola is the generatrix of the tool surface $\mathbf{T}_{SCE}^{(i)}$. In the other direction we use the nine control points circle representation. The knot vector of the circle is $V=\left\{0,0,0,\frac{1}{4},\frac{1}{4},\frac{1}{2},\frac{1}{2},\frac{3}{4},\frac{3}{4},1,1,1\right\}$, and weights $w_j=\left\{1,\frac{\sqrt{2}}{2},1,\frac{\sqrt{2}}{2},1,\frac{\sqrt{2}}{2},1,\frac{\sqrt{2}}{2},1\right\}$. For a unit circle on XY plane, it can be represented as

$$C_c=\sum_{j=0}^{8}N_{j,2}(v)\cdot P_j^{w}\qquad(0\le v\le 1), \tag{5.16}$$

with the control points of hyperbola and unit circle, the control polyhedron of the $\mathbf{T}_{SCE}^{(i)}$ can be written as

$$P_{j,k}^{w}=\begin{bmatrix} w_{j,k}\cdot X_{P_{0,k}}\cdot X_{P_k} \\ w_{j,k}\cdot X_{P_{0,k}}\cdot Y_{P_k} \\ w_{j,k}\cdot Z_{P_{0,k}} \\ w_{j,k} \end{bmatrix},$$

with $w_{j,k}=w_j\cdot w_k$.

The $x_c z_c$ cross section of inner blade CCE is a cubic B-spline curve, with $n+1$ control points $P_{0,2}\cdots$. The B-spline curve can be treated as NURBS curve with weight equal to 1.

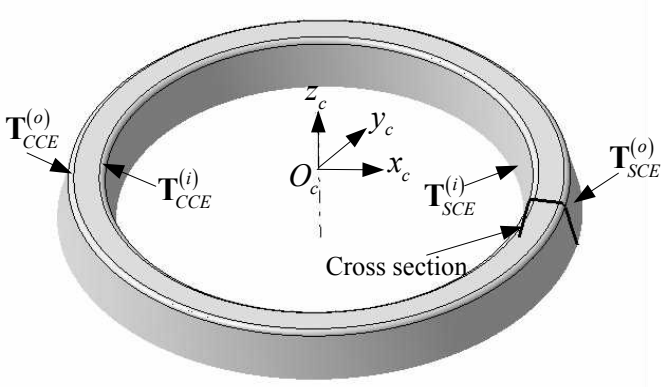

Figure 5.7 Tool surfaces represented as NURBS.

In Eq. 5.17, $\mathbf{T}_{CCE}^{(i)}$, $\mathbf{T}_{CCE}^{(o)}$ and $\mathbf{T}_{SCE}^{(o)}$ are the tooth surfaces generated by inner blade CCE, outer blade CCE and SCE respectively.

$$\begin{cases} \mathbf{T}_{CCE}^{(i)}(u,v) = \sum_{j=2}^{n+2}\sum_{k=0}^{8} \cdot N_{j,2}(u) N_{k,2}(v) P_{j,k}^{w} & (0 \le u \le 1, 0 \le v \le 1) \\ \mathbf{T}_{CCE}^{(o)}(u,v) = \sum_{j=n+7}^{2\cdot n+7}\sum_{k=0}^{8} \cdot N_{j,2}(u) N_{k,2}(v) P_{j,k}^{w} & (0 \le u \le 1, 0 \le v \le 1) \\ \mathbf{T}_{SCE}^{(o)}(u,v) = \sum_{j=2\cdot n+7}^{2\cdot n+9}\sum_{k=0}^{8} \cdot N_{j,2}(u) N_{k,2}(v) P_{j,k}^{w} & (0 \le u \le 1, 0 \le v \le 1) \end{cases}, \qquad (5.17)$$

5.6 Generation of Member Gear Tooth Surface

Member gear tooth can be machined with generated or non-generated method. In this work non-generated method is used. For the non-generated method the gear tooth just duplicates the tool surface, thus the member gear tooth can be obtained by transforming

the tool surface from S_c to gear coordinate system S_g. Fig. 5.8 shows the kinematics of member gear tooth generation. The coordinate system S_g is connecting to gear blank, and z_g is its center axis. Coordinate system S_{f1} connects to the machine frame, and $y_{f1}z_{f1}$ plane is called machine setting plane. ΔX_m is the withdrawal of gear crossing point from machine setting plane. γ_2 is the machine root angle setting. The origin of cutter coordinate system S_c locates on the machine setting plane. H_2 is the horizontal coordinate of the cutter center, and V_2 is the vertical coordinate. In one tooth machining process, the work table which gear blank installed on will feed in $z_{\mathrm{C}}^{\mathrm{G}}$ or x_{f1} direction, and the head cutter rotates about z_c, but cradle keeps stationary. Thus in the member gear machining process with non-generated method gear tooth surface simply duplicates the shape of the tool surface.

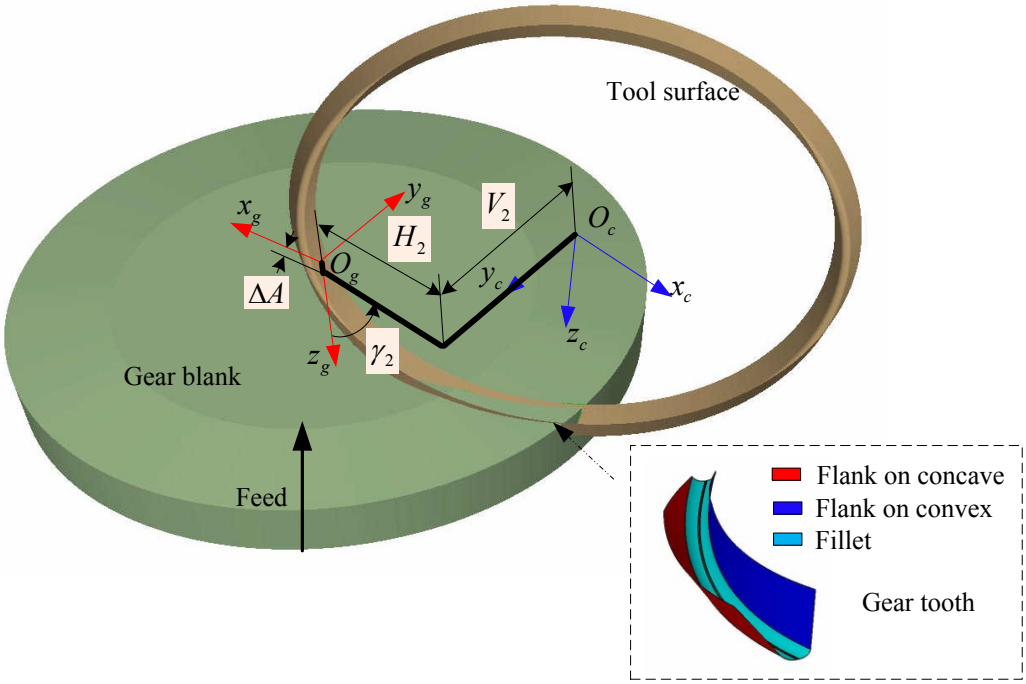

Figure 5.8 Kinematics of member gear tooth generation.

In above we derived the tool surfaces $\mathbf{T}_{SCE}^{(i)}$, $\mathbf{T}_{CCE}^{(i)}$, $\mathbf{T}_{SCE}^{(o)}$ and $\mathbf{T}_{CCE}^{(o)}$ in S_c. They can be transformed to S_g just by transforming its control points from S_c to S_g. This is one advantage to represent the tooth surfaces in NURBS. The gear tooth surfaces can be represented as

$$\begin{cases} \mathbf{G}_{SCE}^{(i)}(u,v) = \sum_{j=0}^{2}\sum_{k=0}^{8} \cdot N_{j,2}(u) N_{k,2}(v) P_{j,k}^{G,w} & (0 \le u \le 1, 0 \le v \le 1) \\ \mathbf{G}_{CCE}^{(i)}(u,v) = \sum_{j=2}^{n+2}\sum_{k=0}^{8} \cdot N_{j,2}(u) N_{k,2}(v) P_{j,k}^{G,w} & (0 \le u \le 1, 0 \le v \le 1) \\ \mathbf{G}_{SCE}^{(o)}(u,v) = \sum_{j=2\cdot n+7}^{2\cdot n+9}\sum_{k=0}^{8} \cdot N_{j,2}(u) N_{k,2}(v) P_{j,k}^{G,w} & (0 \le u \le 1, 0 \le v \le 1) \\ \mathbf{G}_{CCE}^{(o)}(u,v) = \sum_{j=n+7}^{2\cdot n+7}\sum_{k=0}^{8} \cdot N_{j,2}(u) N_{k,2}(v) P_{j,k}^{G,w} & (0 \le u \le 1, 0 \le v \le 1) \end{cases} . \quad (5.18)$$

$\mathbf{P}_{i,j}^{G}$ is the control point in S_g, and $w_{i,j}^{G}$ is the weight. They can be obtained from

$$\begin{bmatrix} X^G_{P_{j,k}} \\ Y^G_{P_{j,k}} \\ Z^G_{P_{j,k}} \\ w^G_{j,k} \end{bmatrix} = M_{GC} \cdot \begin{bmatrix} X_{P_{j,k}} \\ Y_{P_{j,k}} \\ Z_{P_{j,k}} \\ w_{j,k} \end{bmatrix}. \tag{5.19}$$

where $\mathbf{P}_{i,j}$ is the control point in S_c, and M_{GC} is the transformation matrices from S_c to S_g, which can be written as

$$\begin{aligned} M_{GC} &= Trans\left(z,-\Delta A\right)\cdot Rot\left(y,-\gamma_2\right)\cdot Trans\left(y,V_2\right)\cdot Trans\left(z,H_2\right)\cdot Rot\left(z,\pi\right)\cdot Rot\left(y,-\tfrac{\pi}{2}\right) \\ &= \begin{bmatrix} -\sin\gamma_2 & 0 & \cos\gamma_2 & -H_2\cdot\sin\gamma_2 \\ 0 & -1 & 0 & V_2 \\ \cos\gamma_2 & 0 & \sin\gamma_2 & H_2\cdot\cos\gamma_2-\Delta A \\ 0 & 0 & 0 & 1 \end{bmatrix} \end{aligned} \tag{5.20}$$

The size and shape of the bevel gear blanks are changed with different tooth taper. Here a general gear blank model is given (see Fig. 5.9). This model can represent the standard depth taper with a common apex for the pitch cone, root cone and face cone, and represent the uniform depth taper with the same face, pitch and root angle. The gear blank model is defined in the S_g. Parameter Γ_r is the gear root angle. Γ_p is the gear pitch angle. Γ_f is the gear face angle. l_m is the mean length of gear pitch cone generatrix. f_w is the gear face width.

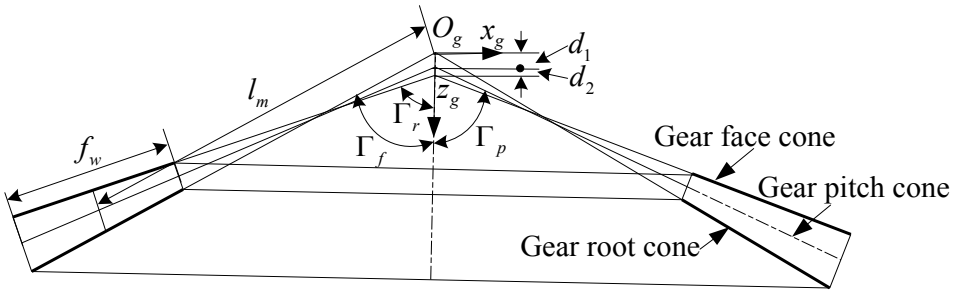

Figure 5.9 Bevel gear blank.

5.7 Generation of Pinion Tooth Surface

In most cases the axes of gear and pinion of spiral bevel gears are perpendicular to each other. For the spiral bevel gear, the relative position of S_g and S_p (pinion coordinate system) can be described by pinion angle φ_g in case of perpendicular shaft (see Fig. 5.10).

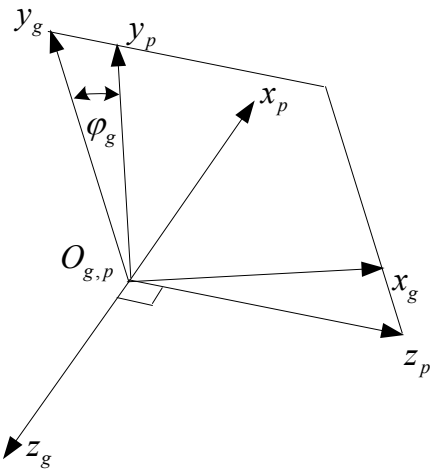

Figure 5.10 Relative position between S_g and S_p.

The transformation matrix from S_p to S_g can be written as

$$M_{gp} = \begin{bmatrix} 0 & -\sin\varphi_g & -\cos\varphi_g & 0 \\ 0 & \cos\varphi_g & -\sin\varphi_g & 0 \\ 1 & 0 & 0 & 0 \\ 0 & 0 & 0 & 1 \end{bmatrix}.$$

5.8 Kinematics of Pinion Tooth Generation

Pinion tooth surface can be only machined by generated method. Fig. 5.11 shows the kinematics of pinion tooth generating. The pinion tool surface is defined in S_c, which is the revolving surface of blade cutting edges. The blade rotating velocity is not related to the tooth generation speed. We assume the tool surface is a continuous surface like the grinder surface. The cutter plate is rigidly connected to cradle. Unlike the cradle and gear blank keep stationary in the non-generated method, in one tooth cutting process the cradle is rotating about z_{m2} with angular velocity ω_c in the generated method, and the pinion blank is rotating about z_p with angular velocity ω_p. S_{m2} is connecting to the machining tool. Assume ϕ_{c2} and ϕ_2 are the respective cradle and pinion blank rotation angles. For the modified roll, the pinion angle ϕ_2 and ϕ_{c2} have the relation

$$\phi_2 = m_{pc} \cdot \phi_{c2} + a_1 \cdot {\phi_{c2}}^2 + a_2 \cdot {\phi_{c2}}^3, \tag{5.21}$$

where m_{pc} is the ratio of roll, a_1 and a_2 are the coefficients of modified roll.

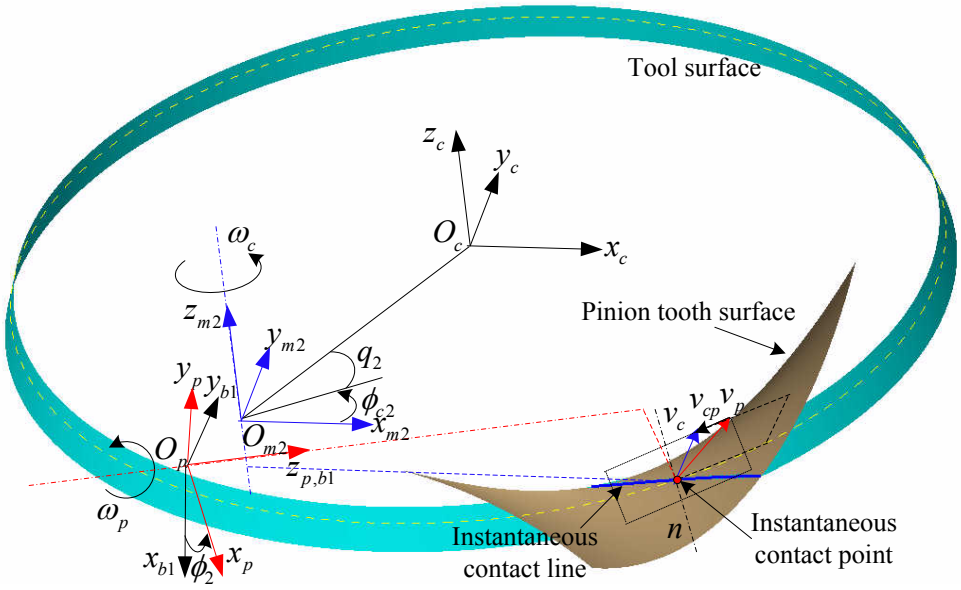

Figure 5.11 Kinematics of pinion tooth generation.

Pinion tooth surface is the envelope of the pinion tool surfaces. At each cradle rotation moment, the tool surface has an instantaneous contact line with pinion tooth surface. At each instantaneous contact point on the line, the relative velocity v_{cp} between tool surface and pinion tooth surface is perpendicular their common normal direction n.

5.9 Genuine Pinion Tooth Surface

Based on the above kinematics of pinion tooth generating and the genuine tool surface, the family surfaces generated by the inner blade side cutting edge can be represented in S_p as

$$\mathbf{R}_S^{(i)}\left(u,v,\phi_2\right)=M_{pc}\left(\phi_2\right)\cdot\mathbf{T}_{SCE}^{(i)}(u,v)\quad\begin{pmatrix}0\le u\le 1\\0\le v\le 1\\0\le\varphi_i\le 2\cdot\pi\end{pmatrix}. \tag{5.22}$$

Here, M_{pc} is the transformation matrices from S_c to S_p, which can be derived from Fig. 5.12 as

$$\begin{aligned} M_{pc} &= M_{pb1} \cdot M_{b1m2} \cdot M_{m2b2} \cdot M_{b2c} \\ &= Rot(z,-\phi_2) \cdot Trans(z,-\Delta A_2) \cdot Rot(y,\tfrac{\pi}{2}-\gamma_{m2}) \cdot Trans(z,-\Delta B_2) \\ &\cdot Trans(y,E_{m2}) \cdot Rot(z,\phi_{c2}) \cdot Trans(y,S_{r2}\cdot\sin q_2) \cdot Trans(x,S_{r2}\cdot\cos q_2) \end{aligned} \quad . \quad (5.23)$$

with

$$M_{pc}(1) = \begin{bmatrix} \cos(\phi_2)\cdot\sin(\gamma_{m2})\cdot\cos(\phi_{c2}) + \sin(\phi_2)\cdot\sin(\phi_{c2}) \\ -\sin(\phi_2)\cdot\sin(\gamma_{m2})\cdot\cos(\phi_{c2}) + \cos(\phi_2)\cdot\sin(\phi_{c2}) \\ \cos(\gamma_{m2})\cdot\cos(\phi_{c2}) \\ 0 \end{bmatrix},$$

$$M_{pc}(2) = \begin{bmatrix} -\cos(\phi_2)\cdot\sin(\gamma_{m2})\cdot\sin(\phi_{c2}) + \sin(\phi_2)\cdot\cos(\phi_{c2}) \\ \sin(\phi_2)\cdot\sin(\gamma_{m2})\cdot\sin(\phi_{c2}) + \cos(\phi_2)\cdot\cos(\phi_{c2}) \\ -\cos(\gamma_{m2})\cdot\sin(\phi_{c2}) \\ 0 \end{bmatrix},$$

$$M_{pc}(2) = \begin{bmatrix} -\cos(\phi_2)\cdot\cos(\gamma_{m2}) \\ \sin(\phi_2)\cdot\cos(\gamma_{m2}) \\ \sin(\gamma_{m2}) \\ 0 \end{bmatrix},$$

$$M_{pc}(4) = \begin{bmatrix} \cos(\phi_2)\cdot\left[\sin(\gamma_{m2})\cdot S_{r2}\cdot\cos q_2 + \cos(\gamma_{m2})\cdot\Delta B_2\right] + \sin(\phi_2)\cdot\left[S_{r2}+E_{m2}\right] \\ -\sin(\phi_2)\cdot\left[\sin(\gamma_{m2})\cdot S_{r2}\cdot\cos q_2 + \cos(\gamma_{m2})\cdot\Delta B_2\right] + \cos(\phi_2)\cdot\left[S_{r2}\cdot\sin q_2 + E_{m2}\right] \\ \cos(\gamma_{m2})\cdot S_{r2}\cdot\cos(\phi_2) - \sin(\gamma_{m2})\cdot\Delta B_2 - \Delta A_2 \\ 1 \end{bmatrix}.$$

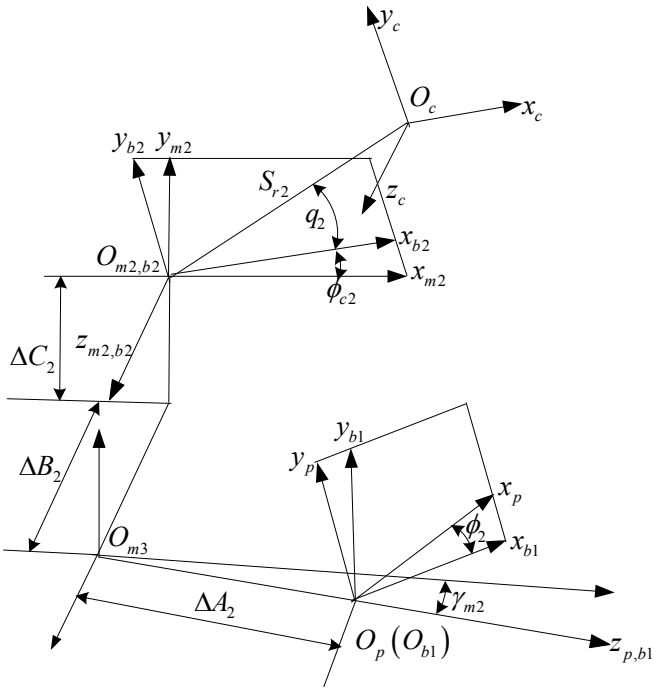

Figure 5.12 Machine settings for pinion tooth generation.

Here a non-tilted blade is used, so the z_c is parallel to the cradle center axis. The coordinate system S_{b2} is connected to cradle, and S_{b1} is connected to machining tool. S_{r2} is the radial setting. ΔC_2 is the machine offset. ΔB_2 is the sliding base, and ΔA_2 is the machine center to back. γ_{m2} is the machine root angle.

In the pinion tooth generation, at the instantaneous contact point, v_{cp} is perpendicular to n, which can be written as the mesh equation

$$f_S^{(i)}\left(u, v, \phi_2\right) = n \cdot v^{(cp)} = 0\,. \tag{5.24}$$

Here, $n^{(2)}$ and $v^{(cp)}$ can be represented in S_{m2}. The normal n in S_{m2} can transformed from normal on tool surface in S_c as

$$n = L_{m2b2} \cdot L_{b2c} \cdot n_c . \tag{5.25}$$

Here, L_{m2b2}, L_{b2b} and L_{b2c} are the matrices with first three rows and columns of corresponding matrices of M_{m2b2} and M_{b2c}. The normal of the tool surface in S_c can be represented as

$$n_c = \frac{\partial \mathbf{T}_{SCE}^{(i)}(u,v)}{\partial u} \times \frac{\partial \mathbf{T}_{SCE}^{(i)}(u,v)}{\partial v} . \tag{5.26}$$

The relative velocity $v^{(cp)}$ can be expressed as

$$v^{(cp)} = \left(\omega_c - \omega_p\right) \times r_{m2} + \overline{O_{m2}O_{m3}} \times \omega_p . \tag{5.27}$$

r_{m2} is the tool surface in S_{m2}, which can be transformed from S_c as

$$r_{m2} = M_{m2b2} \cdot M_{b2b} \cdot M_{b2c} \cdot \mathbf{T}_{SCE}^{(i)}(u,v) . \tag{5.28}$$

The vector $\overline{O_{m2}O_{m3}}$ can be represented as $\overline{O_{m2}O_{m3}} = \begin{bmatrix} 0 & -\Delta C_2 & \Delta B_2 \end{bmatrix}^{\mathrm{T}}$. Assume ω_p is a unit vector, which can be represent in S_{m2} as $\omega_p = \begin{bmatrix} \cos\gamma_{m2} & 0 & \sin\gamma_{m2} \end{bmatrix}^{\mathrm{T}}$. The ω_c can be represented as $\omega_c = \begin{bmatrix} 0 & 0 & m_{cp} \end{bmatrix}^{\mathrm{T}}$. The roll ratio can be expressed as

$$m_{cp} = \frac{1}{m_{pc} \cdot +2 \cdot a_1 \cdot \phi_{c2} + 3 \cdot a_2 \cdot {\phi_{c2}}^2} . \tag{5.29}$$

Combining the Eq. 5.25 and Eq. 5.27, the flank on the pinion convex side can be represented in S_p as

$$\begin{cases} \mathbf{R}_S^{(i)}(u,v,\phi_2) = M_{pc}(\phi_2)\cdot \mathbf{T}_{SCE}^{(i)}(u,v) \\ f_S^{(i)}(u,v,\phi_2) = 0 \end{cases}. \tag{5.30}$$

By using the same procedure, the fillet on pinion convex side can be represented in S_p as

$$\begin{cases} \mathbf{R}_C^{(i)}(u,v,\phi_2) = M_{pc}(\phi_2)\cdot \mathbf{T}_{CCE}^{(i)}(u,v) \\ f_C^{(i)}(u,v,\phi_2) = 0 \end{cases}. \tag{5.31}$$

For the pinion concave tooth surfaces, we can derive them with the same way. But the machine settings for the concave and convex sides are different. The flank on pinion concave side can be represented in S_p as

$$\begin{cases} \mathbf{R}_S^{(o)}(u,v,\phi_2) = M_{pc}(\phi_2)\cdot \mathbf{T}_{SCE}^{(o)}(u,v) \\ f_S^{(o)}(u,v,\phi_2) = 0 \end{cases}, \tag{5.32}$$

and the fillet on pinion concave side can be represented in S_p as

$$\begin{cases} \mathbf{R}_C^{(o)}(u,v,\phi_2) = M_{pc}(\phi_2)\cdot \mathbf{T}_{CCE}^{(o)}(u,v) \\ f_C^{(o)}(u,v,\phi_2) = 0 \end{cases}. \tag{5.33}$$

5.10 Pinion Tooth Surface Represented as NURBS Surface

The above pinion tooth surfaces are represented by three parameters in two dependent equations. It cannot directly be used in CAD software. In this work we represent the pinion tooth surfaces as NURSB surface. First we figure out the contact

points from the above tooth surface equations, and then use NURBS surfaces to interpolate these points.

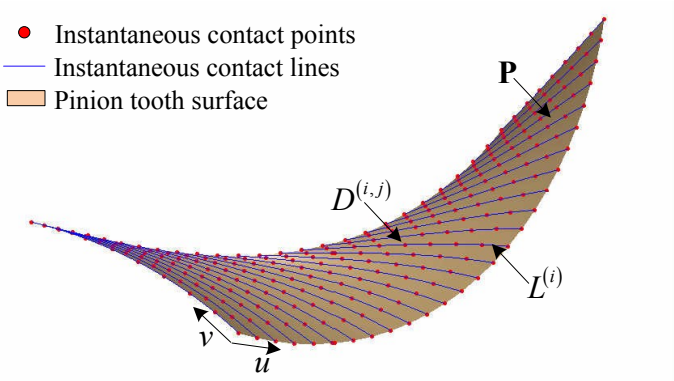

Figure 5.13 Pinion tooth surface represented as NURBS surface.

In the pinion tooth generation, at each cradle rotation moment the tool surface has line contact with the pinion tooth surface (see Fig. 5.13). With the cradle continuously rotating, the generating process will produce adjacent contact lines, which form the pinion tooth surface. This continuous process can be discretized by dividing cradle rotation angle ϕ_{c2} into small segments $\Delta\phi_{c2}$, and the corresponding pinion blank rotation angle will be $\Delta\phi_2$. Assume at cradle rotating angle $\phi_{c2}^{(i)}$ and the corresponding pinion rotating angle $\phi_2^{(i)}$, the tool surface and pinion tooth surface will contact at instantaneous contact line. We know u and v are tool surface parameters. u varies from 0 to 1, and v varies from 0 to 2π. Under a given value $u^{(j)}$ of parameter u, we can find the corresponding $v^{(j)}$ which satisfies the mesh equation. There may be two solutions for $v^{(j)}$. We choose the solution which is intersecting with the pinion blank. The parameters $\phi_2^{(i)}$,

$u^{(j)}$ and $v^{(j)}$ determine the instantaneous contact point $\mathbf{D}^{(i,j)}$. which can be calculated from the equation

$$\begin{cases} \mathbf{R}_S^{(i)}\left(u^{(j)}, v^{(j)}, \phi_2^{(i)}\right) = M_{pc}\left(\phi_2^{(i)}\right) \cdot \mathbf{T}_{SCE}^{(i)}(u^{(j)}, v^{(j)}) \\ f_S^{(i)}\left(u^{(j)}, v^{(j)}, \phi_2^{(i)}\right) = 0 \end{cases}. \tag{5.34}$$

When u varies from 0 to 1, we can find a series of contact points, which form the instantaneous contact line at $\phi_2^{(i)}$. One NURBS curve $\mathbf{L}^{(i)}$ with degree d_1 can be used to interpolate these contact points.

$$\mathbf{L}^{(i)}(v) = \sum_{k=0}^{m} N_{k,d_1}(v)\mathbf{Q}_{k,j}. \tag{5.35}$$

With the cradle rotating, a series of contact line can be generated with different ϕ_2. One NURBS surface can be used to interpolate all of them, which can be represented as

$$\mathbf{P}(u,v) = \sum_{k=0}^{m}\sum_{l=0}^{n} N_{k,d_1}(u) N_{l,d_2}(v)\mathbf{T}_{k,l}. \tag{5.36}$$

Here $\mathbf{T}_{k,l}$ are the control net points. The NURBS surface $\mathbf{P}$ allows us to represent the pinion tooth surface in CAD software very conveniently, and it is easy to manipulate. Since we just need to calculate the few control points instead of tons of sampling points, to reach the same accuracy level it reduces the workload dramatically. The next step is to how to use as few as possible number of points to control the NURBS surface within tolerance. To reach this goal we have to optimize the number of sampling points and control points.

For the surface $\mathbf{P}$ only at sampling points it is exactly same as the theoretic tooth surface because of interpolation. Points out of the sampling points are approximate, so the geometric errors exist. The geometric errors can be controlled within tolerance by using the steps in Table 5.1.

Table 5.1 Procedure of pinion tooth surface generation.

Step 1	Set the number of sampling points n_0, and calculate the initial sampling points $\mathbf{D}_0$.
Step 2	Set the number of controlling points m_0, and generate the initial tooth surface $\mathbf{P}_0$ by interpolating $\mathbf{D}_0$.
Step 3	Increase the sampling points $n_0 + \Delta n$, and generate the new tooth surface $\mathbf{P}_1$.
Step 4	Calculate the geometric error between the two surfaces, $error = \lvert \mathbf{P}_1 - \mathbf{P}_0 \rvert$.
Step 5	Check if the error is large than the specified tolerance, go to Step 3, and $\mathbf{P}_0 = \mathbf{P}_1$; If the error is small than the specified tolerance, go to Step 6.
Step 6	Increase the control points $m_1 = m_0 + \Delta m$, and generate the new tooth surface $\mathbf{P}_2$.
Step 7	Calculate the geometric error between the two surfaces: $error = \lvert \mathbf{P}_2 - \mathbf{P}_1 \rvert$.
Step 8	Check if the error is large than the specified tolerance, go to Step 6, and $\mathbf{P}_1 = \mathbf{P}_2$; If the error is small than the specified tolerance, output the tooth surface.

The above algorithm is to achieve the tooth surface within specified tolerance. At the beginning, we use the small number of sampling points and controlling points, we can get a rough surface. By increasing of the sampling and control points, an improved surface which is getting closer to the theoretic tooth surface can be obtained. The distance between the rough surface and improved surface is getting smaller with the increasing of sampling and controlling points. When the distance reaches specified tolerance, we know that the geometric errors of the interpolating surface can be neglected.

5.11 Applications

To illustrate how to build up the genuine gear tooth surfaces, two examples are conducted. One is for the spiral bevel gear, and the other example is for the hypoid gears. In examples, under the given blade data, the genuine blade model is build up first, and then produce the member gear tooth surface with specified gear machine settings. After get the member gear tooth, the pinion tooth surfaces are generated with the given pinion machine settings and pinion cutter. Finally we compare the genuine gear tooth geometry and tooth contact with the simplified gear tooth geometry and tooth contact.

5.11.1 Tooth Generation of Spiral Bevel Gears

In this example, the first step is to build up the genuine blade model. Table 5.2 gives the blade data for the member gear. The inner blade and outer blade have the same geometric parameter value. There are 12 blades mounted on the cradle.

Table 5.2 Blades data for the member gear.

Bake rake angle	20.00^{o}	End relief angle	12.00^{o}
Side rake angle	10.00^{o}	Side relief angle	4.00^{o}
Inner blade angle	22.50^{o}	Outer blade angle	20.00^{o}
Point width	4.826 mm	Corner radius	2.794 mm
Average cutter radius	177.800 mm		

Based on the given blade data the geometric model of genuine and simplified blades are built up. Fig. 5.14 shows that the cross sections of simplified tool surface and genuine tool surface are different. The geometric errors of the simplified blade are calculated (see Fig. 5.15). From the result we find that the geometric errors from blade

top to bottom are gradually increasing. The geometric errors of inner blade are larger than the errors of outer blade, because the distance of outer blade to z_c is larger than the distance of inner blade to z_c. For the inner blade, the maximum geometric error is about 0.551 mm, and for the outer blade, the maximum error is about 0.374 mm.

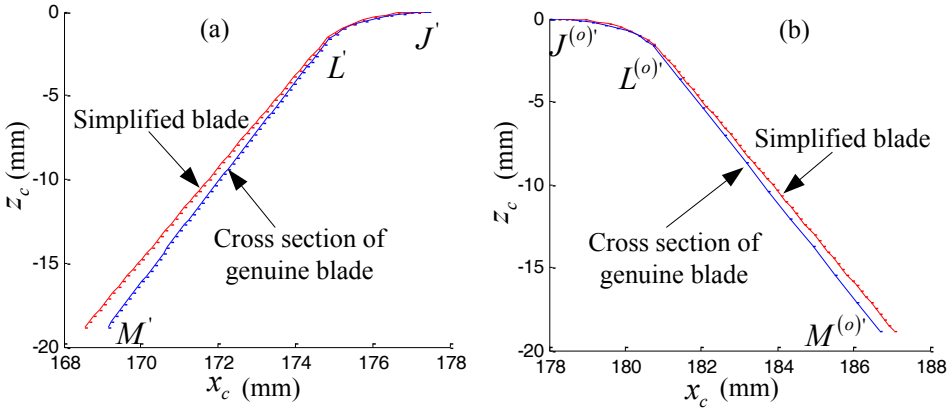

Figure 5.14 Cross sections of tool surface: (a) inner blade, (b) outer blade.

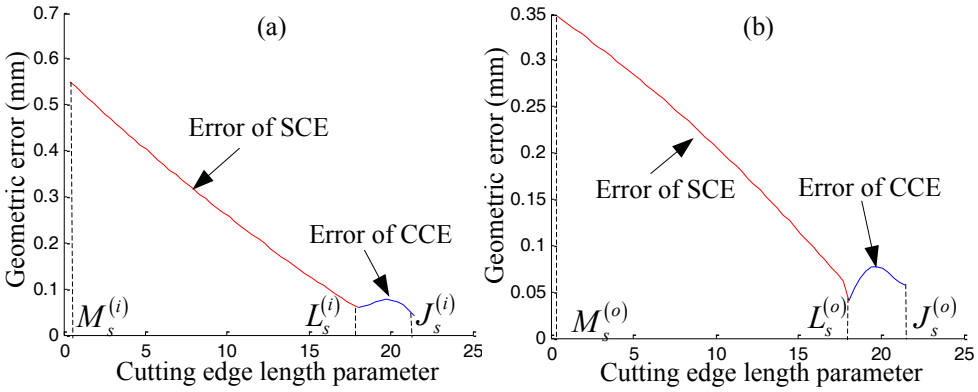

Figure 5.15 Geometric errors of the simplified blades: (a) inner blade, (b) outer blade.

The second step is to build up the member gear tooth surface with the genuine blade model. The member gear is a non-generated (Formate®) spiral bevel gear. The

machine settings of member-gear are shown in Table 5.3. The data of member gear blank are listed in Table 5.4.

Table 5.3 Machine settings of member gear.

Correction in machine center to back	-2.007 mm	Machine root angle	76.17^{o}
Cutter horizontal setting	100.152 mm	Cutter vertical setting	137.897 mm

Table 5.4 Data of member gear blank.

Gear root angle	75.13^{o}	Gear face angle	80.30^{o}
Gear face width	71.120 mm	Mean cone distance	177.521 mm
Teeth number	52	Blank depth	35.000 mm
Hand of spiral	Left hand		

The flank and fillet of the member-gear are represented by separated surfaces (see Fig. 5.16). The flanks are produced by the side cutting edges. We know that the cross section of side cutting edge is a hyperbola, which can be accurately represented by a rational Bézier curve with 3 control points. The cross section of circular cutting edge is approximated by a cubic B-spline curve, so its error should be controlled within tolerance (see Fig. 5.17). As mentioned above, we increase the accuracy by using more control points. In the test, the radius of circular cutting edge is about 2.794 mm. When 8 control points are taken, the maximum error is about 0.0019 mm. when the number of control points increases to 12, the maximum error decreases to 0.00015 mm.

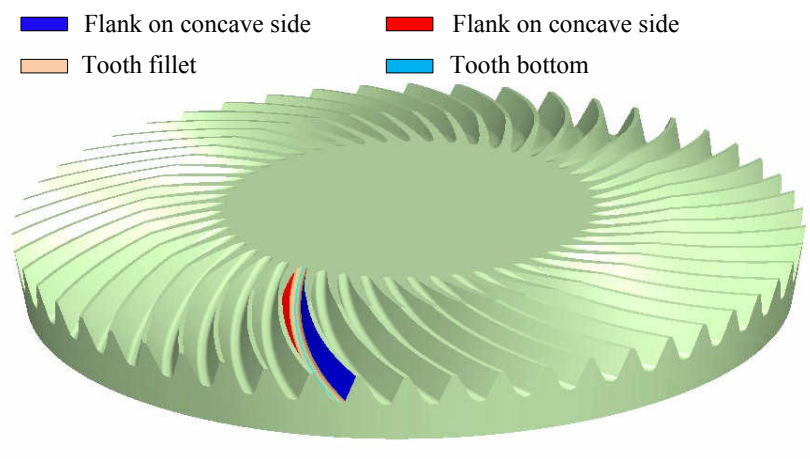

Figure 5.16 Genuine member gear tooth.

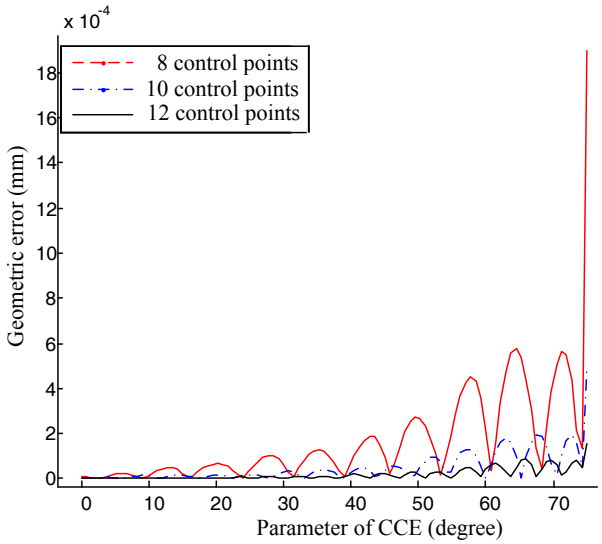

Figure 5.17 Error of CCE in B-spline with different number of control points.

The third step is to generate the pinion tooth surface with the given pinion machine settings and blade data. The pinion teeth on concave and convex sides are generated with different blades and machine settings. Table 5.5 shows the data of the pinion blades. The machine settings of pinion are listed in Table 5.6. The data of pinion blank are shown in Table 5.7.

Table 5.5 Data of the pinion blades.

	Concave side	Convex side
Bake rake angle	17.00^{o}	23.00^{o}
Side rake angle	10.00^{o}	10.00^{o}
blade angle	14.00^{o}	14.00^{o}
End relief angle	12.00^{o}	12.00^{o}
Side relief angle	4.00^{o}	4.00^{o}
Cutter point radius	174.496 mm	185.151 mm
Corner radius	2.794 mm	2.794 mm

Table 5.6 Machine settings for pinion.

	Concave side	Convex side
Machine center to back	-4.530 mm	8.134 mm
Blank offset	19.947 mm	-20.314 mm
Sliding base setting	0.339 mm	-1.795 mm
Radial setting	150.301 mm	195.018 mm
Installment angle	62.06^{o}	61.54^{o}
Machine root angle	9.70^{o}	9.70^{o}
Ratio of cutting	4.853	5.773
Coefficient of modified roll a_1	0.0302	-0.0527
Coefficient of modified roll a_2	-0.0599	0.1157

Table 5.7 Data of pinion blank.

Pinion root angle	14.87^{o}	Pinion pitch angle	79.12^{o}
Mean cone distance	177.521 mm	Face width	71.120 mm
Number of teeth	52	Hand of spiral	Right hand

Fig. 5.18 shows the pinion tooth surface generated with the above pinion blade data, machine setting and blank data. The flank and fillet on concave and convex side are

pointed out with different colors. To achieve the genuine pinion tooth surface, the following steps are taken.

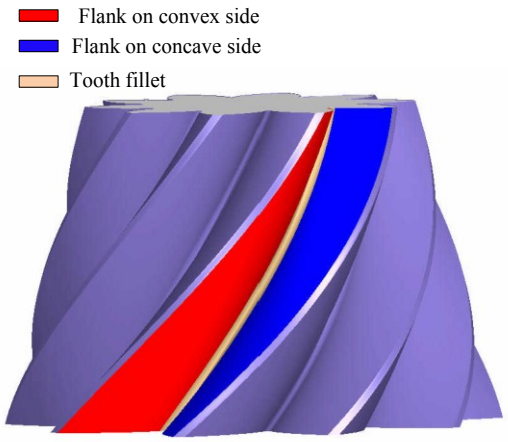

Figure 5.18 Genuine pinion tooth surface.

5.11.2 Pinion Flank on Concave Side in NURBS Surface

In this chapter we propose a method to represent the pinion tooth surface in NURBS surface, and also provide the method to control it within specified tolerance. Here one example on pinion concave flank is used to demonstrate the method. At the beginning, we figure out 6×30 initial sampling points from Eq. 5.34, and gradually increase the number of sampling points to 18×140. Difference NURBS surfaces are used to interpolate the sampling points with the same number of control points. The relative geometric errors are calculated (see Fig. 5.19). For example, we calculate the distance between the surface with 6×30 sampling points and the surface with 7×40 sampling points, the average distance is 0.0207 mm, and the maximum distance is 0.0622 mm. When the number of sampling points are increased to 18×140, the average distance is less than 0.0001 mm, and the maximum distance is 0.0006 mm. when keep on increasing

the sampling points, the distance becomes very small, and can be neglected. At this moment, the contribution of the adding sampling point to improve the tooth accuracy is trivial.

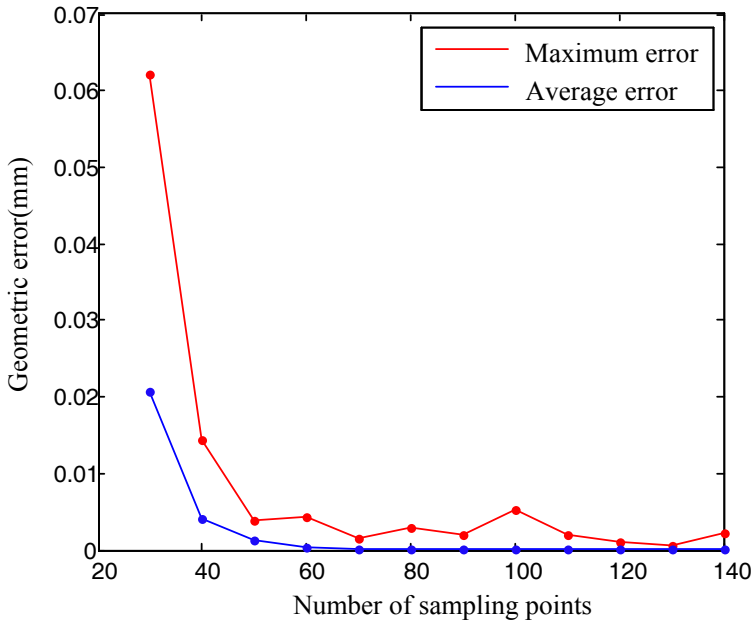

Figure 5.19 Geometric errors with the increase of sampling points.

Once the sampling points are settled down, we can optimize the control points. We gradually increase controlling points from 5×30 to 15×110, and calculate the relative geometric errors (see Fig. 5.20). When 30 control points is taken, the average geometric error is 0.001 mm, and the maximum geometric error is 0.0035 mm. When the number of control points increase to 12×90, the average error is less than 0.0002 mm, and maximum error is 0.0001 mm. Keep on increasing the control points, the contribution of the adding sampling point to improve the tooth accuracy is trivial.

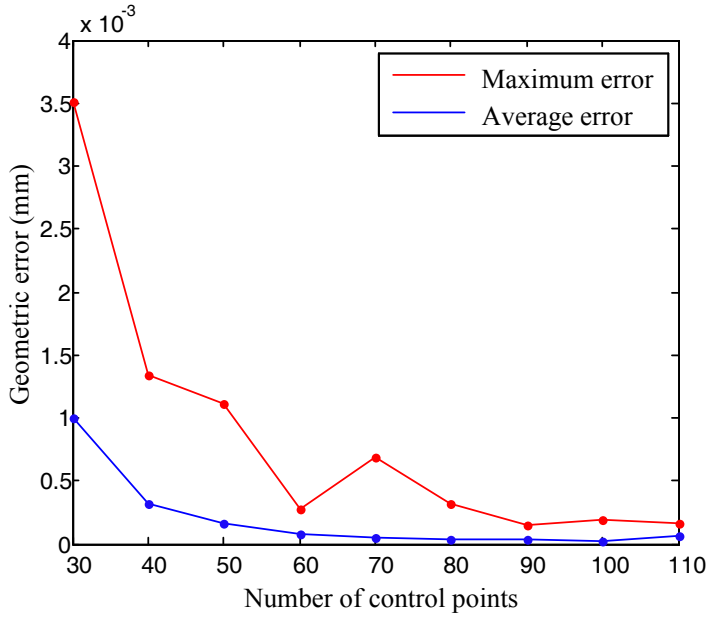

Figure 5.20 Geometric errors with the increase of control points.

Fig. 5.21 shows the calculated instantaneous contact points, instantaneous contact lines and the genuine flank tooth. For the following tooth contact analysis, the principal directions and curvatures at mean point can also be calculated.

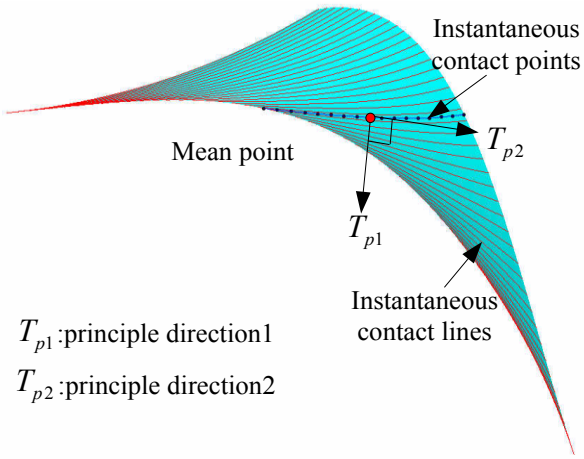

Figure 5.21 Pinion flank on concave side.

5.11.3 Calculation of Pinion Tooth Geometric Errors

In the above section, we build up the pinion flank on concave side. By using the same strategy the flank on convex side and fillets can be generated (see Fig. 5.22). The surfaces in Fig. 5.22 are the generated by the tool surface with cradle angle varying from -15^{o} to 15^{o}. The gear tooth geometric model in Fig. 5.18 can be obtained by do the intersection between these surfaces and pinion blank.

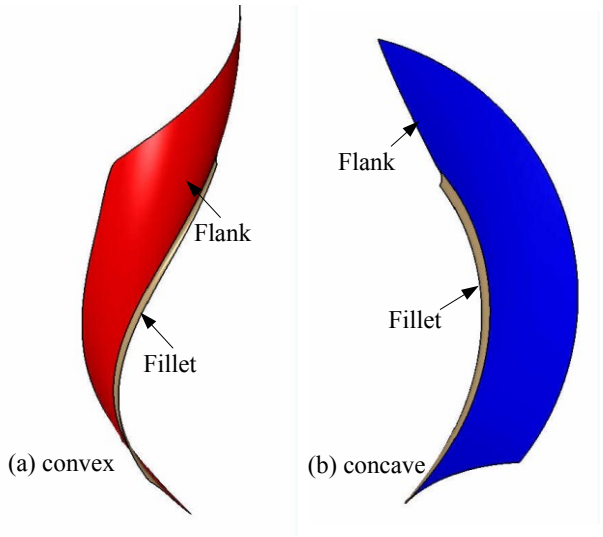

Figure 5.22 Genuine flank and fillet of pinion on concave and convex sides.

In the above pinion tooth generation process, since the genuine the blade geometric model and machining settings are exactly the same as the real pinion tooth machining process, the pinion tooth CAD model should be exact match the real tooth. We calculated the NURBS tooth surface in Matlab and output the tooth geometry as igs file, so it can be directly used by all the commercial CAD software. To estimate the geometric error of the simplified pinion tooth surface, the distance between the simplified and genuine pinion tooth surfaces is calculated.

Fig. 5.23 (a) shows the maximum geometric error of the simplified pinion flank on concave side is 0.358 mm, and the average geometric error is about 0.206 mm. Fig. 5.23 (b) shows the maximum geometric error of the simplified pinion fillet on concave side is 0.089 mm, and the average geometric error is about 0.075 mm.

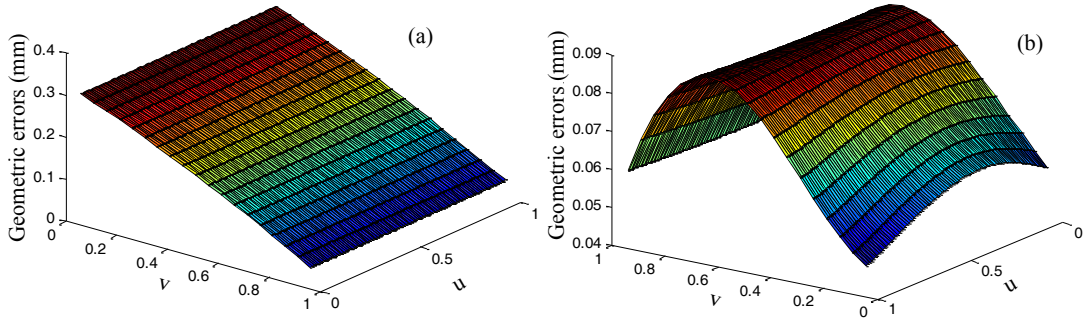

Figure 5.23 Geometric errors of simplified pinion tooth on concave side: (a) flank, (b) fillet.

The distribution of the geometric error for the simplified pinion tooth surface on concave and convex sides are different. Fig. 5.24 (a) shows the maximum geometric error of the simplified pinion flank on convex side is 0.535 mm, and the average geometric error is about 0.272 mm. Fig. 5.24 (b) shows the maximum geometric error of the simplified pinion fillet on concave side is 0.063 mm, and the average geometric error is about 0.052 mm.

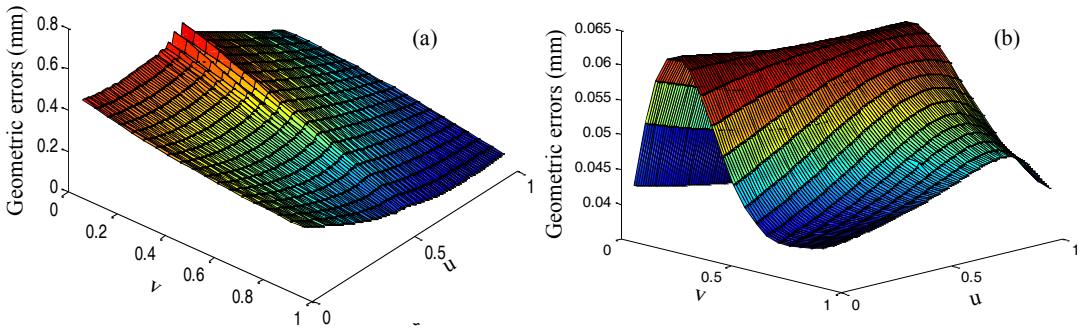

Figure 5.24 Geometric errors of simplified pinion tooth on convex side: (a) flank, (b) fillet.

One of our goals is to produce the genuine tooth surface of gear and pinion, which is exact the same as the real machined tooth surface. Another objective of this work is to provide the accurate CAD model for the FEA tooth analysis. We know the fillet is the weakest part of the whole tooth surface. Since we describe the flank and fillet with separate NURBS surfaces, it is easy to conduct adaptive meshing for the tooth. Fig. 5.25 shows the different mesh size for the flanks and fillets.

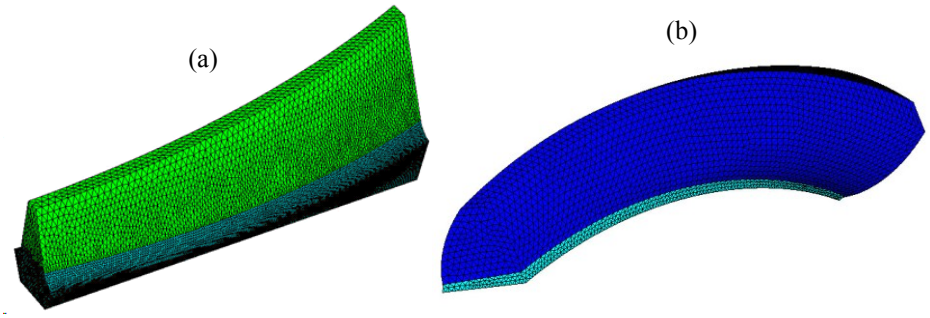

Figure 5.25 Adaptive meshing for flank and pinion: (a) gear, (b) pinion.

The last step is to evaluate the error by comparing the tooth contact of the genuine gears to the tooth contact of simplified gears at the mean point. We know the pinion tooth generation is based on the pinion blade geometric model and the pinion machine settings. The pinion machine settings is calculated based on the designed tooth contact at the mean

point, which include the length of contact ellipse major axis, the orientation of the tangent to the contact path. Since the simplified gear tooth surface does not exactly match with the real tooth surface, so the real tooth contact may be different with the tooth contact of simplified gears. Here we assemble the genuine gears and simplified gears, and compare their tooth contacts.

5.11.4 Tooth Contact of the Genuine Spiral Bevel Gears

In the above section we generate the member gear and pinion. The relative position between the member gear and pinion in the assembly can be determined from M_{gp}. In the genuine gear and pinion assemble (see Fig. 5.26), the gear convex flank and pinion concave flank will contact at the mean point, whose coordinates in S_g are $\begin{bmatrix}-171.816 & -17.851 & 36.452\end{bmatrix}^{\mathrm{T}}$. The gear and pinion tooth will form a contact ellipse under the working load. Here we assume the elastic deformation at mean point is 0.007 mm under the given load. Fig. 5.27 shows the contact ellipse of the genuine gear and pinion. $G_r^{(1)}$ and $G_r^{(2)}$ are the two principle directions of gear tooth surface at mean points, the corresponding principal curvatures are $k_{g,r}^{(1)} = -0.0006$, and $k_{g,r}^{(2)} = 0.0055$. $P_r^{(1)}$ and $P_r^{(2)}$ are the two principle directions of pinion tooth surface at mean points, the corresponding principal curvatures are $k_{p,s}^{(1)} = -0.0386$, and $k_{p,s}^{(2)} = 0.0052$. The angle between the gear and pinion principal directions $\alpha_s = 7.85^o$. The angle between $G_s^{(1)}$ and minor axis of contact ellipse β_s is 9.08°. The length of contact ellipse's major axis a_r is 23.208 mm, and the length of minor axis b_r is 1.210 mm.

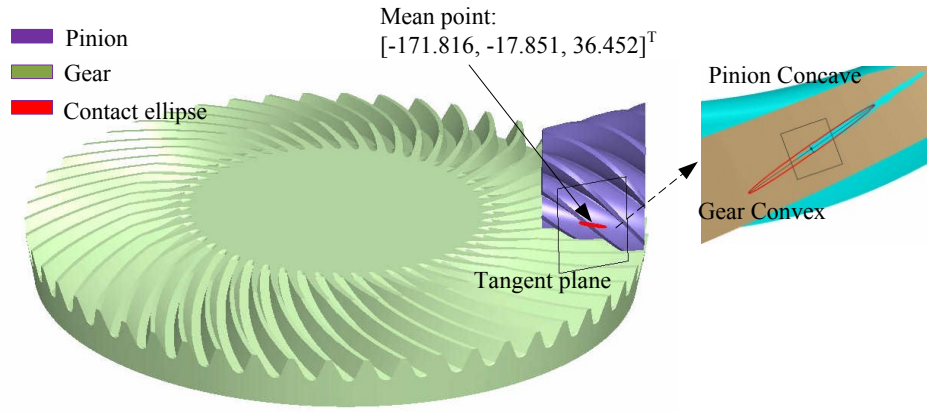

Figure 5.26 Tooth contact of genuine spiral bevel gears.

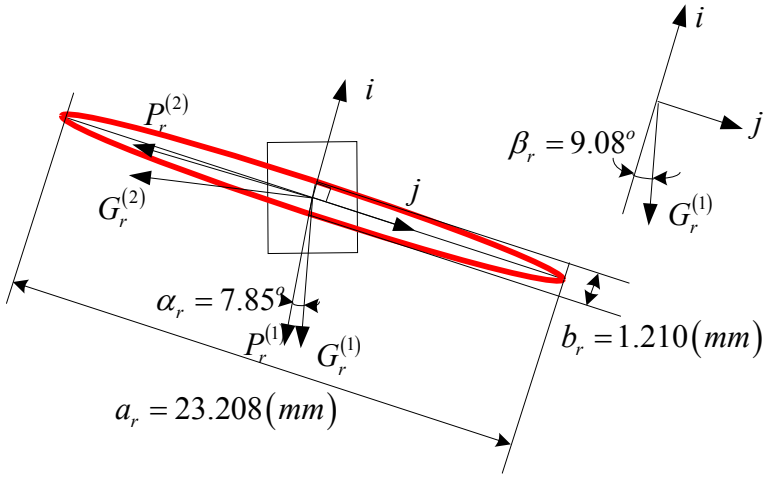

Figure 5.27 Contact ellipse of the genuine spiral bevel gears.

5.11.5 Tooth Contact of the Simplified Spiral Bevel Gears

The gear and pinion tooth are generated with simplified cutter, and assembled together (see Fig. 5.28). The gear and pinion tooth contacts at the mean point, whose coordinates in S_g are $\begin{bmatrix}-170.796 & -18.145 & 36.327\end{bmatrix}^{\mathrm{T}}$. The contact ellipse is calculated under the same load as in the genuine gears. Fig. 5.29 shows the contact ellipse of the simplified gear and pinion. $G_s^{(1)}$ and $G_s^{(2)}$ are the two principle directions of gear tooth

surface at mean points, the corresponding principal curvatures are $k_{g,s}^{(1)} = 0$, and $k_{g,s}^{(2)} = 0.0054$. $P_s^{(1)}$ and $P_s^{(2)}$ are the two principle directions of pinion tooth surface at mean points, the corresponding principal curvatures are $k_{p,s}^{(1)} = -0.0387$, and $k_{p,s}^{(2)} = 0.0052$. The angle between the gear and pinion principal directions $\alpha_s = 8.65^o$. The angle between $G_s^{(1)}$ and minor axis of contact ellipse β_s is 9.85°. The length of contact ellipse's major axis a_s is 26.092 mm, and the length of minor axis b_s is 1.201 mm.

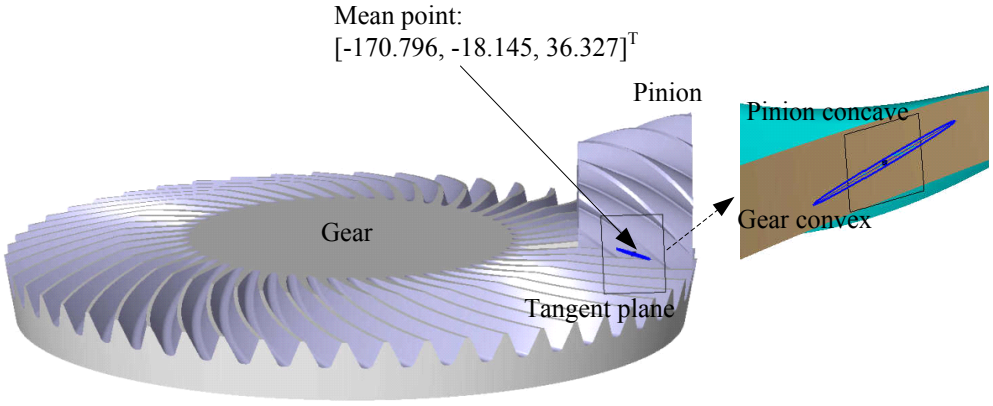

Figure 5.28 Tooth contact of simplified gears.

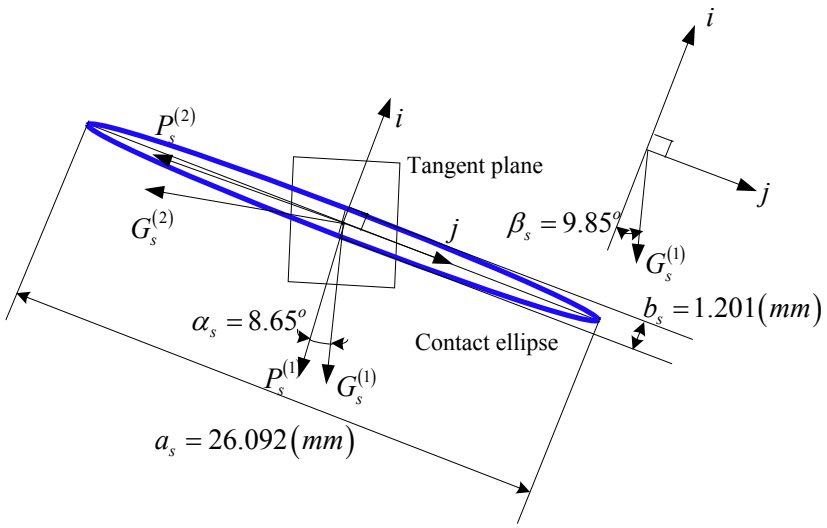

Figure 5.29 Contact ellipse of the simplified gears.

5.11.6 Compare of the Genuine and Simplified Tooth Contacts

Compare the tooth contacts of genuine and simplified gears, we find the effect of the simplified cutter on gear assembly (see Fig. 5.30). First, the gear and pinion contacts at the different mean points, and the distance between them is about 1.102 mm. Second, the lengths of the contact ellipse major axis are different. The length of the genuine gear major axis is about 23.208 mm, and for the simplified gear it is about 26.092 mm. With almost the same minor axis, the areas of genuine and simplified gear contact ellipse will be different because of the different major axes. The area of genuine gears contact ellipse is about 22.256 mm^2, and the area of simplified contact ellipse is about 24.944 mm^2. Third, the orientations of the contact ellipse are different, and the angle between their axes is about 1.08^o. The stress on the gear tooth will have a big change with the three differences.

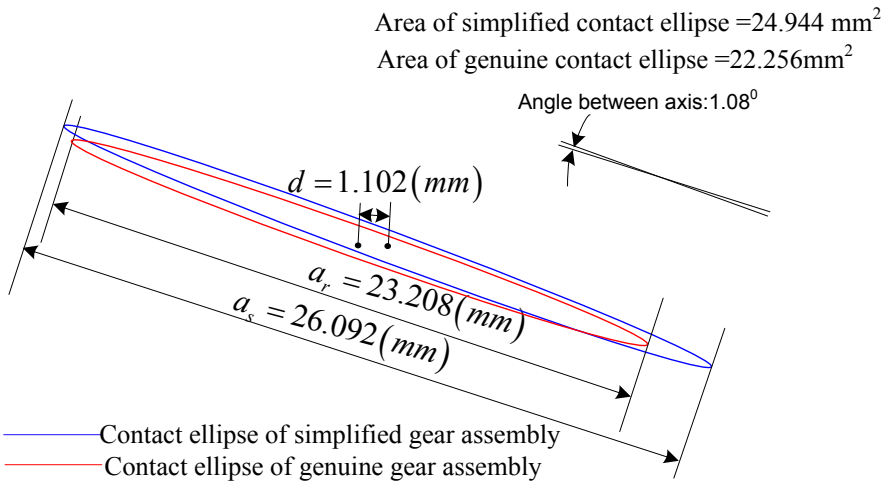

Figure 5.30 Tooth contact compare between the genuine and simplified gears.

5.12 Summary

In this chapter, a genuine cutter geometric model is built up. Based on the kinematics of tooth machining process, the gear and pinion tooth surfaces are generated with this genuine cutter, rather than the current simplified cutter. The tooth surfaces are represented as NURBS surface, and they are controlled within specified tolerance. The NURBS tooth surface can be directly implemented in CAD software. It is easy to manipulate, and provide the accurate tooth geometry and adaptive mesh for tooth FEA. In the applications we observe the geometric errors of the simplified gear and pinion tooth. The geometric errors cause the tooth contact changing at the mean point. The proposed the genuine gear tooth model can remove the discrepancy between simplified gear tooth and real machined tooth. This model lays a foundation for the high speed face-milled used in gear tooth finishing process.

Chapter 6 Modeling the Accurate Tooth Surface of Genuine Face-Milled Hypoid Gears with Genuine Cutter Geometric Model

6.1 Introduction

Hypoid gears are common used in automobile industry and helicopter for transformation of the rotation of crossed axes, which is more complicated than the spiral bevel gears, used for transformation between intersected axes. Spiral bevel gears can be treated as a special type of hypoid gears without shaft offset. The machining process of hypoid gears is similar to the spiral bevel gear machining process. In this chapter, the tooth surfaces of accurate member-gear and pinion are modeled based on the kinematics of hypoid gear and pinion generation by using the genuine cutter geometric model. The geometric error of the tooth surfaces is calculated, and the tooth contacts between genuine hypoid gears and simplified gears are compared.

6.2 Kinematics of Gear and Pinion Generation

The member gear of hypoid gears can be machined with non-generated method or generated method. In this work the non-generated method is used. For the non-generated gear, The final gear tooth surface just duplicates the tool surface, thus the gear tooth can

be obtained by transforming the tooth surface from the cutter coordinate system S_c to the gear coordinate system S_g. Fig. 6.1 shows the gear machine settings. z_g is the gear center axis. The coordinate system S_{f1} connects to the machine frame, and $y_{f1}z_{f1}$ plane is called machine setting plane. ΔX_m is the correction in machine center to back setting. γ_2 is the machine gear root angle setting. The origin of S_c locates in the machine setting plane. H_2 is the horizontal coordinate of the cutter center in S_{f1}, and V_2 is the vertical coordinate. ψ_g is the machine spiral angle. During one tooth machining, the gear blank keeps stationary; the cutter rotates about z_c, and the workpiece material will be removed with the table feeding.

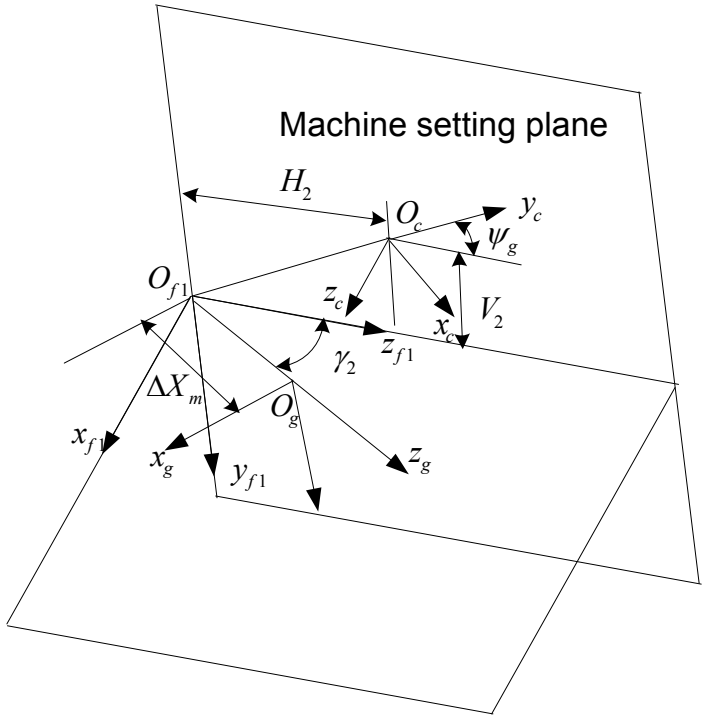

Figure 6.1 Machine settings of member gear of hypoid gears.

The transformation matrices from S_c to S_g can be represented as

$$\begin{aligned} M_{GC} &= Trans\left(z,-\Delta X_m\right)\cdot Rot\left(y,-\gamma_2\right)\cdot Trans\left(z,-H_2\right)\cdot Trans\left(y,-V_2\right) \\ &\quad \cdot Rot\left(x,\tfrac{\pi}{2}\right)\cdot Rot\left(y,\tfrac{\pi}{2}\right)\cdot Rot\left(z,\psi_x\right) \\ &= \begin{bmatrix} -\sin\gamma_2\cdot\sin\psi_x & -\sin\gamma_2\cdot\cos\psi_x & \cos\gamma_2 & -H_2\cdot\sin\gamma_2 \\ \cos\psi_x & -\sin\psi_x & 0 & -V_2 \\ \cos\gamma_2\cdot\sin\psi_x & \cos\gamma_2\cdot\cos\psi_x & \sin\gamma_2 & H_2\cdot\cos\gamma_2-\Delta X_m \\ 0 & 0 & 0 & 1 \end{bmatrix} \end{aligned} . \quad (6.1)$$

In the chapter 4, we derived the tool surfaces $\mathbf{T}_{SCE}^{(i)}$, $\mathbf{T}_{CCE}^{(i)}$, $\mathbf{T}_{SCE}^{(o)}$, $\mathbf{T}_{CCE}^{(o)}$ and their NURBS control points $\mathbf{P}_{i,j}$. The control points can be transformed from S_c to S_g as

$$\begin{bmatrix} X_{P_{j,k}}^G \\ Y_{P_{j,k}}^G \\ Z_{P_{j,k}}^G \\ w_{j,k}^G \end{bmatrix} = M_{GC}\cdot\begin{bmatrix} X_{P_{j,k}} \\ Y_{P_{j,k}} \\ Z_{P_{j,k}} \\ w_{j,k} \end{bmatrix}. \quad (6.2)$$

The gear tooth surface can be represented in S_g as

$$
\begin{cases}
\mathbf{G}_{SCE}^{(i)}(u,v)=\sum_{j=0}^{2}\sum_{k=0}^{8}\cdot N_{j,2}(u)N_{k,2}(v)P_{j,k}^{G,w} & (0\le u\le 1,0\le v\le 1)\\
\mathbf{G}_{CCE}^{(i)}(u,v)=\sum_{j=2}^{n+2}\sum_{k=0}^{8}\cdot N_{j,2}(u)N_{k,2}(v)P_{j,k}^{G,w} & (0\le u\le 1,0\le v\le 1)\\
\mathbf{G}_{TCE}^{(i)}(u,v)=\sum_{j=n+2}^{n+4}\sum_{k=0}^{8}\cdot N_{j,2}(u)N_{k,2}(v)P_{j,k}^{G,w} & (0\le u\le 1,0\le v\le 1)\\
\mathbf{G}_{TCE}^{(o)}(u,v)=\sum_{j=n+5}^{n+7}\sum_{k=0}^{8}\cdot N_{j,2}(u)N_{k,2}(v)P_{j,k}^{G,w} & (0\le u\le 1,0\le v\le 1)\\
\mathbf{G}_{CCE}^{(o)}(u,v)=\sum_{j=n+7}^{2\cdot n+7}\sum_{k=0}^{8}\cdot N_{j,2}(u)N_{k,2}(v)P_{j,k}^{G,w} & (0\le u\le 1,0\le v\le 1)\\
\mathbf{G}_{SCE}^{(o)}(u,v)=\sum_{j=2\cdot n+7}^{2\cdot n+9}\sum_{k=0}^{8}\cdot N_{j,2}(u)N_{k,2}(v)P_{j,k}^{G,w} & (0\le u\le 1,0\le v\le 1)
\end{cases}
. \qquad (6.3)
$$

Mostly the axes of gear and pinion are perpendicular to each other with a shaft offset E_s. Fig. 6.2 shows the relative positions between S_g and pinion coordinate system S_p.

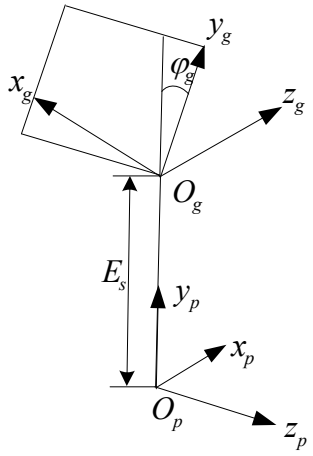

Figure 6.2 Relative position between S_g and S_p.

The transformation matrices from S_g to S_p can be represented as

$$M_{pg} = Rot\left(y, 90^o\right) \cdot Tra\left(y, E_s\right) \cdot Rot\left(z, \varphi_g\right)$$
$$= \begin{bmatrix} 0 & 0 & 1 & 0 \\ \sin\varphi_g & \cos\varphi_g & 0 & E_s \\ -\cos\varphi_g & \sin\varphi_g & 0 & 0 \\ 0 & 0 & 0 & 1 \end{bmatrix} . \quad (6.4)$$

Pinion tooth surface of hypoid gears can be machined only by generated method. Fig. 6.3 shows the pinion machine settings. Here the tilted cutters are used, which are shown in Fig. 6.4. The pinion cutters are defined in S_C, and mounted on the cradle with tilted angle i. The coordinate system S_{b2}, S_{b3} and S_{b4} are connected to cradle. j is the swivel angle. The coordinate system S_{m2} and S_{b1} is rigidly connected to machine. The angle q_2 is the initial cradle angle, and radial setting S_{r2} is the distance between O_{m2} and O_c. The parameter ΔC_2 is the machine offset. γ_{m2} is the machine root angle. ΔB_2 is the sliding base, and ΔA_2 is the machine center to back. In the pinion tooth generating process, the pinion cutter rotates about z_c; the cradle performs rotation about z_{m2} with angular velocity ω_c, and the pinion rotates about z_p with angular velocity ω_p. The ratio of roll is $m_{cp} = \frac{\phi_{c2}}{\phi_2}$.

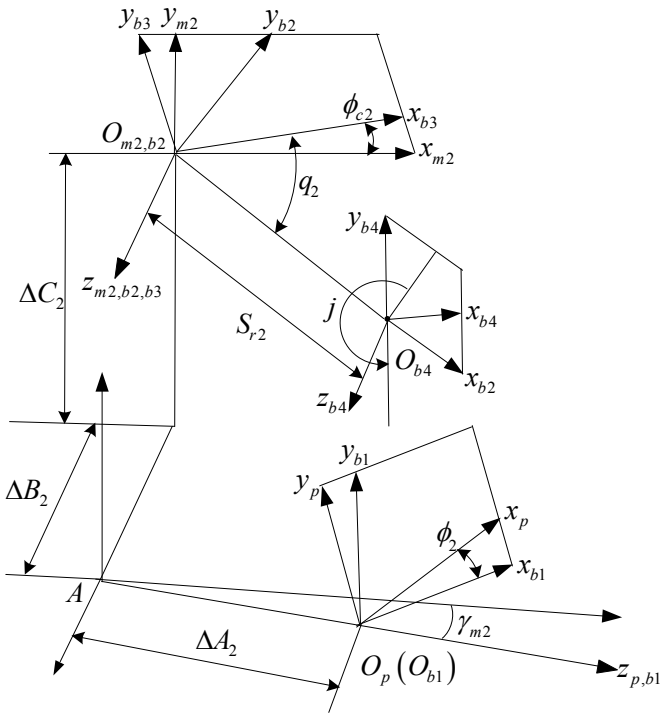

Figure 6.3 Pinion machine settings of hypoid gears.

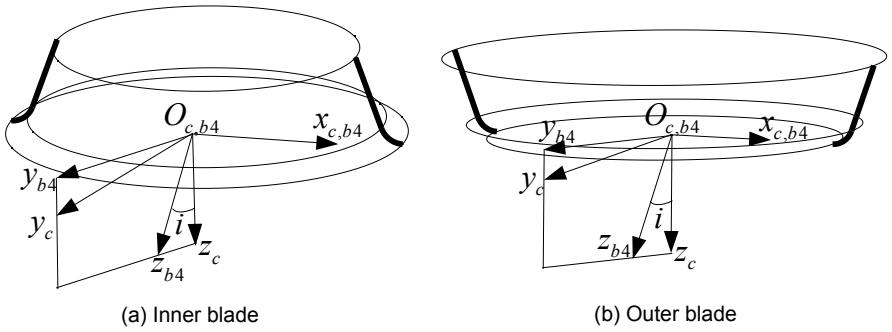

Figure 6.4 Tilted pinion cutter.

The family surface generated by the pinion inner blade side cutting edge can be represented in S_p by the matrix equation

$$\mathbf{R}_S^{(i)}\left(u,v,\phi_2\right)=M_{m2c}\cdot M_{m2c}\cdot\mathbf{T}_{SCE}^{(i)}(u,v)\qquad\begin{pmatrix}0\le u\le 1\\0\le v\le 1\\0\le\phi_2\le 2\cdot\pi\end{pmatrix}. \tag{6.5}$$

with

$$M_{m2c}=\begin{bmatrix} -\cos\left(\phi_{c2}-q_2+j\right) & \sin\left(\phi_{c2}-q_2+j\right)\cdot\cos i & -\sin\left(\phi_{c2}-q_2+j\right)\cdot\sin i & S_{r2}\cdot\cos\left(\phi_{c2}-q_2\right) \\ -\sin\left(\phi_{c2}-q_2+j\right) & -\cos\left(\phi_{c2}-q_2+j\right)\cdot\cos i & \cos\left(\phi_{c2}-q_2+j\right)\cdot\sin i & S_{r2}\cdot\sin\left(\phi_{c2}-q_2\right) \\ 0 & \sin i & \cos i & 0 \\ 0 & 0 & 0 & 1 \end{bmatrix},$$

$$M_{pm2}=\begin{bmatrix} \cos\phi_2\cdot\sin\gamma_{m2} & \sin\phi_2 & -\cos\phi_2\cdot\cos\gamma_{m2} & \cos\phi_2\cdot\cos\gamma_{m2}\cdot\Delta B_2+\sin\phi_2\cdot\Delta C_2 \\ -\sin\phi_2\cdot\sin\gamma_{m2} & \cos\phi_2 & \sin\phi_2\cdot\cos\gamma_{m2} & -\sin\phi_2\cdot\cos\gamma_{m2}\cdot\Delta B_2+\cos\phi_2\cdot\Delta C_2 \\ \cos\gamma_{m2} & 0 & \sin\gamma_{m2} & -\sin\gamma_{m2}\cdot\Delta B_2-\Delta A_2 \\ 0 & 0 & 0 & 1 \end{bmatrix}.$$

During the pinion tooth generation, it should satisfy the mesh equation, which can be represented as

$$f\left(l_i,\varphi_i,\phi_2\right)=n^{(2)}\cdot v^{(p2)}=0\,. \tag{6.6}$$

$n^{(2)}$ is the normal to the tool surface, and $v^{(p2)}$ is the relative velocity between cutter and pinion. Here, $n^{(2)}$ and $v^{(p2)}$ are represented in S_{m2}.

$$n^{(2)}=L_{m2c}\cdot n_c^{(2)}\,. \tag{6.7}$$

$$v^{(p2)}=\left(\omega_c-\omega_p\right)\times r_{m2}+\overline{O_{m2}A}\times\omega_p\,. \tag{6.8}$$

r_{m2} can be obtained by transforming the cutting edge from S_c to S_{m2}, and it can written as

$$r_{m2}=M_{m2c}\cdot\mathbf{T}_{SCE}^{(i)}\,. \tag{6.9}$$

$\overline{O_{m2}A}$ in S_{m2} can be represented as $\overline{O_{m2}A}=\begin{bmatrix}0 & -E_{m2} & \Delta B_2\end{bmatrix}^{\mathrm{T}}$. ω_p is the angular velocity of pinion, in S_{m2} it is $\omega_p=\begin{bmatrix}\cos\gamma_{m2} & 0 & \sin\gamma_{m2}\end{bmatrix}^{\mathrm{T}}$. ω_c is the angular velocity of the cutter, it can be written as $\omega_c=\begin{bmatrix}0 & 0 & m_{cp}\end{bmatrix}^{\mathrm{T}}$. Based on the mesh equation, the pinion flank on the concave side can be represented in S_p as

$$\begin{cases}\mathbf{R}_S^{(i)}\left(u,v,\phi_2\right)=M_{pc}\left(\phi_2\right)\cdot\mathbf{T}_{SCE}^{(i)}(u,v)\\ f\left(l_i,\varphi_i,\phi_2\right)=0\end{cases}. \tag{6.10}$$

By using the same way, the pinion fillet on the concave side can be represented in S_p as

$$\begin{cases}\mathbf{R}_C^{(i)}\left(u,v,\phi_2\right)=M_{pc}\left(\phi_2\right)\cdot\mathbf{T}_{CCE}^{(i)}(u,v)\\ f\left(l_i,\varphi_i,\phi_2\right)=0\end{cases}. \tag{6.11}$$

The machine settings of the convex side have the same parameters with the machines settings on concave side but with difference values. The pinion tooth surfaces can be presented by using the similar equations. In the previous section we introduced the method using NURBS surface to represent the pinion tooth surface. For the pinion tooth of hypoid gears, we figure out the instantaneous contact points, and also use NURBS to interpolate these points. Such as the pinion flank on concave side can be represented as

$$\mathbf{P}\left(u,v\right)=\sum_{k=0}^{m}\sum_{l=0}^{n}N_{k,d_1}\left(u\right)N_{l,d_2}\left(v\right)\mathbf{T}_{k,l}\,. \tag{6.12}$$

6.3 Applications

One pair of hypoid gears was used to illustrate how to build up the genuine tooth surfaces. The geometry of hypoid gears are the same as spiral bevel gears' geometry except there is a shaft offset between member gear and pinion, and the machining process of the hypoid gears is the similar to the machining process of spiral bevel gears. The member gear tooth surface is modeled first, and then the pinion tooth surface is generated. In this example the tilted cutter is used in the pinion tooth generation. Table 6.1 shows the data of gear cutter. Table 6.2 shows the machine settings of member gear, and Table 6.3 shows the data of member gear blank.

Table 6.1 Data of the member gear blade.

Bake rake angle	20.00^{o}	End relief angle	12.00^{o}
Side rake angle	10.00^{o}	Side relief angle	4.00^{o}
Inner blade angle	22.50^{o}	Outer blade angle	22.50^{o}
Point width	4.826 mm	Corner radius	2.794 mm
Average cutter radius	177.800 mm		

Table 6.2 Machine settings of the member gear.

Correction in machine center to back	-2.007 mm	Machine root angle	76.17^{o}
Cutter horizontal setting	100.152 mm	Cutter vertical setting	137.897 mm

Table 6.3 Data of the member gear blank.

Gear root angle	75.13^{o}	Gear face angle	80.30^{o}
Gear face width	71.120 mm	Mean cone distance	177.521 mm
Teeth number	52	Blank depth	35.000 mm
Hand of spiral	Left hand		

Fig. 6.5 shows the genuine tooth geometry of hypoid member gear, and the Fig. 6.6 shows the geometric error of cross section on normal plane of simplified tool. From the geometric error curves we find the same phenomenon. The geometric error of inner blade is larger than the outer blade due to their different distance to the cutter axis. Since the non-generated method is used, the geometric error of the tool will be the same as the gear tooth geometric error. The geometric error at the mean point on convex flank is about 0.120 mm.

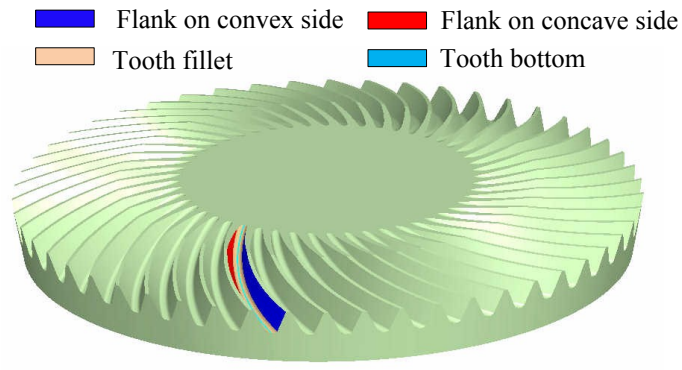

Figure 6.5 Tooth surface of hypoid member gear.

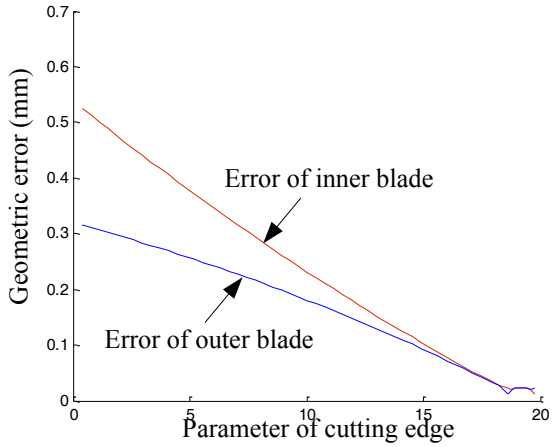

Figure 6.6 Geometric errors of the simplified cutter.

The second step is to generate the hypoid pinion tooth. Here the gear convex and pinion concave teeth are the contact surfaces. In the following tables we list out the data used for the pinion concave tooth generation. Table 6.4 shows the data of pinion cutter. Table 6.5 shows the data of pinion blank. The machine settings of pinion are represented in Table 6.6.

Table 6.4 Data of the pinion cutter.

Bake rake angle	20.00°	End relief angle	12.00°
Side rake angle	10.00°	Side relief angle	4.00°
blade angle	14.00°	Corner radius	1.000 mm
Depth of blade	18.000 mm	Cutter point radius	152.400 mm

Table 6.5 Data of pinion blank.

Pinion root angle	8.989°	Pinion pitch angle	9.633°
Mean length of pinion pitch cone generatrix	150.960 mm	Pinion face angle	13.271°

Table 6.6 Machine settings of pinion on concave side.

Blank offset	25.490 mm	Change of pinion mounting distance	-10.980 mm
Ratio of roll	0.16525	Machine root angle	-2.50°
Sliding base setting	-26.770 mm	Machine vertical setting	-132.374 mm
Machine horizontal setting	13.835 mm	Machine angular setting	-84.033°
Swivel angle	307.195°	Tilted angle	9.124°

Fig. 6.7 shows the hypoid pinion tooth on concave side. The flank and fillet are differentiated with colors. Fig. 6.8 shows the geometric errors of the simplified pinion flank and fillet. It shows the geometric error on flank is larger than the fillet.

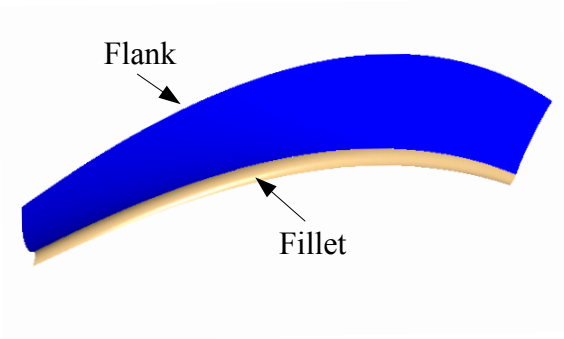

Figure 6.7 Hypoid pinion tooth on concave side.

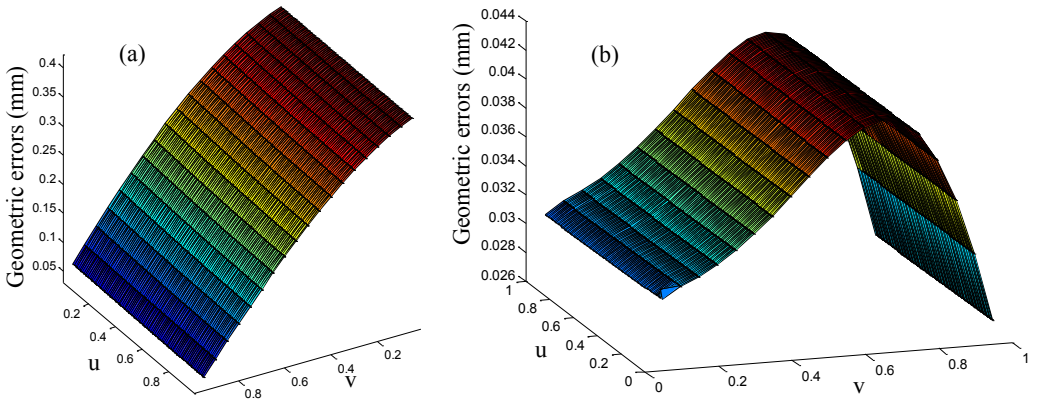

Figure 6.8 Geometric errors of the simplified pinion tooth: (a) flank, (b) fillet.

The last step is to compare the tooth contact of genuine gears to the tooth contact of simplified gears. Fig. 6.9 shows the tooth contact between the genuine hypoid gear and pinion. The coordinates of the mean point in S_g is $[-144.737 \quad 2.723 \quad 28.415]^T$.

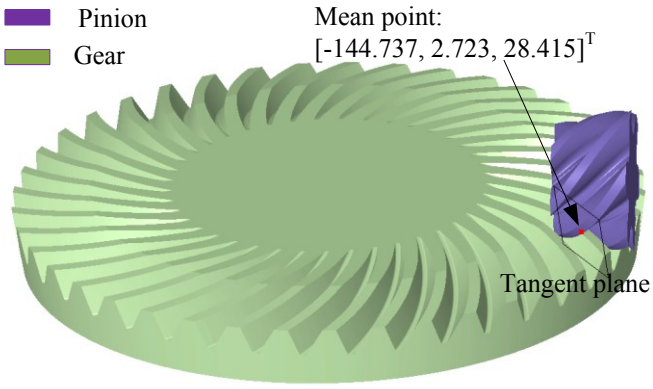

Figure 6.9 Tooth contact of genuine hypoid gears.

The tooth contacts of genuine hypoid gears and simplified hypoid gears are compared in Fig. 6.10. First, the distance between their mean points is about 1.64 mm. Second, the length of the genuine gear major axis is about 14.205 mm, and for the simplified gear it is about 20.879 mm. The area of genuine gears contact ellipse is about 11.591 mm^2, and the area of simplified contact ellipse is about 21.062 mm^2. Third, the

orientations of the contact ellipse are different, and the angle between their axes is about 2.86°. From the results we can see that there are big difference between genuine hypoid gears and simplified hypoid gears on the length of major axis and the area of contact ellipse. The simplified cutter has more effect on the tooth contact of hypoid gears than the tooth contact of spiral bevel gears.

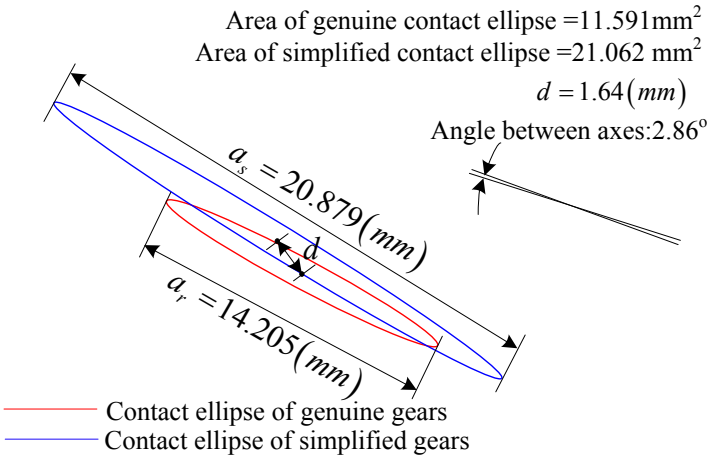

Figure 6.10 Compare of the genuine and simplified tooth contacts.

6.4 Summary

In this chapter the accurate tooth surface of hypoid gears is modeled with genuine cutter geometric model. In the pinion tooth generation, a tilted cutter is used. We use the same procedure of tooth surface generation as spiral bevel gears. In tooth contact analysis, we find the simplified cutter has more effect on the gear tooth contact of the hypoid gears compared to the spiral bevel gears.

Chapter 7 Conclusions and Future Work

In this research, an accurate approach to model the genuine tooth surface of face-milled spiral bevel and hypoid gears is proposed. The major contributions of this research summarized as follows:

- A genuine cutter geometric model for spiral bevel and hypoid gears is proposed. This model exactly matches the cutter used in real industry. The cutting edges of the genuine cutter are defined on the rake face, which is determined by the blade rake angles, relief angles and blade angle. The cross section of genuine tool surface generated by side cutting edge on normal plane is a hyperbola curve, rather than the straight line of simplified cutter, and the cross section of genuine circular cutting edge is a complicated curve, rather than the arc of simplified cutter. The examples show that the geometric error of simplified cutter is affected by the cutter geometric parameters, and the error is about 0.2 mm at mean point which is too much larger than the tooth surface 10 um tolerance requirement.
- The accurate tooth surface of spiral bevel gears is build up by using the genuine cutter geometric model based on machine kinematics model during machining process. First, the tooth surface of non-generated member gear is modeled using the genuine cutter model, and then the generated pinion tooth surface represented as NURBS surface, rather than the typical representation with three independent parameters, and two equations. During the tooth generation, the accuracy of the NURBS tooth surface is controlled within specified tolerance by optimizing the

sampling points and control points. This NURBS tooth surface can be directly implemented in the CAD software. In the tooth contact analysis, the contact ellipses produced by genuine and simplified cutter are different in term of orientation and contact area.

- The accurate tooth surface of hypoid gears is build up by using the genuine cutter geometric model. In the tooth surface generation of hypoid gears, the same procedure is used as the spiral bevel gears. The member gear tooth is modeled first, and then the pinion tooth is generated with genuine cutter geometric model. In the final tooth contact analysis, the simplified cutter has more effect on the tooth contact of the hypoid gears compared to the spiral bevel gears since the shaft offset and tilted cutter are used in the hypoid gear machining. The big different on tooth contact area will significantly affect the stress on the gear teeth.

In this work, the genuine gear tooth surfaces of spiral bevel and hypoid gears are accurately modeled by using genuine blade geometric model. It can avoid 0.2mm geometric error in gear tooth modeling compared to the gear tooth modeled by using simplified blade model. Based on the genuine gear tooth, the face milling process can be used in the gear tooth finishing, and obtain accurate tooth surface. It can also obtain equally distributed residue stress on the gear stock in the tooth roughing, and also the workload on the cutter in finishing process will be reduced, thus the life of gear cutter will be prolonged.

For future research, following topics are suggested to expand the present research work:

- Calculating the pinion machine settings based on the genuine member gear and cutter geometric model;
- Conducting the FEA on the gear tooth to analysis the stress difference on genuine and simplified gear tooth.
- Modeling the in-process geometric model of gear and pinion, and predicting the cutting forces during gear teeth machining.

Bibliography

[1] F. L. Litvin, *Gear Geometry and Applied Theory*. Cambridge University Press, 2004.

[2] P. R. Stephen, *Dudley's handbook of practical gear design and manufacture*. 2 edition ed.: CRC, 2012.

[3] Gleason. Available: www.gleason.com Dec. 8, 2011

[4] Klingelnberg. Available: http://www.klingelnberg.com Dec. 8, 2011

[5] Oerlikon. Available: http://www.oerlikon.com Dec. 8, 2011

[6] S. H. Suh, W. S. Jih, H. D. Hong *et al.*, "Sculptured surface machining of spiral bevel gears with CNC milling," *International Journal of Machine Tools and Manufacture,* vol. 41, no. 6, pp. 833-850, 2001.

[7] S. H. Suh, D. H. Jung, E. S. Lee *et al.*, "Modelling, implementation, and manufacturing of spiral bevel gears with crown," *International Journal of Advanced Manufacturing Technology,* vol. 21, no. 10-11, pp. 775-86, 2003.

[8] S. M. Safavi, S. S. Mirian, R. Abedinzadeh *et al.*, "Use of PLC module to control a rotary table to cut spiral bevel gear with three-axis CNC milling," *International Journal of Advanced Manufacturing Technology,* vol. 49, no. 9-12, pp. 1069-1077,2010.

[9] C. Ozel, A. Ian, and L. Ozler, "An investigation on manufacturing of the straight bevel gear using end mill by CMC milling machine," *Journal of Manufacturing Science and Engineering, Transactions of the ASME,* vol. 127, no. 3, pp. 503-511, 2005.

[10] K. Kawasaki, and K. Shinma, "Accuracy measurement and evaluation of straight bevel gear manufactured by end mill using CNC milling machine," *Journal of Mechanical Design, Transactions of the ASME,* vol. 131, no. 1, pp. 0110011-0110018, 2009.

[11] F. Qi, "Computerized modeling and simulation of spiral bevel and hypoid gears manufactured by Gleason face hobbing process," *Transactions of the ASME. Journal of Mechanical Design,* vol. 128, no. 6, pp. 1315-27, 2006.

[12] S. Yi-Pei, F. Zhang-Hua, and G. C. Y. Lin, “Mathematical model for a universal face hobbing hypoid gear generator,” *Transactions of the ASME. Journal of Mechanical Design,* vol. 129, no. 1, pp. 38-47, 2007.

[13] M. Vimercati, “Mathematical model for tooth surfaces representation of face-hobbed hypoid gears and its application to contact analysis and stress calculation,” *Mechanism and Machine Theory,* vol. 42, no. 6, pp. 668-690, 2007.

[14] F. Qi, “Tooth surface error correction for face-hobbed hypoid gears,” *Journal of Mechanical Design,* vol. 132, no. 1, pp. 011004 (8 pp.), 2010.

[15] Y. Xu, L. Zhang, W. Wei *et al.*, "Virtual simulation machining on spiral bevel gear with new type spiral bevel gear milling machine," *2009 International Conference on Measuring Technology and Mechatronics Automation (ICMTMA).* pp. 432-5, 2009.

[16] Y. Xu, L. Zhang, W. Wei *et al.*, "Digitized conjugate tooth surface model of spiral bevel gear and its simulation," *2009 IEEE International Conference on Mechatronics and Automation, ICMA 2009.* pp. 3453-3458.

[17] Z. Li, Y. Wang, and D. Xue, "Modeling and simulating of spiral bevel gears based on actual cutting process," *Proceedings of the IEEE International Conference on Automation and Logistics, ICAL 2007.* pp. 1694-1698, 2007.

[18] S. H. Suh, E. S. Lee, H. C. Kim *et al.*, “Geometric error measurement of spiral bevel gears using a virtual gear model for STEP-NC,” *International Journal of Machine Tools & Manufacture,* vol. 42, no. 3, pp. 335-42, 2002.

[19] P. Weimin, L. Yi, and L. Jishun, "Control of analogue scan probe in CMM inspect of spiral bevel gear," *2006 IEEE International Conference on Mechatronics and Automation, ICMA 2006.* pp. 79-83, 2006.

[20] M. Kolivand, and A. Kahraman, “An ease-off based method for loaded tooth contact analysis of hypoid gears having local and global surface deviations,” *Journal of Mechanical Design, Transactions of the ASME,* vol. 132, no. 7, pp. 0710041-0710048, 2010.

[21] M. Kolivand, and A. Kahraman, “A load distribution model for hypoid gears using ease-off topography and shell theory,” *Mechanism and Machine Theory,* vol. 44, no. 10, pp. 1848-1865, 2009.

[22] M. Guagliano, L. Vergani, and M. Vimercati, “Sub-surface crack propagation analysis in hypoid gears,” *Engineering Fracture Mechanics,* vol. 75, no. 3-4, pp. 417-26, 2008.

[23] M. Vimercati, M. Guagliano, and L. Vergani, "Determination of stress intensity factors for three-dimensional subsurface cracks in hypoid gears," *Engineering Fracture Mechanics,* vol. 73, no. 14, pp. 1947-58, 2006.

[24] A. Ural, G. Heber, P. A. Wawrzynek *et al.*, "Three-dimensional, parallel, finite element simulation of fatigue crack growth in a spiral bevel pinion gear," *Engineering Fracture Mechanics,* vol. 72, no. 8, pp. 1148-70, 2005.

[25] M. A. Hotait, A. Kahraman, and T. Nishino, "An investigation of root stresses of hypoid gears with misalignments," *Journal of Mechanical Design, Transactions of the ASME,* vol. 133, no. 7, pp. 071006 (9 pp.), 2011.

[26] Y. Cheng, and T. C. Lim, "Vibration analysis of hypoid transmissions applying an exact geometry-based gear mesh theory," *Journal of Sound and Vibration,* vol. 240, no. 3, pp. 519-543, 2001.

[27] J. Wang, T. C. Lim, and M. Li, "Dynamics of a hypoid gear pair considering the effects of time-varying mesh parameters and backlash nonlinearity," *Journal of Sound and Vibration,* vol. 308, no. 1-2, pp. 302-329, 2007.

[28] P.-Y. Wang, S.-C. Fan, and Z.-G. Huang, "Spiral bevel gear dynamic contact and tooth impact analysis," *Journal of Mechanical Design, Transactions of the ASME,* vol. 133, no. 8, 2011.

[29] J. H. Yoon, B. J. Choi, I. H. Yang *et al.*, "Deflection test and transmission error measurement to identify hypoid gear whine noise," *International Journal of Automotive Technology,* vol. 12, no. 1, pp. 59-66, 2011.

[30] C. Gosselin, T. Nonaka, Y. Shiono *et al.*, "Identification of the machine settings of real hypoid gear tooth surfaces," *Journal of Mechanical Design, Transactions of the ASME,* vol. 120, no. 3, pp. 429-440, 1998.

[31] C. Y. Lin, C. B. Tsay, and Z. H. Fong, "Computer-aided manufacturing of spiral bevel and hypoid gears with minimum surface-deviation," *Mechanism and Machine Theory,* vol. 33, no. 6, pp. 785-803, 1998.

[32] C.-Y. Lin, C.-B. Tsay, and Z.-H. Fong, "Computer-aided manufacturing of spiral bevel and hypoid gears by applying optimization techniques," *Journal of Materials Processing Technology,* vol. 114, no. 1, pp. 22-35, 2001.

[33] W. Pei-Yu, and F. Zhang-Hua, "Fourth-order kinematic synthesis for face-Milling spiral bevel gears with modified radial motion (MRM) correction," *Transactions of the ASME. Journal of Mechanical Design,* vol. 128, no. 2, pp. 457-67, 2006.

[34] V. Simon, "Head-cutter for optimal tooth modifications in spiral bevel gears," *Mechanism and Machine Theory,* vol. 44, no. 7, pp. 1420-1435, 2009.

[35] V. Simon, "Optimal tooth modifications in hypoid gears," *Transactions of the ASME. Journal of Mechanical Design,* vol. 127, no. 4, pp. 646-55, 2005.

[36] F. Qi, "Optimization of Face Cone Element for Spiral Bevel and Hypoid Gears," *Journal of Mechanical Design,* vol. 133, no. 9, pp. 091002 (7 pp.), 2011.

[37] J. Zhang, Z. Fang, X. Cao *et al.*, "The modified pitch cone design of the hypoid gear: Manufacture, stress analysis and experimental tests," *Mechanism and Machine Theory,* vol. 42, no. 2, pp. 147-158, 2007.

[38] F. L. Litvin, L. Qiming, and A. L. Kapelevich, "Asymmetric modified spur gear drives: reduction of noise, localization of contact, simulation of meshing and stress analysis," *Computer Methods in Applied Mechanics and Engineering,* vol. 188, no. 1-3, pp. 363-90, 2000.

[39] F. L. Litvin, Q. Fan, D. Vecchiato *et al.*, "Computerized generation and simulation of meshing of modified spur and helical gears manufactured by shaving," *Computer Methods in Applied Mechanics and Engineering,* vol. 190, no. 39, pp. 5037-55, 2001.

[40] F. L. Litvin, A. Fuentes, C. Zanzi *et al.*, "Face-gear drive with spur involute pinion: geometry, generation by a worm, stress analysis," *Computer Methods in Applied Mechanics and Engineering,* vol. 191, no. 25-26, pp. 2785-813, 2002.

[41] F. L. Litvin, A. Fuentes, A. Demenego *et al.*, "New developments in the design and generation of gear drives," *Proceedings of the Institution of Mechanical Engineers, Part C: Journal of Mechanical Engineering Science,* vol. 215, no. 7, pp. 747-757, 2001.

[42] F. L. Litvin, and J. Lu, "Computerized design and generation of double circular-arc helical gears with low transmission errors," *Computer Methods in Applied Mechanics and Engineering,* vol. 127, no. 1-4, pp. 57-86, 1995.

[43] J. Lu, F. L. Litvin, and J. S. Chen, "Load share and finite element stress analysis for double circular-arc helical gears," *Mathematical and Computer Modelling,* vol. 21, no. 10, pp. 13-30, 1995.

[44] F. L. Litvin, J. Lu, D. P. Townsend *et al.*, "*Computerized simulation of meshing of conventional helical involute gears and modification of geometry*," NASA Technical Memorandum 107451, 1997.

[45] F. L. Litvin, A. Fuentes, I. Gonzalez-Perez *et al.*, "Modified involute helical gears: computerized design, simulation of meshing and stress analysis," *Computer Methods in Applied Mechanics and Engineering,* vol. 192, no. 33-34, pp. 3619-55, 2003.

[46] I. Gonzalez-Perez, F. L. Litvin, A. Fuentes *et al.*, "Topology of modified surfaces of involute helical gears with line contact developed for improvement of bearing contact, reduction of transmission errors, and stress analysis," *Mathematical and Computer Modelling,* vol. 42, no. 9-10, pp. 1063-78, 2005.

[47] F. L. Litvin, and M. De Donno, "Computerized design and generation of modified spiroid worm-gear drive with low transmission errors and stabilized bearing contact," *Computer Methods in Applied Mechanics and Engineering,* vol. 162, no. 1-4, pp. 187-201, 1998.

[48] F. L. Litvin, G. Argentieri, M. de Donno *et al.*, "Computerized design, generation and simulation of meshing and contact of face worm-gear drives," *Computer Methods in Applied Mechanics and Engineering,* vol. 189, no. 3, pp. 785-801, 2000.

[49] F. L. Litvin, A. Nava, F. Qi *et al.*, "New geometry of face worm gear drives with conical and cylindrical worms: generation, simulation of meshing, and stress analysis," *Computer Methods in Applied Mechanics and Engineering,* vol. 191, no. 27-28, pp. 3035-54, 2002.

[50] F. L. Litvin, and P.-H. Feng, "Computerized design, generation, and simulation of meshing of rotors of screw compressor," *Mechanism and Machine Theory,* vol. 32, no. 2, pp. 137-160, 1997.

[51] F. L. Litvin, and Y. Gutman, "Methods of Synthesis and Analysis for Hypoid Gear-Drives of Formate and Helixform - 1. Calculations for Machine Settings for Member Gear Manufacture of the Formate and Helixform Hypoid Gears," *American Society of Mechanical Engineers (Paper)*, no. 80 -C2/DET-31, 1980.

[52] F. L. Litvin, and Y. Gutman, "Methods of Synthesis and Analysis for Hypoid Gear-Drives of Formate and Helixform - 2. Machine Setting Calculations for the Pinions of Formate and Helixform Gears," *American Society of Mechanical Engineers (Paper)*, no. 80 -C2/DET-32, 1980.

[53] F. L. Litvin, and Y. Gutman, "Methods of Synthesis and Analysis for Hypoid Gear-Drives of Formate and Helixform - 3. Analysis and Optimal Synthesis Methods for Mixmatch Gearing and its Application for Hypoid Gears of Formate and Helixform," *American Society of Mechanical Engineers (Paper)*, no. 80 -C2/DET-33, 1980.

[54] F. L. Litvin, R. F. Handschuh, and Y. Zhang, "Computerized design of low-noise face-milled spiral bevel gears," *American Society of Mechanical Engineers, Design Engineering Division (Publication) DE.* pp. 129-137, 1994.

[55] F. L. Litvin, A. Fuentes, Q. Fan *et al.*, "Computerized design, simulation of meshing, and contact and stress analysis of face-milled formate generated spiral bevel gears," *Mechanism and Machine Theory,* vol. 37, no. 5, pp. 441-459, 2002.

[56] F. L. Litvin, A. G. Wang, and R. F. Handschuh, "Computerized generation and simulation of meshing and contact of spiral bevel gears with improved geometry," *Computer Methods in Applied Mechanics and Engineering,* vol. 158, no. 1-2, pp. 35-64, 1998.

[57] J. Argyris, A. Fuentes, and F. L. Litvin, "Computerized integrated approach for design and stress analysis of spiral bevel gears," *Computer Methods in Applied Mechanics and Engineering,* vol. 191, no. 11-12, pp. 1057-1095, 2002.

[58] A. Fuentes, F. L. Litvin, B. R. Mullins *et al.*, "Design and stress analysis of low-noise adjusted bearing contact spiral bevel gears," *Journal of Mechanical Design, Transactions of the ASME,* vol. 124, no. 3, pp. 524-532, 2002.

[59] F. L. Litvin, A. Fuentes, and K. Hayasaka, "Design, manufacture, stress analysis, and experimental tests of low-noise high endurance spiral bevel gears," *Mechanism and Machine Theory,* vol. 41, no. 1, pp. 83-118, 2006.

[60] C.-Y. Lin, C.-B. Tsay, and Z.-H. Fong, "Mathematical model of spiral bevel and hypoid gears manufactured by the modified roll method," *Mechanism and Machine Theory,* vol. 32, no. 2, pp. 121-136, 1997.